Effects of Random Manufacturing Errors on the Performance of Contemporary Coherent Radiation Sources

by

Ian M. Rittersdorf

A dissertation submitted in partial fulfillment
of the requirements for the degree of
Doctor of Philosophy
(Nuclear Engineering and Radiological Sciences)
in The University of Michigan
2014

Doctoral Committee:

Professor Yue Y. Lau, Chair
Associate Professor John E. Foster
Professor Ronald M. Gilgenbach
Professor Mark J. Kushner

To my family and friends

ACKNOWLEDGEMENTS

First and foremost I must thank my chair, Professor Y.Y. Lau. Without him, none of this would have been possible. It was his guidance, support, advice, wisdom, and mentorship that has made me into the scientist that I am today and given me the tools to succeed in the future. I would certainly not be where I am without him and for that I am forever grateful. Next, I would like to thank Professor Ron Gilgenbach for his teachings and support, which helped to broaden my knowledge of experiments. Any time that I shared in the lab with him he was able to teach me something that "you can't find in books". I would like to thank Professor John Foster for his enthusiastic lectures in NERS 471 that served as my introduction to plasmas and the inspiration to study them further. I would also like to thank Professor Mark Kushner for getting me involved with the Michigan Institute for Plasma Science and Engineering. MIPSE is a wonderful program that allowed me to connect with other scientists and broaden my knowledge of plasma research. I am very proud of my MIPSE Certificate. I want to thank all members of my thesis committee for taking time out of their busy schedules for me.

There are many senior scientists without whom this thesis would have never happened. Dr. Phongphaeth Pengvanich worked to bring me up to speed on a project he was working on as I transitioned into graduate school and he was transitioning out. His training was an invaluable introduction to vacuum electron devices and numerical methods while his other works would prove to be the basis of much of the research in this thesis. Other graduate students of the previous generation, Dr. David French,

Dr. Matt Gomez, and Dr. Jacob Zier, were all essential to my training and taught me how to be a graduate student during those first few years of classes. A very special thanks to Dr. David Chernin of SAIC/Leido and Professor Tom Antonsen, Jr. of the University of Maryland at College Park. It was such an honor to work alongside such encouraging and knowledgeable scientists. Our former lab manager, Dr. David Chalenski, was always there to encourage me both professionally and as a friend.

My fellow graduate students during my time in school, Dr. Bradley Sommers, David Simon, Matt Weis, Dr. Aimee Hubble, Dr. Brandon Weatherford, Sonal Patel, Paul Cummings, and Dr. Peng Zhang, have made my time as a graduate student memorable. In particular, Matt Franzi has been many things to me over the years: a colleague, a roommate, a fellow intern, a coworker, but above all he has been a great friend. Thank you for sharing in all of our many triumphs.

All of my family and friends have offered me emotional support and encouragement throughout the years. I wouldn't be here without my parents, Mary and David. They raised me to believe that I could do anything if I put my mind to it and worked hard. Elizabeth Spehalski was nothing but compassionate and understanding throughout this entire process. Thank you for being so patient with me. I could not have asked for a better partner.

This research was supported by the Office of Naval Research, Air Force Office of Scientific Research Grant FA 9550-09-1-0662, Air Force Research Laboratory, L-3 Communications Electron Device Division, and Northrop-Grumman Corporation.

TABLE OF CONTENTS

LIST OF FIGURES

Figure

LIST OF TABLES

Table

LIST OF APPENDICES

Appendix

ABSTRACT

Effects of Random Manufacturing Errors on the Performance of Contemporary Coherent Radiation Sources

by

Ian M. Rittersdorf

Chair: Yue Ying Lau

The traveling wave tube (TWT) is a linear beam microwave vacuum electron device (MVED) and is a key element in telecommunication systems, satellite-based transmitters, military radar, electronic countermeasures, and communication data links. Variations in TWT performance due to random errors in the manufacturing process can drive up the cost. These errors provide a proportionately larger perturbation to the circuit as the frequency increases into the sub-millimeter wavelength regime and beyond. Previous studies calculated the standard deviation in the small-signal gain and phase of a TWT in the presence of small random, axially varying perturbations in the circuit phase velocity, but assumed zero space charge effects and synchronous interaction. This work relaxes the latter assumptions and calculates the ensemble-average gain and phase by two analytic approaches as well as a numerical calculation. The analytic theory resolved a previously unexplained puzzle where a significant fraction of samples with random circuit errors show a higher gain than an error-free tube. The effects of multiple internal reflections are also presented and

their effects on the small-signal gain and phase are shown to be significant. Due to interest in the absolute instability of TWTs with such internal reflections, the absolute instability in a dielectric waveguide is investigated.

The magnetron is another type of MVED in a crossed-field configuration that is promising to deliver GWs of power in the GHz frequency range. The peer-to-peer configuration is an attractive method of phase-locking a large number of very efficient, lower power magnetrons. This thesis advances the theory a step further by examining the viability of peer-to-peer locking when two magnetrons in a peer-to-peer configuration suffer from a frequency chirp or contain a low frequency noise component. An argument is made that the analysis of temporal locking is analogous to the spatial locking experimentally observed in neighboring wires in z-pinch arrays. A framework for the interpretation of spatial locking found in these experiments is provided.

CHAPTER 1

Introduction

1.1 Random Fabrication Errors and Random Noise in Microwave Sources

Microwave sources are a class of device that have a wide range of impactful applications, including telecommunications, satellite-based transmission systems, military radars, electronic countermeasures, and communication data links [1–3]. The current interest with this technology is to push these microwave sources to higher frequencies, in the terahertz range, and to higher powers, deep into the gigawatt range [2, 4]. One challenge that arises when trying to realize these goals is that random variations due to error tolerances in the manufacturing process or random noise in a device during operation can effect the performance of the microwave source. This thesis explores such phenomena in two specific microwave sources: the traveling wave tube (TWT) and the magnetron.

The TWT is the prime candidate for a high power, coherent THz radiation source, with the ultimate goal of being integrated in microwave power modules (MPMs). The MPM is a miniature, complete amplifier package containing a TWT, integrated power conditioner, and solid state amplifier [5]. These miniature and efficient amplifiers, at sub-THz frequencies, have been deployed for airborne and space applications where

small size, low weight, and minimal power consumption are advantageous [6]. The use of terahertz radiation is thought to be an important tool in counter-improvised explosive device (C-IED) sensing techniques [7]. Currently, the most advanced THz TWT was developed by Kreischer's group at Northrop Grumman, producing 67 mW at 0.850 THz, using an electron beam of 11.7 kV, 2.5 mA in a folded waveguide circuit [8]. As the millimeter and sub-millimeter wavelength regimes are approached, the feature size of TWTs will approach that of the tolerances of modern manufacturing methods. This leads to performance degrading perturbations. This thesis will investigate such effects.

Some of the primary applications for high power magnetrons are radar systems, power beaming, and industrial heating [9]. For radar systems, the maximum detection range scales as $P^{1/4}$, where P is the power, therefore significant gains in the high power output of magnetrons is of interest [10]. One appealing way of creating high power microwaves would be to combine the output of several, medium power magnetron sources together in a configuration known as peer-to-peer locking. Even though a magnetron has a characteristic operating frequency, in practice there is some finite spread in the output signal spectrum or some noise component to the frequency output. Magnetron noise has been known to be an important issue from the outset, and numerous attempts to reduce it have been made [11]. This thesis investigates the effects of frequency chirps, where the output frequency of one magnetron drifts upward (or downward) as a function of time, and random noise in the output signal of two magnetrons that are locked in a peer-to-peer configuration. Similar phenomena is observed in adjacent optical waveguides of CO_2 lasers [12]. In such an experiment, the coupling was provided by radiation leaking through a ZnSe plate that separated the two waveguides and locking was only observed when the individual lasers were operating on the same transition. Further, it is noticed that the temporal locking of two such oscillators is similar to the spatial locking that is observed on the ablation

structure of neighboring wires in z-pinch array plasmas. This thesis also offers an interpretation of this spatial locking phenomenon that is analogous to that of the temporal locking of magnetrons.

1.2 Description of Coherent Radiation Sources Discussed in this Thesis

1.2.1 Traveling Wave Tubes

The traveling wave tube is a linear beam device [1, 10]. It is capable of delivering kilowatts of power in the tens of gigahertz frequency range by converting the kinetic energy of a DC electron beam into RF energy. Although the initial experiments were performed on the TWT by Kompfner in 1947 [13], the theory of TWTs was largely founded by J. R. Pierce of Bell Telephone Laboratories in the late 1940s [14]. The Pierce theory of TWTs is still widely used in the analysis of TWTs (and other sources such as free electron lasers and gyrotrons) to this day and will be the basis of the analysis performed in this thesis. There are several types of TWTs: helix, coupled-cavity, folded waveguide, ring bar, and ladder. The standard Pierce theory, to be described in Section 2.3, is applicable to all types in the basic description.

The general model of a TWT, with a few key components, is shown in Fig. 1.1 [1]. An electron beam is produced from the electron gun. This beam travels down the axis of the vacuum envelope and into the collector, where some of the kinetic energy of the beam is recovered to improve overall efficiency. While the collector can exist in many configurations, they all operate on the principle of applying on a negative voltage bias such that the electrons slow down before being collected on the structure wall. The beam is confined inside the vacuum envelope by a magnetic field supplied by a magnet structure outside of the vacuum envelope. The RF signal to be amplified is injected into the TWT at the input and travels down a slow wave circuit in the form of a

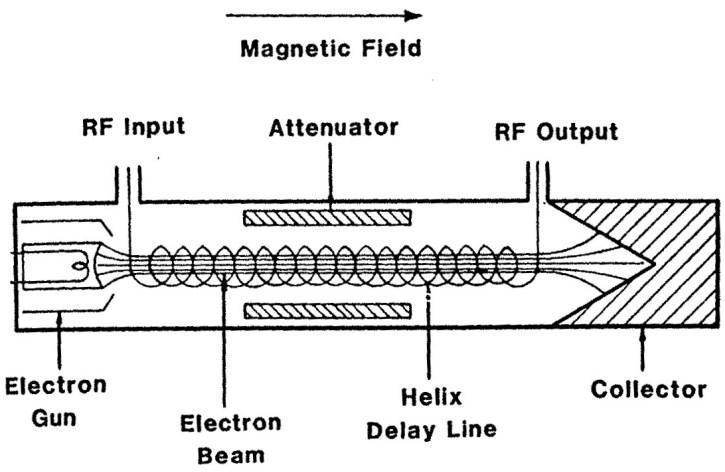

Figure 1.1: The basic components of a typical traveling wave tube. The labeled components are the electron gun, the RF input, the magnetic field, the attenuator, slow wave circuit (helix type shown here), the RF output, and the collector. All of these components are inside the TWT vacuum envelope. Image from [1].

helix or other structure and is collected at the RF output. The slow wave structure slows the *axial* speed of the RF signal to approximately that of the electron beam so the two may interact continuously as they co-move down the axis of the TWT. During this continuous interaction, the electron beam gives up its kinetic energy to the RF wave and RF amplification occurs. An attenuator is sometimes used to damp out the backward wave which may cause feedback oscillations of TWTs. Typically, the TWT may be described by the linear theory in the first 85 percent of the axial length. Non-linear saturation, when it occurs, takes place only at the last 15 percent of the axial length. This thesis, therefore, adopts Pierce's linear theory of TWTs as described in Section 2.3.

When an RF signal is injected into a TWT it usually generates four waves: three waves traveling in the forward direction (from input to output) and one traveling in the backward direction (from output to input). In the analysis performed in Chapter 2, the backward wave is ignored although its effects are discussed in Chapter 3. Of the three forward waves, one wave grows exponentially in space as it travels down the

axis and provides the gain in the amplifier. The second of the waves decays exponentially in space as it travels down the axis, and the third forward wave maintains its amplitude as it travels down the axis in a lossless circuit. This input power injected into the TWT must be split between these three waves, leading to a phenomenon known as launching loss [1, 14].

The fractional difference between the velocity of the electron beam and the axial component of the circuit phase velocity is one of the most important parameters in the operation of the TWT because it is a measure of the degree of synchronism between the circuit wave and the beam's motion. In the case of the helix slow wave structure, it is the geometry of the helix that determines the axial circuit phase velocity. The dimensions of the helix can change in the presence of manufacturing tolerances, slightly changing the axial circuit phase velocity and thus altering the synchronous interaction in a TWT, affecting the gain and the phase in the output signal.

1.2.2 Magnetrons

The magnetron is a crossed-field device, meaning that the electric field and the magnetic field within the device are perpendicular to each other. The magnetron is a very robust microwave source that is capable of generating GWs of power in the GHz frequency range [2, 10]. The earliest demonstrations of the magnetron were performed by Arthur Hull around 1920 at General Electric's Research Laboratory. The cavity magnetron was first introduced by Randall and Boot of the University of Birmingham in 1940 during the push for radar technologies in World War II. After the war, many theoretical contributions on magnetrons came from some major scientists including Buneman, Hartree, Lamb, and Slater. One of the greatest appeals of the magnetron as a microwave source is its extremely high efficiency, ranging from 50% upwards to 90%, and how inexpensive it is to manufacture; the kilowatt oven magnetron,

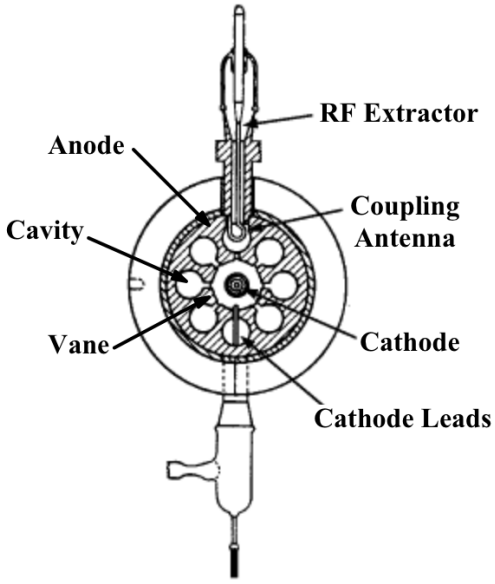

Figure 1.2: A schematic of an eight cavity magnetron highlighting all of the major components. Original image from [1].

most commonly used in household appliances, only costs around $7 to manufacture [9]. While the prevalence of the magnetron has led to extensive study, there is no comprehensive theory for the operation of the magnetron [15]. For example, to-date there is no generally accepted theory which gives the voltage-current characteristics of a magnetron; the proper interpretation of the Buneman-Hartree condition, which is the basic design rule for magnetrons, has been recently questioned [16].

A schematic of a cylindrical magnetron is shown in Fig. 1.2 [1]. The electrons are emitted from the cathode via thermionic emission and the magnetic field confines the electrons within the interaction space between the cathode and the anode. A slow wave structure on the anode is created by periodic placement of cavities and vanes. This slow wave structure sets up vacuum RF modes, some of which will have resonance and become excited by the interaction between electrons with the RF modes. The electrons will then form "spokes" which will oscillate in and out of the RF cavities. The onset of these oscillations is known as start-up. The RF signal is extracted through one of the cavities by the RF extractor. Table 1.1 lists the typical

operating parameters of a conventional high power magnetron [17].

Parameter	**Conventional Value**
Voltage	$\leq$ 100 kV
Current	$\sim$100 A
Cathode Type	Thermionic & Secondary Emission
Pulse Duration	$\geq 1\mu$s
Risetime	$\leq$ 200 kV / μs
Power	$\leq$ 10 MW
Efficiency	50% $-$ 90%

Table 1.1: List of typical operating parameters for a conventional high power magnetron [17].

1.2.3 Wire Array Z-Pinches

The z-pinch is a different type of source of electromagnetic radiation. Since this thesis also considers spatial locking observed in the ablated wires in a z-pinch, we give a brief description of the z-pinch here. The contemporary z-pinch is used to produce high energy x-rays instead of microwaves [18–20]. The conventional z-pinch consists of a plasma column through which an intense current is passed that is sufficient to create an azimuthal magnetic field that provides an inward Lorentz force to compress and confine the plasma. This confinement proves to be insufficient for thermonuclear fusion due to the surface instabilities that the z-pinch suffers from, which include the magneto-Rayleigh-Taylor (MRT) instability, and the sausage and kink instabilities, as seen in Fig. 1.3 [21]. Even though the z-pinch plasma is insufficient for thermonuclear fusion, it is a powerful high energy x-ray source [18–20]. Unfortunately, the instabilities mentioned above reduce the x-ray yield of z-pinches as well.

In recent years, the z-pinch plasma is created by a circular array of wires made of high-Z materials, typically tungsten [20, 22]. An intense current on the order of 20 MA is passed through this array, causing all of the wires to ablate into plasma. The ablated plasma, and the wires themselves, are then accelerated to the center of the array where it stagnates and the hot, dense plasma emits x-rays. These x-rays

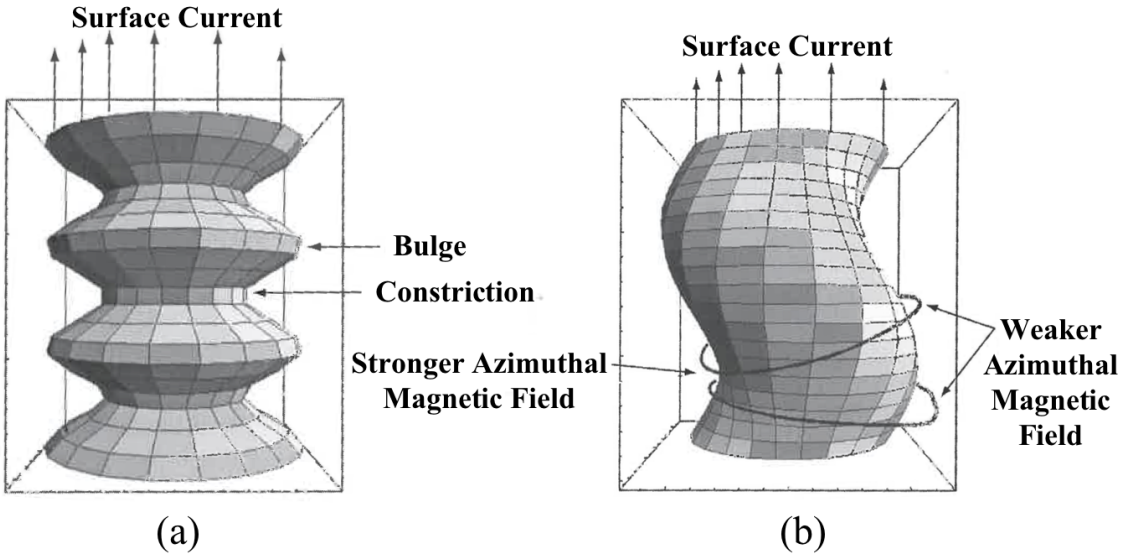

Figure 1.3: An example of the (a) sausage and (b) kink instabilities on the surface of a current carrying plasma column. Image from [21].

are used to drive Inertial Confinement Fusion (ICF) targets, experimental studies of equations of state, or for x-ray diagnostics [23]. The ablation structure of a wire in the middle of a current pulse can be seen in Fig. 1.4 [24]. In this figure, the sausage-like instability is apparent in the ablation structure.

It has been found that the ablation structure of two such wires in a z-pinch wire array will correlate when the distance between the two wires becomes sufficiently small [25]. This thesis attempts to use the phenomenon of the temporal locking of magnetrons in the peer-to-peer configuration to describe this spatial locking behavior [26].

1.3 Prior Work

1.3.1 Effects of Random Errors on TWTs

Some of the earliest investigations of fabrication errors in the performance of a helix slow wave TWT were made by D'Agostino and Paoloni [27]. In these early

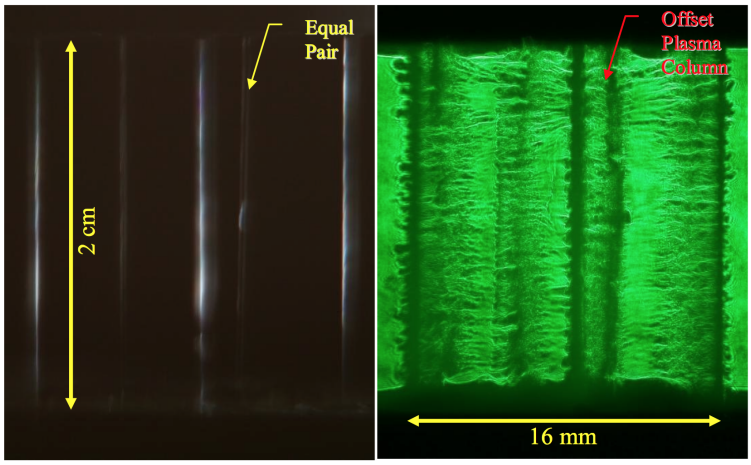

Figure 1.4: A front-lit preshot image (left) and a laser backlit image (right) at 92 ns during a shot of a tungsten wire array pulsed with intense current from a 1 MA driver. Figure from [24].

works, the effects of the mechanical tolerance of the dielectric rods that hold the helix circuit in place were investigated. Specifically, the effects of altering the three different dimensions that define a T-shaped rod (Fig. 1.5), a very common rod shape, were investigated and showed that the circuit phase velocity would change most significantly to variation in the width of the dielectric rods. Following this, D'Agostino and Paoloni went on evaluate the effect this would have on the small-signal gain of the TWT [28]. They developed a method by which the electrical parameters of the slow wave circuit can be calculated quickly and accurately. The small-signal gain was then determined by using the standard Pierce theory [14]. The parameters are assumed to be uniform and constant over the entire tube so that the standard Pierce theory may be applied on each sample. The purpose of this method was to be able to quickly evaluate many TWTs with small variations in the dimensions of the dielectric support rods as a design tool to understand the sensitivity of the rod dimensions to TWT performance. Their calculations were validated by comparison to experimental data.

D'Agostino and Paoloni next extended their investigation to the tolerances of the helix wire dimensions and their effect on the TWT small-signal gain [29]. Here, a five

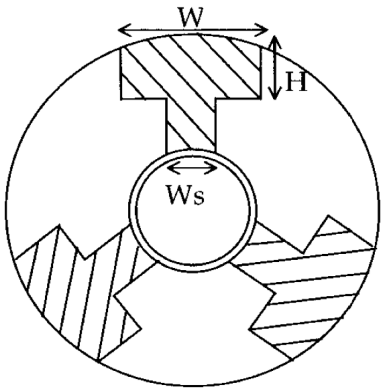

Figure 1.5: A schematic showing T-shaped dielectric rods holding a TWT helix circuit in place. The three dimensions varied by D'Agostino et al. [27] are labeled. Image from [27].

section TWT with an operational bandwidth of 10 - 13 GHz was considered. When the dimensions of the helix in each of the five sections were allowed to vary by $\pm 10\%$, it was found that variations in the gain as large as 8 dB could occur. The effects of the helix pitch tolerance, i.e., period length, for a multi-segment TWT were also studied [30]. A key result of this study showed that just a $\pm 5\%$ tolerance to the helix pitch value produced less than 10% of simulated TWTs with both less than 1 dB variation in the average gain and less than 6% flatness to the gain curve. The effects of dimensional variations in a 94 GHz folded-waveguide TWT were investigated as well by Wilson and Chevalier [31]. In their work, only dimensional variations in the period of the slow wave structure were considered and the TWT performance was simulated by the 2-D NASA Coupled-Cavity TWT Code. The period length as a function of axial position was then optimized to the average power for three different configurations: the nominal period and the nominal period plus/minus the dimensional tolerance. It was found that this optimization technique produced designs that were significantly less sensitive to dimensional tolerance variations than standard design techniques in the limit of high frequencies, i.e., short period lengths. In the limit of long period lengths the optimization algorithm produced similar results to that of standard design techniques.

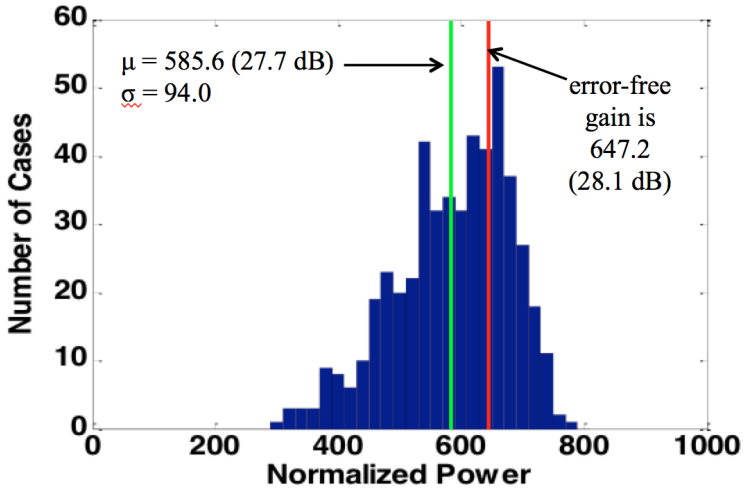

Figure 1.6: Previous works of Pengvanich et al. showing the gain distribution of 500 simulated TWTs, each with unique, random perturbations to the circuit phase velocity. Note that while the mean gain of the distribution (green line) is less than the error-free gain (red line), a significant number of samples show a power gain greater than 647, the gain for the error-free tube. Original image from [32].

A key assumption in previous investigations by D'Agostino and Paoloni (and also by Wilson and Chevalier), is that each section had a uniform, fixed geometry so that the Pierce theory for uniform tubes may be applied to that section in each amplifier. The uniform circuit phase velocity was allowed to fluctuate around some mean value. This circuit phase velocity would then vary amongst all of the simulated traveling wave tubes. This crucial assumption was relaxed by Pengvanich et al. [32, 33]. In this work, the fabrication errors are allowed to vary randomly at all axial positions along the entire tube. The distribution of gain for a set of 500 simulated TWTs in the presence of such errors is shown in Fig. 1.6. These fabrication errors were applied through random variations in the standard Pierce parameters: the velocity mismatch parameter b, the gain parameter C, and the cold-tube circuit loss parameter d. These parameters, as defined by Pierce, are described in detail in Section 2.3. The effects of these randomly distributed errors on the small-signal gain and phase were then studied [32]. Note that Pierce's gain formula for a uniform tube can no longer be used

because Pierce parameters are now random functions of axial position. Pengvanich devised a statistical analysis, showing that the standard deviations in the output gain and phase from the error-free value due to fabrication errors are linear in the standard deviation of the perturbations in the Pierce parameters. This work also showed that it was variations in the circuit phase that provided the greatest impact on the output gain and phase variations. A peculiar feature of Pengvanich's results is that a significant fraction of the samples with random errors show an output gain higher than that of the error-free free tube (Fig. 1.6), something that is not expected among manufactured TWTs. The resolution of this puzzling feature is a main part of this thesis [34].

The analysis performed by Pengvanich et al. considered only the three forward propagating modes inside the TWT. The effects of the Pierce "space charge" term (Section 2.3), QC, were also neglected. Most recently, these effects in the presence of fabrication errors have been considered. Sengele et al. [35] first adapted the analysis and technique of Pengvanich et al. [32] and included the effects of the Pierce space charge term. This work found that the presence of the space charge term reduced the significance of fabrication errors. Sengele then considered the effects of the backward wave in the presence of both random errors and the space charge term [36]. It was found that the random variations had a more significant effect in reducing the backward wave gain than the forward gain [36]. Since it is the backward wave that can cause oscillations in a traveling wave tube, it is thought that the significance of this result is that the random fabrication errors can damp the backward wave gain at a faster rate than the forward wave gain, thus making the amplifier more stable to oscillations. The backward wave, in the absence of space charge term effects, was considered by Chernin et al. [37]. This work emphasized the effects of *multiple* internal reflections due to the fabrication errors. These internal reflections were neglected by Sengele et al. [35, 36]. It was found that the presence of multiple

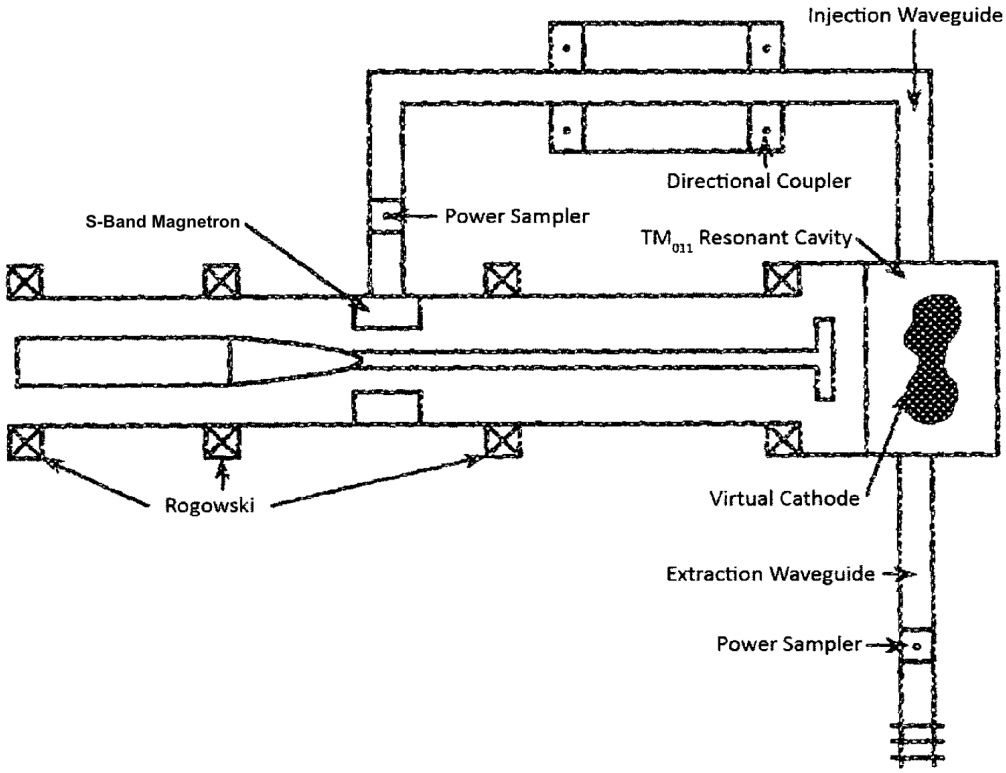

Figure 1.7: A schematic of the experiment of Price et al. [38] of a cavity vircator driven by a relativistic magnetron. Original image from [38].

internal reflections increased the mean and standard deviation in both the gain and phase from the error-free case compared to the results of the forward wave model. It was also found that multiple internal reflections lead to a small-signal gain ripple across the band of operation [37].

1.3.2 Locking of Magnetrons

Some of the earliest experiments on the phase locking using relativistic magnetrons were performed by Physics International Company. Price et al. first investigated the phase locking of a vircator by the injection of microwaves from a relativistic magnetron [38, 39]. A schematic of this experiment is shown in Fig. 1.7. The vircator, or virtual cathode oscillator, is a device that operates by injecting an electron beam through a foil or mesh anode into a resonant cavity. When the current is sufficiently high

that the limiting current is exceeded, the space charge passes through the anode and creates what is a known as a virtual cathode, a mass of space charge that reflects electrons, inside of the resonant cavity. The electrons from the virtual cathode are then subject to oscillations in the microwave frequency range, enhanced by the tuned resonant structure of the cavity. It was found that when the vircator would operate without the injected microwave signal, there was a frequency chirp that was present in its output. The experiments showed that when the relativistic magnetron signal was injected into the vircator cavity, the frequency would lock to that of the magnetron in $3-5$ ns and remain at that frequency [38, 39]. Furthermore, the power output of this configuration was $100-500$ MW, a factor of $2-3$ times higher than that of the vircator alone. A theory was developed by Woo et al. to describe the temporal frequency evolution by way of the classical Van der Pol oscillator equation [40]. The numerical solutions of Woo et al. in the presence of large priming power were found to be in agreement with the experimental results of the viractor injection locking.

The results of Woo et al. were also found to agree with the results of coupled relativistic magnetron experiments. These experiments by Benford and Sze et al. may be considered as the early peer-to-peer locking experiments with relativistic magnetrons [41, 42]. In these experiments, a small section of waveguide was used to couple a cavity of one magnetron to a cavity in the second magnetron. The coupling between the two relativistic magnetrons was found to be dependent on the length of this waveguide; the greatest locking was found to occur when the length of the waveguide was a multiple of the half wavelength [41]. The two oscillators, with power levels of approximately 1.5 GW each, would lock on the order of 5 ns producing around 3 GW of output power. This result was notable as it was three orders of magnitude higher than the power level of previous magnetron work at the time. Direct measurements of the radiation field showed evidence of the coherence enhancement of the output power. Sze et al. also investigated the peer-to-peer locking

of two vircators [43].

RF priming, where a low level external RF source is injected to more quickly build up the oscillations in a higher power RF source, was investigated by White et al. for a relativistic magnetron at the University of Michigan [44]. White et al. performed experiments in which a 100 kW pulsed 1.3 GHz magnetron was used to prime a $5-100$ MW, 1.2 GHz relativistic magnetron pulsed with a 300 kV, $2-8$ kA beam that lasts from $300-500$ ns. This investigation explored RF priming under conditions that both did and did not satisfy the classical Adler locking condition [45]. The Adler locking condition describes the power and frequency requirements for the phase locking of two magnetrons when one of the magnetrons (known as the "master") drives the other (known as the "slave"), as shown in Eq. (4.1). It was found that RF priming was successful at decreasing mode competition from the nearest mode (the $2\pi/3$ mode for this six cavity relativistic magnetron) even without satisfying the Adler locking condition. While successful, it was found that priming the magnetron via cathode priming [46], where the cathode is manufactured to emit current in a geometry conducive to π-mode startup or achieved by use of multiple cathodes [47], or magnetic priming [9, 11, 48, 49], where an azimuthally varying magnetic field is used for preferential selection of the π-mode, were more successful. The "transparent cathode", a hollow cathode with longitudinal strips removed, was invented at the University of New Mexico [50] and is another form of cathode priming.

These previous studies were all performed with relativistic magnetrons. Pengvanich and Neculaes et al. explored both the theoretical and experimental injection locking of two CW oven magnetrons [33, 51]. The model this work was derived from represented the oscillator as an RLC circuit and includes a magnetron specific electronic conductance and a frequency pulling parameter. This work explored injection locking in three different regimes: full locking, where the oscillator fully oscillates at the drive frequency; partial locking, where the oscillator tends to oscillate at both

the drive frequency and at its own free-running frequency; and zero locking, where the oscillator is not effected or marginally effected by the driver [51]. It was found that there was no locking when the drive power was far from the Adler locking condition and that full locking was achieved when the Adler condition was satisfied. The partial locking case was observed when the drive power was close to satisfying the Adler locking condition. In this case, the dominant frequency was either the driver frequency or close to it and sidebands in the magnetron spectrum would be observed. Using the model of [51], Pengvanich et al. explored the effects of a frequency chirp on injection locking [52]. It was found that complete phase locking of the oscillator cannot be achieved in the presence of a frequency chirp, in either the driver or the oscillator. What was observed, however, was that a high degree of locking will occur over a major duration of the frequency chirps.

The peer-to-peer locking of CW oven magnetrons was also theoretically studied by Pengvanich et al. [53]. Modeling the oscillators as RLC circuits connected through a general admittance matrix, a theoretical condition for the peer-to-peer locking of two magnetrons was derived. Experiments performed later by Cruz et al. validated the condition for peer-to-peer locking of Pengvanich [54]. These experiments used two kilowatt magnetrons and found, depending on the coupling network between them, that the oscillators would not necessarily lock to a frequency that lie between the free-running frequencies of the two magnetrons. It was also found that if the locking condition of [53] was not satisfied, beating of the frequency was apparent in the magnetron spectra, although the beat frequency was not necessarily the difference between the free-running frequencies of the two oscillators.

1.4 Thesis Organization

This thesis provides an extension of some of the above studies. In Chapter 2 the effects of TWT performance in the presence of random manufacturing errors is

investigated using a model that considers only the three forward propagating waves. Two analytic formulas are presented and compared to numeric computations. In Chapter 3, validation of the algorithm used to study TWT performance with the inclusion of the backward wave in the presence of random manufacturing errors is presented. A consideration of the presence of absolute instabilities inside of a slow wave structure is included as well. Chapter 4 explores the temporal and spatial locking of nonlinear oscillators. The temporal locking of peer-to-peer locked magnetrons in the presence of a frequency chirp and low frequency noise is investigated. A framework for interpreting locking in the spatial domain that is analogous to locking in the temporal domain is presented. Chapter 5 contains conclusions of this research and recommendations for future work.

CHAPTER 2

Effects of Random Errors in a Traveling Wave Tube: Three Wave Model

2.1 Introduction

The traveling wave tube is a key element in telecommunication systems, satellite-based transmitters, military radar, electronic countermeasures, and communication data links [1, 3, 14, 55, 56]. Variations in performance due to finite fabrication tolerances in the manufacturing process can lower the fraction of TWTs that meet specifications and drive up the cost of manufacturing [57, 58]. Errors as large as 5 μm on 50 μm features have been reported in the fabrication of TWTs in the hundreds of GHz range using modern manufacturing techniques [33, 56]. One consequence of such errors is that it will alter the phase velocity of the circuit, which degrades the TWT performance significantly. These errors produce proportionately larger perturbations to the circuit as the circuit size is reduced. Their effects on the small-signal gain and output phase have been studied by Pengvanich et al. [32] who considered the evolution of the three forward waves in a TWT in which the Pierce parameters (Section 2.3) vary randomly along the tube axis. A peculiar feature of the results in [32] is that, in the statistical evaluation of a large number of samples with random errors in the circuit phase velocity, a significant number of these samples show an output gain that

is higher than the corresponding error-free tube (Fig. 1.6). It is this intriguing feature that prompted the analysis of the expectation values of the gain and phase reported in this thesis [34]. As we shall see shortly, an explanation of this statistical feature is provided in this chapter. Pengvanich et al. [32] is also extended to include AC space charge effects and non-synchronous interactions. We shall ignore the effects of the reverse propagating circuit wave, which we also recently analyzed [37]; some of these results will be discussed in further detail in Chapter 3. In Chernin et al. [37], we found that reflections from local errors may significantly increase the statistical effects on the gain and the output phase. Effects on the TWT backward-wave mode [59] by random manufacturing errors were also recently analyzed [36].

The standard deviations in the gain and in the output phase, which were analytically calculated in Pengvanich et al. [32], required only an account of the first order effects of random errors. The expected mean of the output gain and phase, which is the focus here, requires consideration of the second order effects of random errors, and is therefore much more difficult to evaluate. Since deviation from the mean (a second order effect) is much less than the standard deviation (a first order effect), a significant number of the samples in a statistical analysis would naturally show an output gain that is higher than the corresponding error-free tube, as shown in Fig. 1.6. Three approaches are used to analyze this problem. The first approach is analytical where successive perturbations are applied on all three forward waves. The second approach is also analytical where only the dominant, growing mode is included in the analysis. The third approach is purely numerical where the governing differential equation is numerically integrated (at least) 5000 times, each time with unique, random variation in the coefficients that represent random axial variations in the circuit phase velocity. Comparison of these three approaches is presented.

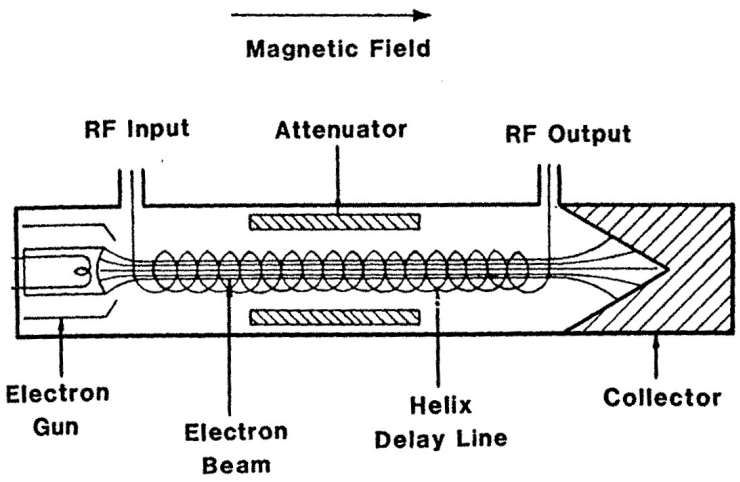

Figure 2.1: The basic schematic of a TWT. It consists of a few components: electron gun, collector, and slow wave structure. Image from [1].

2.2 Basic Description of the TWT

The basic operation of a TWT was discussed briefly in Section 1.2.1. Here we quantify some of the features of Fig. 2.1, which shows an electron beam that travels down the axis of a helix TWT with a velocity of $v_0 = \sqrt{2eV/m_e}$, where e is the electron charge, m_e is the electron mass, and V is the voltage applied to the cathode via an external power supply. Pierce adopted a non-relativistic description for TWTs, which is adequate for beam energy $\lesssim 40$ keV. At the end of the TWT, the beam is dumped into a collector and some of the kinetic energy of the spent beam is recovered. Typically, a multistage depressed collector is used to apply a bias that slows the velocity of the electron down before it is collected at the wall. Collectors can cause the efficiencies of TWTs to be upwards of 70% [60]. Since the beam travels at a velocity less than the speed of light, for the beam to synchronously interact with an electromagnetic wave, the wave speed in the axial direction needs to be slowed down. This is accomplished through the use of a slow wave structure, e.g., a helix slow wave structure as shown in Fig. 2.1. Other slow wave structures include folded wave-guide, coupled-cavity, and ladder circuits [1, 61–63]. To the lowest order, the RF signal

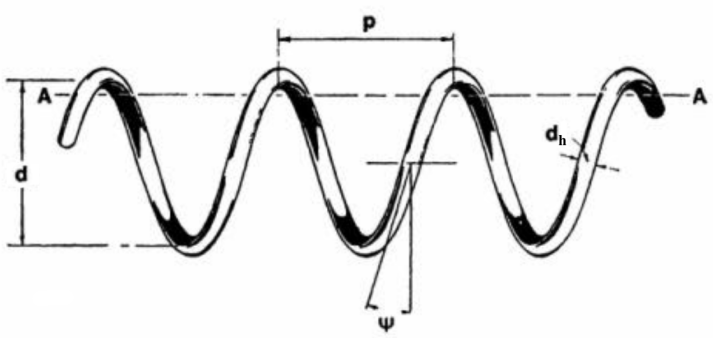

Figure 2.2: The geometry of a helix slow wave structure with the key dimensions labeled. Here, d is the diameter of the helix, p is the helix pitch (or period), ψ is the helix pitch angle, and d_h is the wire diameter. Original image from [1].

propagates along the helix wire at the speed of light. The projected signal velocity along the tube axis can then be reduced to be less than c, so that this z-directed phase velocity can be of the order of the electron beam drift velocity. This axial velocity is known as the cold circuit phase velocity, v_p. For a helix, this axial phase velocity is simply $v_p = c(p/\sqrt{p^2 + (\pi d)^2})$, where p is the helix pitch (period) and d is the helix diameter (Fig. 2.2). A very important feature of this phase velocity is that it is independent of frequency. For this reason, the helix TWT can offer bandwidths up to 3 octaves, where an octave is a doubling of frequency [5]. Attenuators, commonly in the form of a carbon film coating on the dielectric support rods (see Fig. 1.5) [1], can be inserted into the interaction area to give the amplifier stability from oscillations [64] and an external magnetic field, typically through the use of periodic permanent magnets (PPM), is applied to confine and focus the electron beam and prevent it from intercepting the slow wave circuit [65].

When the beam velocity (v_0) and the axial component of the circuit wave velocity (v_p) are approximately equal, $v_0 \approx v_p$, the electrons can continuously interact with the wave. If the electrons spend more time in the decelerating phase of the wave, such that they give up their kinetic energy, then amplification of the wave can occur as the two co-move down the axis of the TWT. In the absence of the beam, the RF

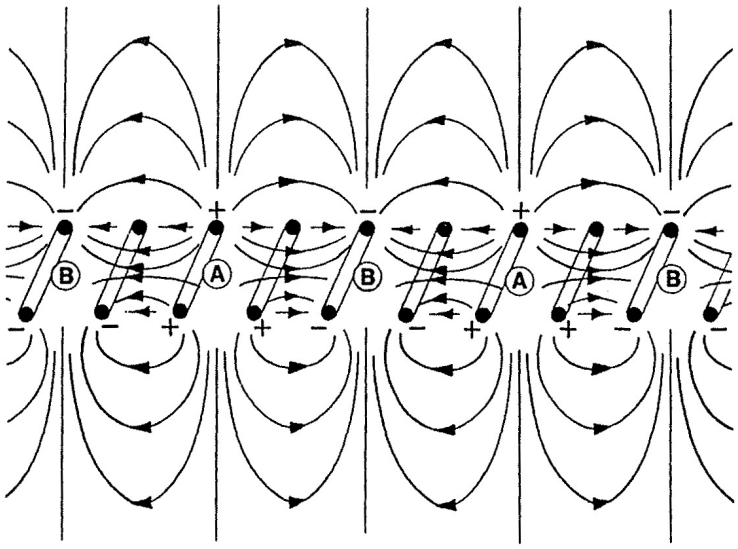

Figure 2.3: The vacuum electric field of an RF signal on a helix slow wave structure, in the frame of the wave. The electrons will experience the strong axial component of this field and bunch in regions A and deplete regions B. Image from [1].

signal on the helix circuit sets up the vacuum electric field, similar to that shown in Fig. 2.3. This field has a strong axial component, and it is this component that interacts most strongly with the electron beam. In Fig. 2.3, the electric field lines point along the axis, away from regions A and towards regions B. This electric field velocity modulates the beam and causes the electrons to deplete in regions B and bunch in regions A. This bunching of space charge enhances the electric field on the helix by inducing more current on the circuit. This amplitude increase in the helix field in turn causes greater bunching of the electron beam. It is this interaction that is the mechanism for amplification of an input RF signal. The output power is then determined from the product of the AC voltage and the AC induced current at the RF extraction [55].

From the axial fields shown in Fig. 2.3, assuming that the electron beam travels from left to right, electrons to the left of regions A will be *accelerated* towards regions A and electrons to the right of regions A will be *decelerated* towards regions A. If the

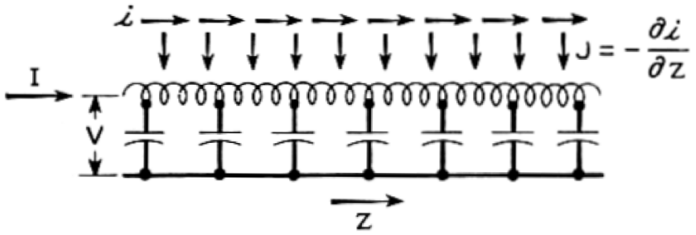

Figure 2.4: The transmission line model of the slow wave circuit used by Pierce. Image from [14].

electrons are accelerated they take energy from the RF wave, but if the electrons are decelerated they give up energy to the wave. From this picture we can see that if the electron beam travels faster than the wave phase velocity, the electrons spend more time in the decelerating phase resulting in a net transfer of energy to the wave.

2.3 Pierce Theory of TWTs

In this section we present the standard TWT theory of Pierce. Pierce modeled the slow wave circuit of the TWT as a transmission line that extends infinitely in the z-direction, as shown in Fig. 2.4 [14]. A narrow electron beam carrying an AC current, i, passes close to the circuit at a speed that is approximately matched with the wave speed of the circuit. The beam induces a current, I, and voltage, V, on the circuit. The electron beam experiences the voltage on the circuit and the electrons become further modulated. It is assumed that the electrons in the beam all experience the same AC field and that the electron beam is monoenergetic in the unperturbed state. Pierce further assumes that there is an infinite magnetic field confining the electrons to 1-dimensional motion in the z-direction.

The equations for electronic motion and for excitation of the circuit wave can be combined to determine the propagation characteristics of the waves. Pierce linearizes these equations. This assumption is valid only in the small signal regime of the amplifier, where certain quantities do not have a significant role when the signal

amplitude is small. This results in a wave-type solution, so we assume that the solutions have $e^{j\omega t - j\beta z}$ dependence, where β is the propagation constant which needs to be determined for an input signal of frequency ω.

The linearized force law describes the displacement (s) of an electron fluid element from its unperturbed position in response to the electric field,

$$\left(\frac{\partial}{\partial t} + v_0 \frac{\partial}{\partial z}\right)^2 s = -\omega_p^2 s - \frac{e}{m_e} E_c. \tag{2.1a}$$

The left-hand side (LHS) of Eq. (2.1a) represents the acceleration where v_0 is the electron velocity in the unperturbed (DC) state. The right-hand side (RHS) of Eq. (2.1a) represents the combined force due to the space charge field, represented by ω_p^2, and the circuit electric field, represented by E_c. The plasma frequency of the electron beam, ω_p, includes the "reduction factor" which accounts for the beam and the circuit geometry [55, 66]. In the absence of the circuit field, $E_c = 0$, and Eq. (2.1a) gives the familiar space charge wave dispersion relation for an electron beam: $(\omega - \beta v_0)^2 = \omega_p^2$.

For a signal of frequency ω, Pierce re-writes Eq. (2.1a) as

$$\left[\left(\frac{\partial}{\partial z} + j\beta_e\right)^2 + \beta_q^2\right] s = a, \tag{2.1b}$$

where $a = -eE_c/(m_e v_0^2)$ represents the circuit field, $\beta_e = \omega/v_0$ is the propagation constant which characterizes the beam's DC velocity v_0, and $\beta_q = \omega_p/v_0$ is the reduced space-charge wavenumber that characterizes the beam's AC space charge effects. In the absence of the AC space charge effects, $\beta_q = 0$, and Eq. (2.1b) is identical to Eq. (1) of Pengvanich et al. [32].

The slow wave circuit equation of Pierce describes the circuit's response to the AC current on the electron beam. It reads

$$\left(\frac{\partial}{\partial z} + j\beta_p + \beta_e C d\right) a = -j\left(\beta_e C\right)^3 s, \tag{2.2}$$

where $\beta_p = \omega/v_p$ is the cold circuit wavenumber, and v_p is the cold circuit phase velocity, that is the phase velocity of the wave on the circuit in the absence of the electron beam. Equation (2.2) is the corrected form of Eq. (2) of Pengvanich et al. [32]. The third term on the LHS of Eq. (2.2) should read $\beta_e Cd$ instead of $\beta_p Cd$, a typo in Pengvanich et al. [32] that has propagated through the literature. Equation (2.2) describes the excitation of the circuit electric field (a) by the AC current on the electron beam, represented by the RHS of Eq. (2.2). The beam's AC current, in the linear theory, is proportional to the electronic displacement, s, and to the DC beam current which is proportional to C^3 in the RHS of Eq. (2.2), where C is defined in Eq. (2.3) below [1, 14, 55]. In the absence of the beam current, $C^3 = 0$ and Eq. (2.2) yields a forward propagating circuit wave, $a = (\text{const.}) \times e^{-j\beta_p z - \beta_e C d z}$, where d denotes the resistive loss on the circuit. We assume, as Pierce does, that by writing Eq. (2.2), we neglect the backward wave that is present on the circuit. This is justified since the backward wave does not experience the cumulative interaction with the electron beam as the forward circuit waves do. Thus, Eq. (2.2) admits one propagating circuit wave in the positive z-direction, whereas Eq. (2.1b) represents two beam modes, also propagating in the positive z-direction. This constitutes the three-wave theory of Pierce.

The interaction of the three forward waves is characterized by four (4) dimensionless parameters: C, b, QC, and d, defined below. These are known as the Pierce parameters. The first of these parameters is the Pierce dimensionless gain parameter, C, and it characterizes the coupling between the beam modes, Eq. (2.1b), and the circuit mode, Eq. (2.2),

$$C^3 = \frac{1}{4}\frac{K I_b}{V_b}, \tag{2.3}$$

where K is the interaction impedance of the circuit, I_b is the DC current of the electron beam, and V_b is the electron beam voltage. The interaction impedance, K,

is roughly the AC voltage induced on the circuit by 1 A of AC current on the beam. Thus, to increase coupling between the beam and the wave, either the interaction impedance of the circuit or the beam current should be increased. The Pierce gain parameter, C, typically has a value between 0.01 to 0.2.

The next dimensionless parameter is known as the velocity mismatch or detune parameter, b,

$$b = \frac{1}{C}\left(\frac{v_0 - v_p}{v_p}\right). \tag{2.4}$$

The difference between the DC beam velocity, v_0, and the circuit wave phase velocity, v_p, is measured by b. When the electron beam is synchronous with the cold circuit phase velocity, $b = 0$. Of the four Pierce parameters (C, b, QC, and d), it is the velocity detune parameter, b, to which the output of the TWT is the most sensitive. Typically, v_b differs from v_p by not more than $\pm 10\%$; and $-2 < b < 2$.

Pierce introduces his space charge parameter, QC, to describe the electrostatic repulsion among the space charges on the beam. He defines his space charge parameter as

$$QC = \frac{1}{4}\frac{\beta_q^2}{\beta_e^2 C^2}. \tag{2.5}$$

The effect of the QC term is to reduce the gain that the TWT can achieve by limiting how tightly a bunched beam can be formed. Since $QC \propto \omega_p^2/\omega^2$, it is expected that this value will be quite small in the terahertz regime. In terms of the beam current (I_b), both C and QC are proportional to $I_b^{1/3}$.

Finally, Pierce describes the loss on the circuit of the TWT through his dimensionless loss parameter, d, which he defines as

$$d = 0.0184\, l/C, \tag{2.6}$$

where C is the gain parameter and l is the resistive loss on the circuit in units of dB per wavelength.

Combining Eqs. (2.1b) and (2.2) and assuming $e^{-j\beta z}$ dependence for a and s, results in a third order algebraic equation for the propagation constant β, shown in Eq. (2.7) below. Each β corresponds to the propagation constant associated with the three forward propagating waves that can be excited in the TWT. Assuming that the Pierce parameters are constant, this result is known as the Pierce dispersion relation and it reads, after substituting Eqs. (2.3) - (2.6) [1, 14, 55],

$$\left(\delta^2 + 4QC\right)\left(\delta + jb + d\right) = -j, \tag{2.7}$$

where $\delta = -j(\beta - \beta_e)/C\beta_e$ is Pierce's incremental propagation constant. There are three solutions in Eq. (2.7) for the propagation constant, δ, representing the three forward waves in the Pierce three-wave theory of TWTs that can be excited by some input signal. Of these three waves, as determined by Eq. (2.7), one will grow exponentially as a function of distance, one will exponentially decay as a function of distance, and one will have a constant amplitude in the absence of circuit losses.

The incremental propagation constant, δ, is in general complex. The real and imaginary parts of δ, from the solution to Eq. (2.7), gives important information about the waves. The real part, $\mathrm{Re}(\delta)$, shows how the amplitude of the wave changes as it propagates. If $\mathrm{Re}(\delta) > 0$, then the wave exponentially grows in amplitude as it propagates in the z-direction whereas, if $\mathrm{Re}(\delta) < 0$, then the wave decays as it propagates in the z-direction. The imaginary part, $\mathrm{Im}(\delta)$, indicates the phase speed of the wave relative to that of the electrons. If $\mathrm{Im}(\delta) > 0$, the wave travels faster than the electrons and if $\mathrm{Im}(\delta) < 0$, the wave travels slower than the electrons. Figure 2.5 shows the real and imaginary parts of the solution to Eq. (2.7), $\delta = \mathrm{Re}(\delta) + j\mathrm{Im}(\delta)$, for the growing mode only as a function of the Pierce velocity mismatch parameter, b, for a case with zero circuit loss ($d = 0$) and zero AC space charge effects ($QC = 0$).

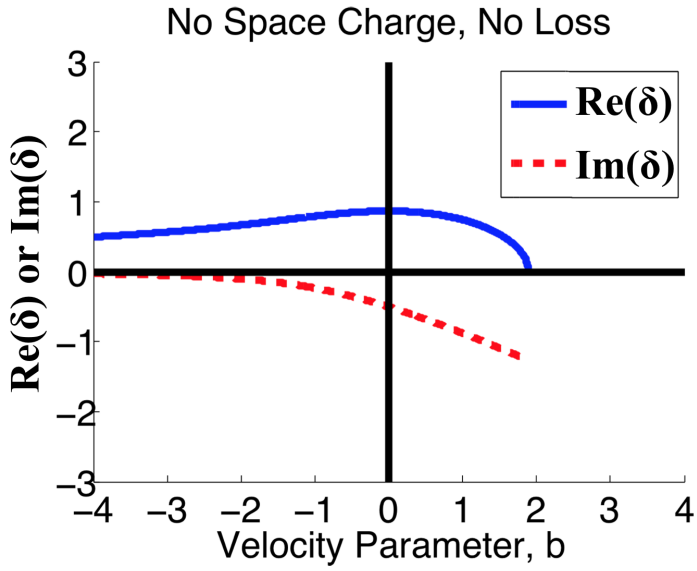

Figure 2.5: Real and imaginary parts of the propagation constant, $\delta = \mathrm{Re}(\delta) + j\mathrm{Im}(\delta)$, for the growing mode in the absence of loss or space charge effects ($d = 0, QC = 0$).

In this case we can see that $\mathrm{Re}(\delta)$ is positive for a wide range of b. Figure 2.5 also shows that $\mathrm{Im}(\delta)$ is negative where there is amplification, so the wave travels more slowly than the electron beam, even when the electron beam is slower than the cold tube circuit phase velocity, $b < 0$. This occurs because the electrons need to travel faster than the wave for amplification to occur. In this case, no gain occurs for values of $b > 2$.

2.4 Three Wave Model with the Inclusion of the QC Term and Nonzero b

We follow the model of Pengvanich et al. [32] which is based on Pierce's theory except that the assumption of axial uniformity in the circuit parameters has been relaxed. When the quantities β_p, C, or d are allowed to vary axially, Eq. (2.7) is no longer applicable. Returning to Eqs. (2.1b) and (2.2) and relaxing the assumption that β_p, C, or d are constant, a third-order ordinary differential equation that governs

the evolution of the input signal in the TWT can be derived. It reads

$$\frac{d^3f(x)}{dx^3}+jC\left(b-jd\right)\frac{d^2f(x)}{dx^2}+4QC^3\frac{df(x)}{dx}+jC\left(4QC^3\left(b-jd\right)+C^2\right)f(x)=0, \quad (2.8)$$

where $x=\beta_e z$ is the normalized axial distance, and $f(x)=e^{jx}s(x)$ represents Pierce's three-wave solution to the third-order ordinary differential equation (2.8). In the absence of AC space charge effects, $QC=0$, and Eq. (2.8) reduces to Eq. (5) of Pengvanich et al. [32]. We solve Eq. (2.8) subject to the initial conditions at the TWT input ($x=0$),

$$f(0)=0, \quad (2.9a)$$

$$f'(0)=0, \quad (2.9b)$$

$$f''(0)=1, \quad (2.9c)$$

which represent, respectively, zero AC current, zero AC velocity, and an arbitrary amount of initial AC electric field, which we choose to be unity in the present linear theory. The change in the amplitude gain, G_1 in e-folds, and in the phase, θ_1 in radians, due to random errors is given by,

$$e^{G_1+j\theta_1}=\frac{f''(x)+4QC^3f(x)}{f_0''(x)+4QC^3f_0(x)}, \quad (2.10)$$

where f_0 represents the solution to Eq. (2.8) for an error-free tube and the prime denotes differentiation with respect to x. From Eq. (2.1b), we see that Eq. (2.10) is simply $a(x)/a_0(x)$, where $a_0(x)$ is the error-free solution of the normalized circuit wave complex amplitude, $a(x)$.

Finally, we revise the standard deviation of gain and phase variations calculated in Pengvanich et al. [32] to include the space charge effects ($QC\neq 0$). In terms of the

standard deviation of b, σ_b, the standard deviation in the gain G_1 and in the phase θ_1 is given by, respectively,

$$\sigma_{Gb} = S_{Gb}\sigma_b,\ S_{Gb} = \sqrt{\frac{x}{N}}\sqrt{\int_0^x ds \left|g_{br}(x,s)\right|^2} \tag{2.11a}$$

and

$$\sigma_{\theta b} = S_{\theta b}\sigma_b,\ S_{\theta b} = \sqrt{\frac{x}{N}}\sqrt{\int_0^x ds \left|g_{bi}(x,s)\right|^2}, \tag{2.11b}$$

where g_{br} and g_{bi} are the real and imaginary parts, respectively, of g_b, given by

$$g_b(x,s) = -jC\left(4QC^3 f_0(s) + a_0(s)\right) a_0(x-s)/a_0(x). \tag{2.12}$$

In the absence of space charge, i.e., $QC = 0$, Eq. (2.12) reduces to Eq. (A15) of Pengvanich et al. [32], whose Eq. (A4) defines the error-free solutions f_0 and a_0.

Equations (2.11) show that the standard deviations in the gain and phase are linear in σ_b. It will be shown in Eqs. (2.13) and (2.14) below that the ensemble averaged quantities, $\langle G_1(x)\rangle$ and $\langle \theta_1(x)\rangle$, are both *quadratic* in σ_b, and their magnitudes are therefore much less than the standard deviations. This contrast between the standard deviation, and the deviation in the mean from the error-free tube, was also apparent in Fig. 1.6.

2.4.1 Second-Order Perturbation Analysis

The random manufacturing errors enter the Pierce parameters b, d, and C. It has been shown that the effects of random errors in the velocity parameter, b, dominates those of random errors in d and C [32], so we only consider random errors in b in this thesis. Random errors are assigned to $b(x)$ as a set of Gaussian random variables

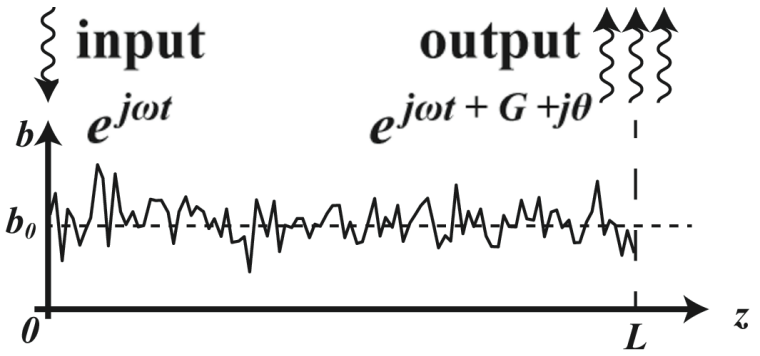

Figure 2.6: Sample velocity mismatch profile with a mean value of b_0 of a TWT of length L.

uniformly spaced in x, each with a mean of b_0 and a specified standard deviation, σ_b, as illustrated in Fig. 2.6. We define the correlation length as $\Delta = L/N$, where N is the number of uniformly spaced nodes over the normalized length (L) of the TWT. The random variation in neighboring segments have no correlation to each other. That is, the random variation in one segment has no "memory" beyond the correlation length.

This work differs from the previous work of Pengvanich et al. by applying the random Gaussian errors directly to the parameter b, instead of to the circuit phase velocity v_p through a dimensionless quantity $q(x) = (v_p(x) - v_{p0})/v_{p0}$, where v_{p0} is the circuit phase velocity of the corresponding error-free tube. The random function $q(x)$ had a specified standard deviation σ_q. The velocity parameter b is related to q by $b(x) = (1/C)[Cb_0 - q(x)]/(1 + q(x))$ and the standard deviations in b and q are *approximately* related by $\sigma_b = (\sigma_q/C)(1+Cb_0)$. Due to the non-linear relationship between b and q, a Gaussian random error profile assigned to $q(x)$ is no longer Gaussian for $b(x)$. Our numerical integration of Eq. (2.8) over many 5000-sample calculations shows that this subtle difference led to quantitatively different results. One reason is that the mean deviation is a second order effect in the random error, as we have already mentioned, and this subtle difference is important. In this work, all random errors are characterized by a Gaussian distribution in $b(x)$ with a standard deviation

of σ_b.

Pengvanich et al. showed analytically that the standard deviations in the gain and in the output phase from an error-free TWT are first order in σ_b (cf. Eqs. (2.11) above). In this work, we need to carry out the analysis to second order in the effects of the random errors. With only perturbations in b, we show in Appendix A (cf. Eq. (A.16)),

$$\langle G_1(x) + j\theta_1(x)\rangle = -\frac{1}{2}C^2\sigma_b^2\Delta\Bigg\{\left[4QC^3\sum_{l=1}^{3}\frac{\tau_l}{C\delta_l} + \sum_{k=1}^{3}\tau_k C\delta_k\right]\int_0^x \frac{Q_1(x,s)ds}{a_0(x)} + \sum_{l=1}^{3}\sum_{k=1}^{3}\left(\tau_l C\delta_l\right)\left(\tau_k C\delta_k\right)e^{C(\delta_l+\delta_k)x}\int_0^x \frac{Q_2(x,s)ds}{a_0^2(x)}\Bigg\}, \tag{2.13}$$

where $\langle G_1(x) + j\theta_1(x)\rangle$ is the ensemble-average deviation in gain and in phase from the error-free tube due to random errors, $\delta_k (k = 1, 2, 3)$ are the three roots to the Pierce dispersion relation (2.7), $\tau_k (k = 1, 2, 3)$ which depends only on δ_k, is defined by Eq. (A5) of Pengvanich et al. [32], and $Q_1(x, s)$, $Q_2(x, s)$ depend only on the error-free, three-wave solution. The expressions for $Q_1(x, s)$, $Q_2(x, s)$ are given in Appendix A in Eqs. (A.17), (A.18). Use of Eq. (2.13) will be referred to as the **perturbation** method. It is emphasized once more that the deviation from the mean, for both gain and phase as given by Eq. (2.13), is second order in σ_b.

2.4.2 Nonlinear Formulation of Complex Wavenumber

In addition to the perturbation method, another analytic approach to predict the ensemble average deviation in gain and phase was developed by Professor Tom Antonsen, Jr. at the University of Maryland [34]. This approach consists of a nonlinear formulation of the complex wavenumber for *only* a single wave (the growing mode). The result of this formulation yields

$$\langle G_1(x) + j\theta_1(x) \rangle = -\frac{\rho(\gamma)}{2} \left(\frac{C}{1 + Cb_0} \right)^2 \sigma_b^2 x \Delta, \tag{2.14}$$

where $\rho(\gamma)$ is a complex value that is determined by the value of the error-free mismatch parameter, b_0, and can be solved for using

$$\rho(\gamma) \equiv \frac{2\gamma^2 (\alpha - j\gamma)}{\left[1 + 2\gamma^2 (\alpha - j\gamma)\right]^2} \tag{2.15}$$

where $\alpha \equiv b_0/(1 + Cb_0)$. The details on how Eq. (2.14) was obtained can be found in Rittersdorf et al. [34]. The value of γ is determined by solving the dispersion relationship

$$\gamma \left[\left(\gamma + \frac{ib_0}{1 + Cb_0} \right)^2 + 4QC \right] = j, \tag{2.16}$$

which is essentially the Pierce dispersion relation Eq. (2.7), assuming $d = 0$, and written in a slightly different form. Physically, Eq. (2.16) represents the coupling between the forward circuit wave (represented in the LHS by the first term γ) and the two forward beam modes including space charge effects, QC (represented by the square brackets in the LHS). Use of Eq. (2.14) will be referred to as the **Riccati** method. The details of Antonsen's work can be found in Appendix B of [34]. Note that if $b_0 = 0$ and $QC = 0$, then $\alpha = 0$, $\gamma^3 = j$, and ρ is real by Eq. (2.15), in which case $\langle \theta_1 \rangle = 0$ by Eq. (2.14), as in the example in Fig. 2.9 below. It is important to note that Eq. (2.14) is also second order in σ_b, similar to Eq. (2.13).

2.4.3 Numerical Solution

For a specified value of σ_b, we may also integrate Eq. (2.8) numerically using a Runge-Kutta method 5000 times, each time with a unique, random profile for the circuit phase velocity. Previous work [32] showed that performing only 500 integrations would be sufficient. That work, however, was only focused on calculating the stan-

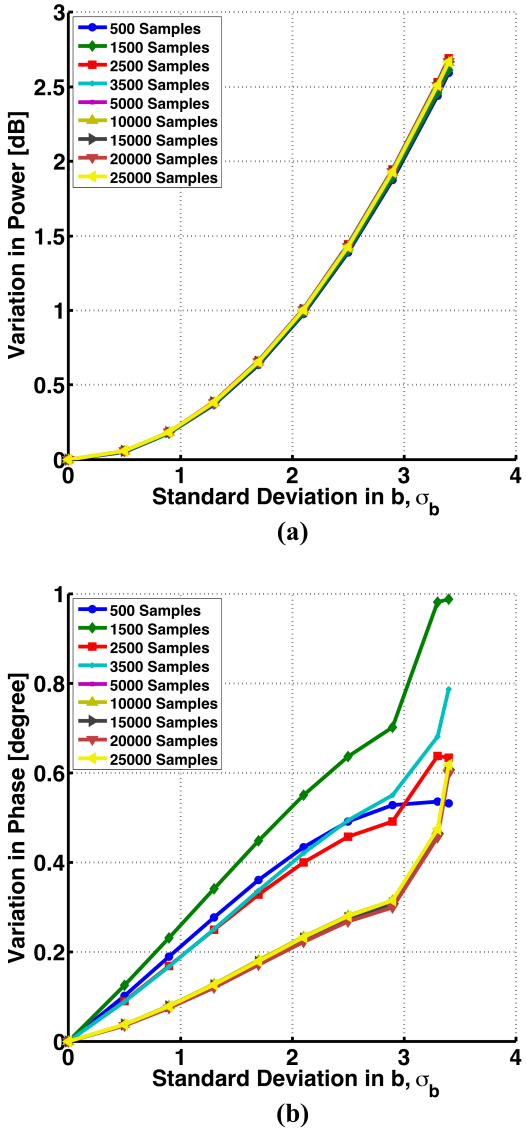

Figure 2.7: Mean values of the (a) power and (b) phase at the output relative to the unperturbed values at the output for a synchronous beam velocity as a function of the standard deviation of the error profile, σ_b, for several different sample sizes. Here, $x = 100, b_0 = 0, C = 0.05, \Delta = 1, d = 0$, and $QC = 0$.

dard deviation in gain and phase, which is first order in σ_b (Eqs. (2.11)). While 500 integrations are sufficient to calculate these standard deviations, significantly more are required to calculate the mean accurately, since the deviation from the mean is second order in σ_b (Eqs. (2.13), (2.14)). Figure 2.7 shows the mean gain and phase variation as a function of σ_b for sample sizes ranging from 500 up to 25,000. As can

be seen from Fig. 2.7, 5,000 samples provides converged results, meaning increasing the number of samples does not significantly change the result. It is also worth noting that 500 samples is sufficient for the calculation of the mean variation in the gain; the phase, however, requires 5,000 samples for convergence. Calculations performed in this manner will be designated as **numerical**. One important note is that this numerical calculation is dependent on the random number seed used in these calculations. Different seed values do not produce a difference in the mean gain output, however, the exact values for the output phase will be different albeit of the same order. In all of the following calculations, the seed used for the random number sequence has been fixed.

2.5 Results

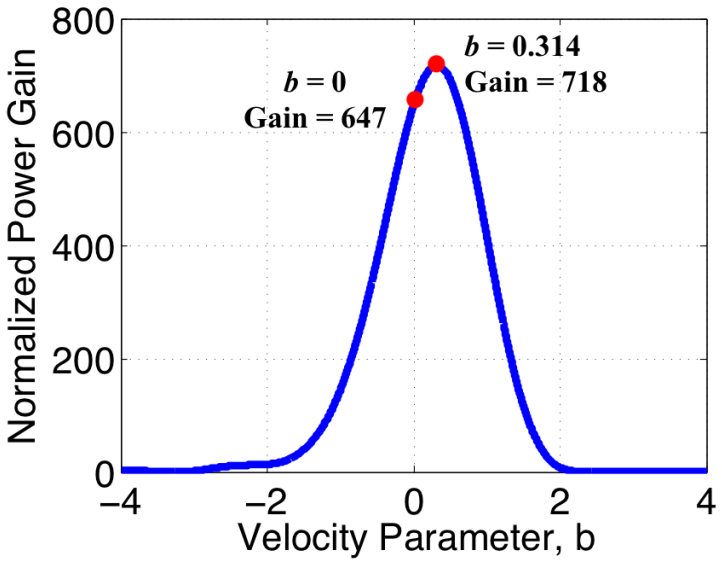

Figure 2.8: Gain of a TWT as a function of the dimensionless Pierce velocity parameter, b. The peak gain occurs at a value of $b_0 = 0.314$. At synchronism, $b_0 = 0$, the gain is 647, or 28.1 dB.

We start with the TWT base case with length $x = L = 100$ where $b_0 = d = QC = 0$, and $C = 0.05$. This could correspond, for example, to a microwave power module TWT that has a 21.6 cm circuit length, a beam voltage of $V_b = 5$ kV, a beam current

of $I_b = 260$ mA, and is operating at a frequency of 3 GHz [56]. This was also the base case studied by Pengvanich [32]. Equation (2.8) yields an error-free power gain of 28.1 dB and an output phase of -5872°. Random errors are then introduced into the velocity parameter, b, as shown in Fig. 2.6. The value at each node is an independent Gaussian random variable with a mean of b_0 and a specified standard deviation, σ_b. A correlation length of $\Delta = 1$ has been used in all calculations, meaning that each node of the Gaussian random error profile would correspond to $x = 1, 2, \ldots, L$ in the TWT. It is worth noting that this base case of $b_0 = 0$ does not provide the maximum amount of gain for this set of TWT parameters. We can see from Fig. 2.8, which shows TWT gain as a function of b, that the optimum gain occurs at a point $b_0 = 0.32$. This implies that the beam velocity v_0 is 1.6% larger than the cold circuit phase velocity v_p. See also Fig. 2.5.

Figure 2.9a shows the gain variations for the numerical, perturbation, and Riccati methods. All three methods show good agreement. The phase calculation is shown in Fig. 2.9b. The perturbation method shows good agreement with the numerical results. It should be noted that in this case $\langle \theta_1(x) \rangle = 0$ for the Riccati method (cf. the second to last sentence in Section 2.4.2). This result is consistent with those from the perturbative analysis and the numerical solution to Eq. (2.8), in that the phase variations $\langle \theta_1(x) \rangle$ due to random errors, measured in radians, is found to be negligible compared with the amplitude variations $\langle G_1(x) \rangle$, measured in e-folds, in this case. This case is identical to the one considered by Pengvanich et al. [32].

Figure 2.10 shows two cases where the velocity mismatch is nonzero. For $C = 0.05$, $b_0 = \pm 1$ corresponds to a difference of $\pm 5\%$ between the beam velocity and cold circuit phase velocity. All three methods are in reasonable agreement even when the velocity mismatch is allowed to be nonzero. Looking at the phase output (Fig. 2.10b) it appears that the perturbation method is more accurate than the Riccati method.

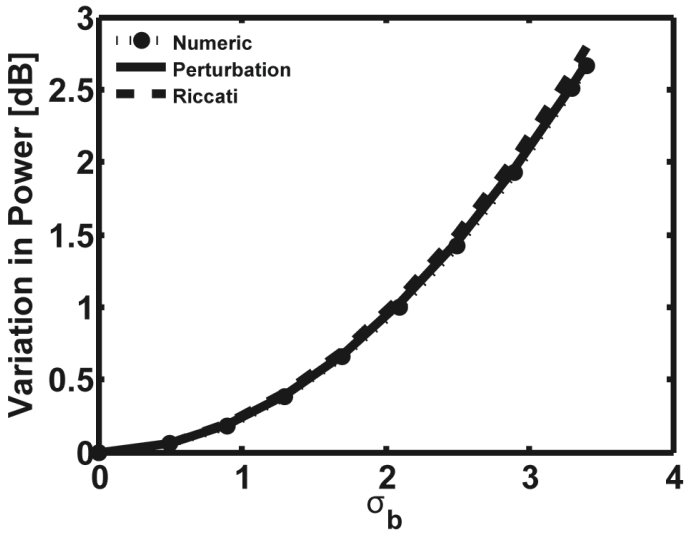

(a)

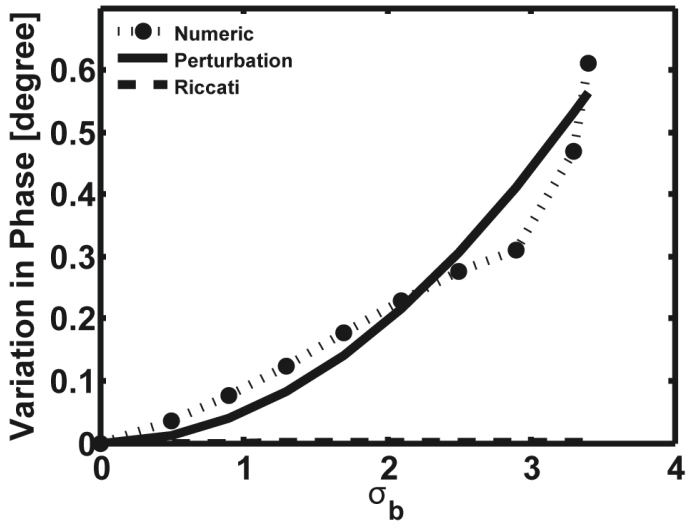

(b)

Figure 2.9: Mean values of the (a) power and (b) phase at the output relative to the unperturbed values at the output for a synchronous beam velocity, $b = 0$. The points are the results of numerically integrating Eq. (2.8). The solid and dashed lines show the perturbation and Riccati formulas, Eqs. (2.13) and (2.14), respectively. Here, $x = 100, C = 0.05, \Delta = 1, d = 0$, and $QC = 0$.

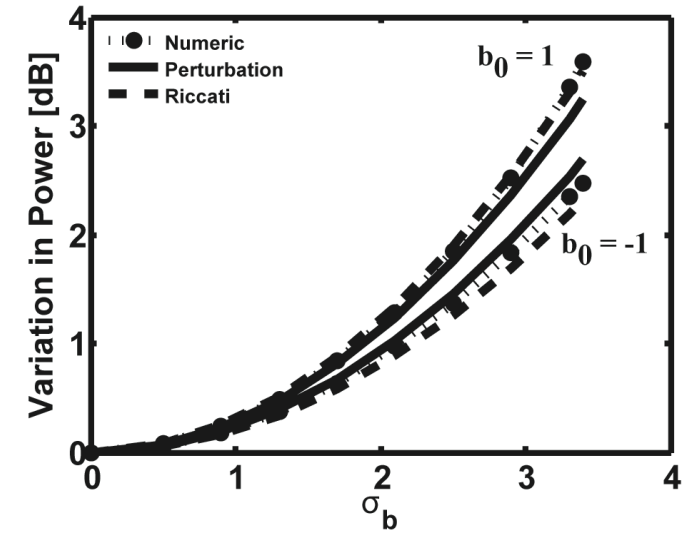

(a)

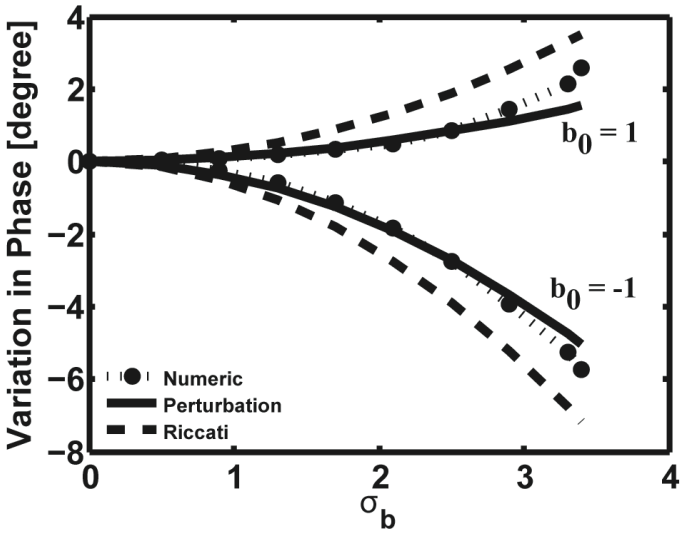

(b)

Figure 2.10: Mean values of the (a) power and (b) phase at the output relative to the unperturbed values at the output for non-synchronous beam velocities of $\pm 0.05 v_p$ ($b = \pm 1$). The points are the results of numerically integrating Eq. (2.8). The solid and dashed lines show the perturbation and Riccati formulas, Eqs. (2.13) and (2.14), respectively. Here, $x = 100, C = 0.05, \Delta = 1, d = 0$, and $QC = 0$.

2.5.1 Mean Variations in the Presence of the Space Charge Term

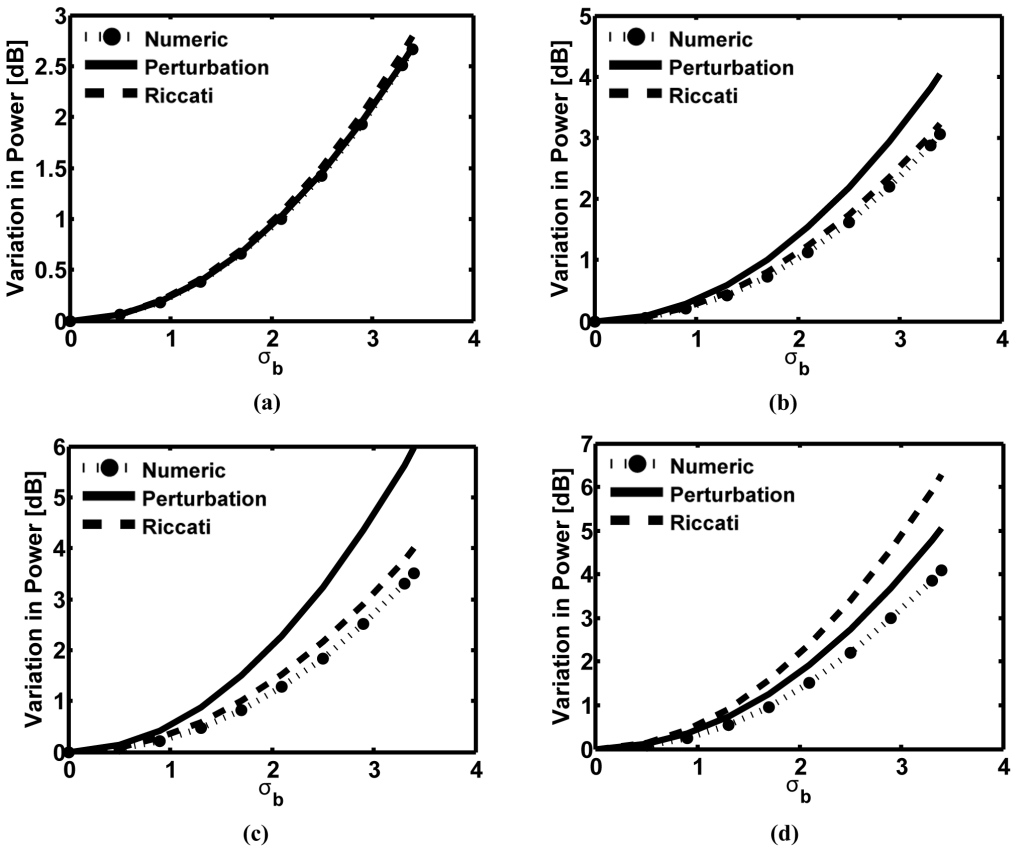

Figure 2.11: Mean values of the power at the output relative to the unperturbed values for (a) $QC = 0$, (b) $QC = 0.15$, (c) $QC = 0.25$, and (d) $QC = 0.35$ for the synchronous velocity case, $b_0 = 0$.The points are the results of numerically integrating Eq. (2.8). The solid and dashed lines show the perturbation and Riccati formulas, Eqs. (2.13) and (2.14), respectively. Here, $x = 100, C = 0.05, \Delta = 1$, and $d = 0$.

Figures 2.11 and 2.12 show how the gain and phase are affected by the inclusion of the QC term, increasing it from 0 to 0.35 for the synchronous case, $b_0 = 0$. When $QC \neq 0$, both the perturbation and Riccati methods predict a larger variation in gain and phase than shown by the numerical analysis. The Riccati method tends to predict smaller variations than the perturbation method, but neither prediction shows agreement with the numerical data. Figures 2.13 and 2.14 show the gain and phase variations for QC again increasing from 0 to 0.35, this time for the $b_0 = 1$ case.

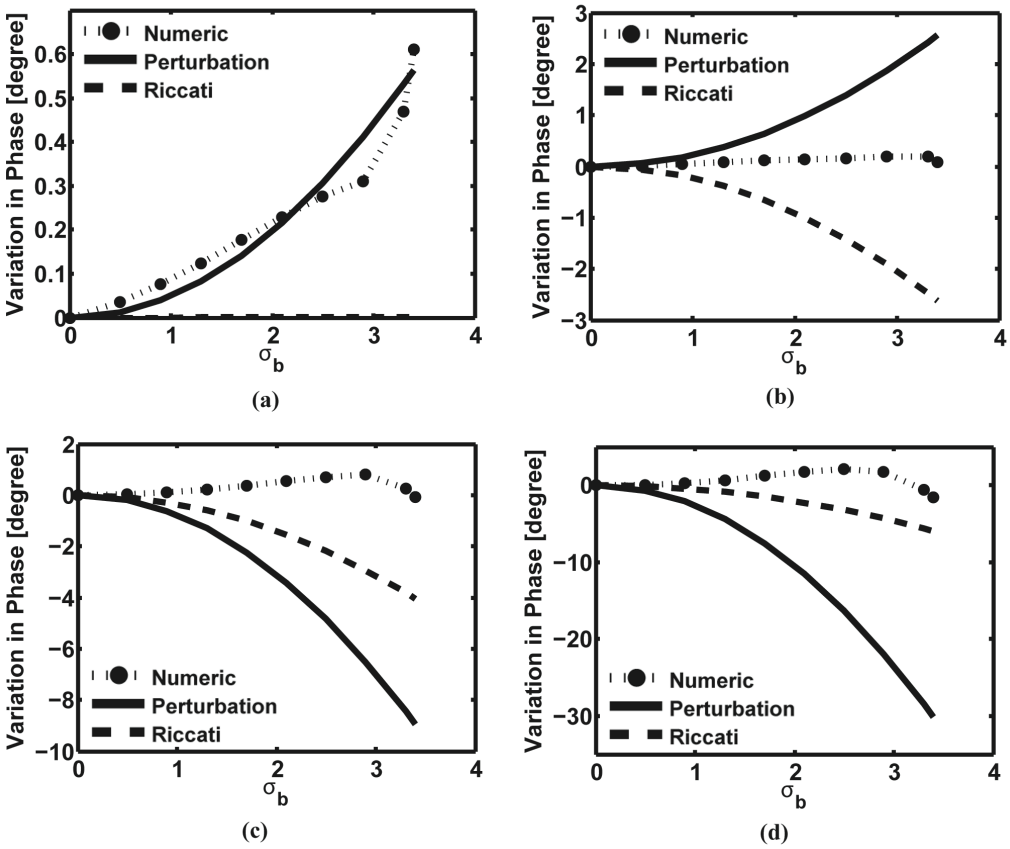

Figure 2.12: Mean values of the phase at the output relative to the unperturbed values for (a) $QC = 0$, (b) $QC = 0.15$, (c) $QC = 0.25$, and (d) $QC = 0.35$ for the synchronous velocity case, $b_0 = 0$.The points are the results of numerically integrating Eq. (2.8). The solid and dashed lines show the perturbation and Riccati formulas, Eqs. (2.13) and (2.14), respectively. Here, $x = 100, C = 0.05, \Delta = 1$, and $d = 0$.

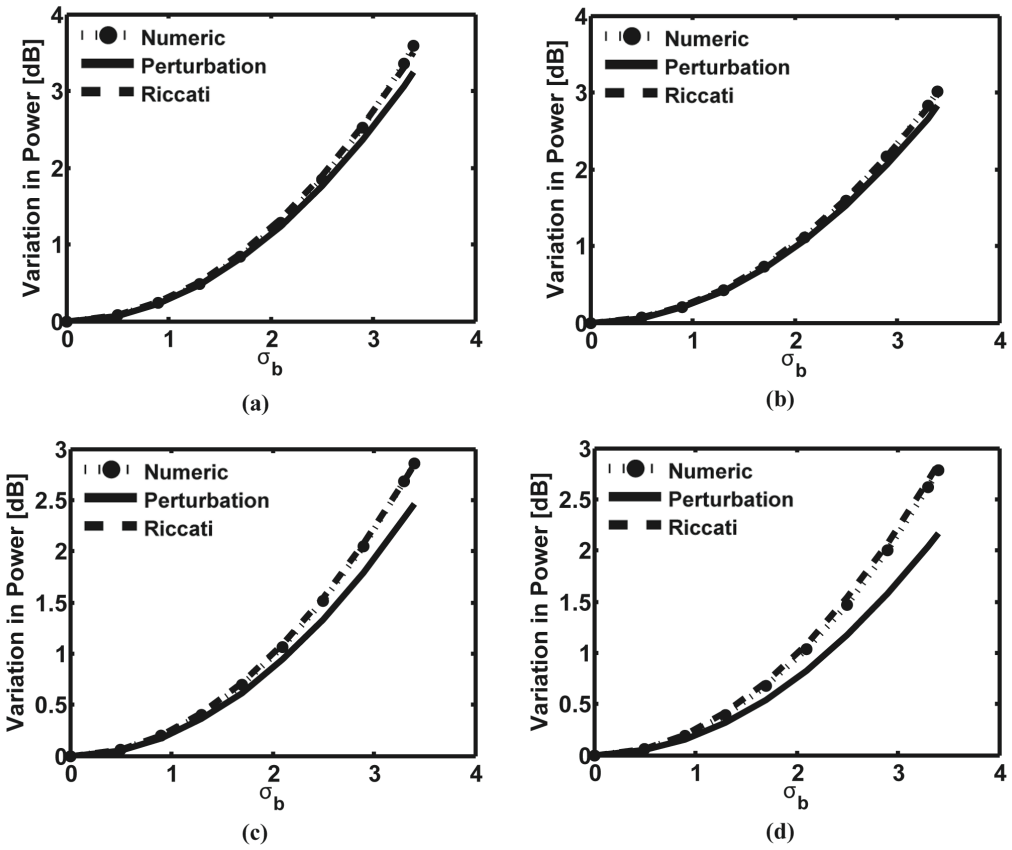

Figure 2.13: Mean values of the power at the output relative to the unperturbed values for (a) $QC = 0$, (b) $QC = 0.15$, (c) $QC = 0.25$, and (d) $QC = 0.35$ for the non-synchronous velocity case, $b_0 = 1$.The points are the results of numerically integrating Eq. (2.8). The solid and dashed lines show the perturbation and Riccati formulas, Eqs. (2.13) and (2.14), respectively. Here, $x = 100, C = 0.05, \Delta = 1$, and $d = 0$.

In this case, the Riccati method shows good agreement with the numerical data for gain. Neither analytical method shows agreement with the numerical phase data in this case. The $b_0 = -1$ case could not be calculated reliably because the TWT would not amplify for any significant values of QC.

One explanation of the disagreement among the perturbation, Riccati, and numeric results could stem from the fact that the presence of the space charge term reduces the range over b in which there will be gain. Figure 2.15 shows the real and imaginary parts of the propagation constant, δ, as a function of b over several dif-

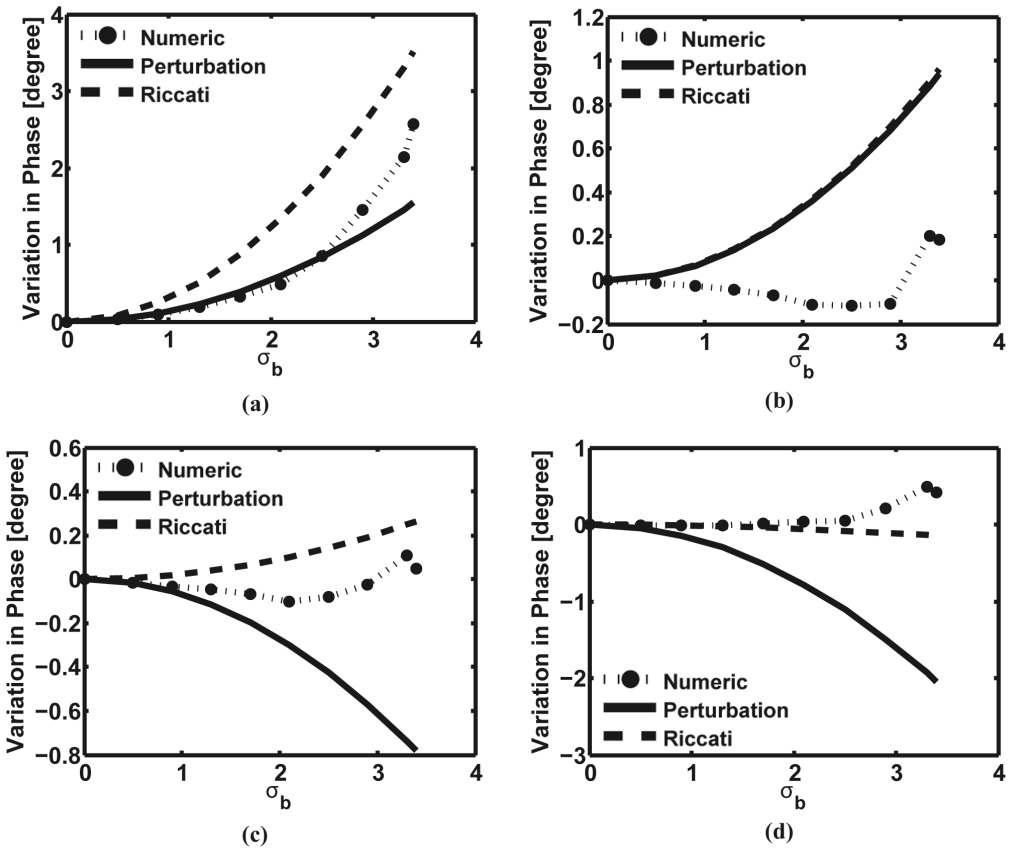

Figure 2.14: Mean values of the phase at the output relative to the unperturbed values for (a) $QC = 0$, (b) $QC = 0.15$, (c) $QC = 0.25$, and (d) $QC = 0.35$ for the non-synchronous velocity case, $b_0 = 1$.The points are the results of numerically integrating Eq. (2.8). The solid and dashed lines show the perturbation and Riccati formulas, Eqs. (2.13) and (2.14), respectively. Here, $x = 100, C = 0.05, \Delta = 1$, and $d = 0$.

ferent values of QC. As Fig. 2.15 shows, increasing QC shrinks the region of b, and also shifts the region of b, over which gain occurs as well as reduces the magnitude of x, when compared with Fig. 2.5. As less amplification occurs, the amplitude of the growing wave can become comparable to those of the other two forward propagating waves. This violates the initial assumption of a single dominant growing wave in the Riccati analysis.

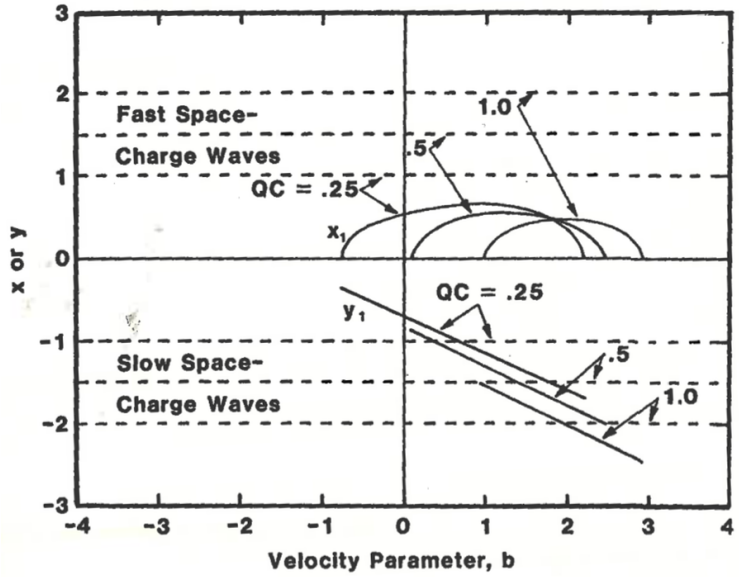

Figure 2.15: The effect of the space charge term, QC, on the propagation constant of the dominant, exponentially growing mode with no losses. The dashed lines represent the fast and slow space charge waves that can be excited in the beam for the corresponding values of QC, showing that it is the bunching associated with the slow space charge wave that produces amplification. Image from [1].

2.5.2 Standard Deviations in the Absence of the Space Charge Term ($QC = 0$)

Ignoring the AC space charge effects by setting QC = 0, we show in Figs. 2.16 - 2.18 the analytical standard deviation calculation from the perturbation method, Eqs. (2.11a) and (2.11b), and compare with the statistical standard deviation as calculated from the numerical integration of Eq. (2.8). Both calculations are in agree-

ment over a range of velocity mismatch parameters. (The standard deviation in the Riccati method has not been derived.) Figures 2.16, 2.17, and 2.18 show, respectively, the results of these calculations when the velocity mismatch parameter is fixed at a value of $b_0 = -1, 0$, and 1.

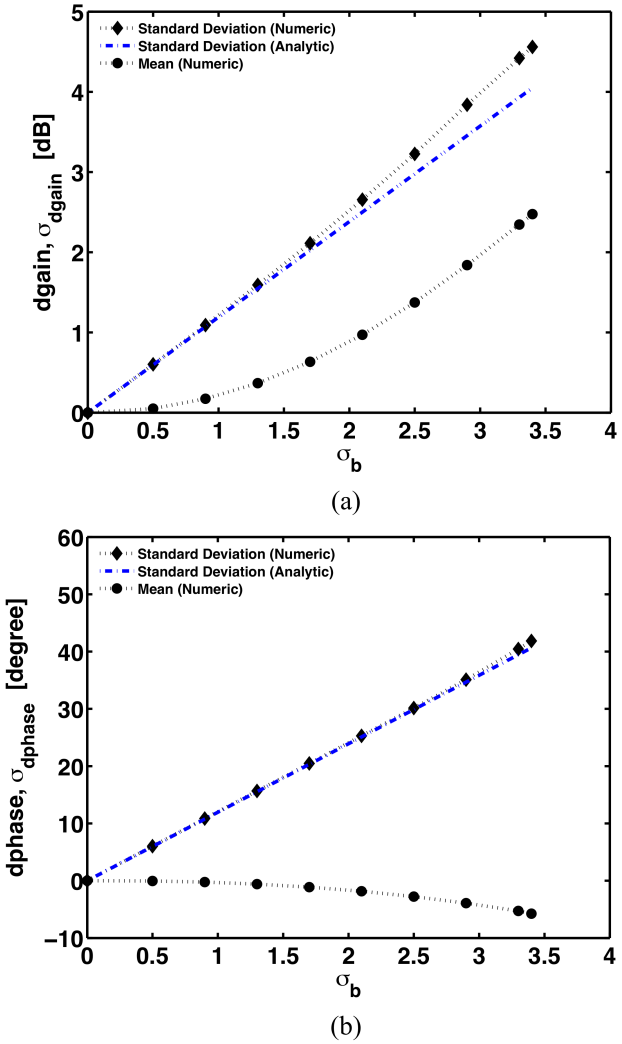

Figure 2.16: Mean values and standard deviation of the (a) gain and (b) phase at the output relative to the unperturbed values for $QC = 0$ for the non-synchronous velocity case, $b_0 = -1$. The circles are the results of numerically integrating Eq. (2.8). The diamonds are the standard deviation results from numerically integrating Eq. (2.8). The dashed line is the analytic standard deviation as calculated from Eqs. (2.11a) and (2.11b). Here, $x = 100, C = 0.05, \Delta = 1$, and $d = 0$.

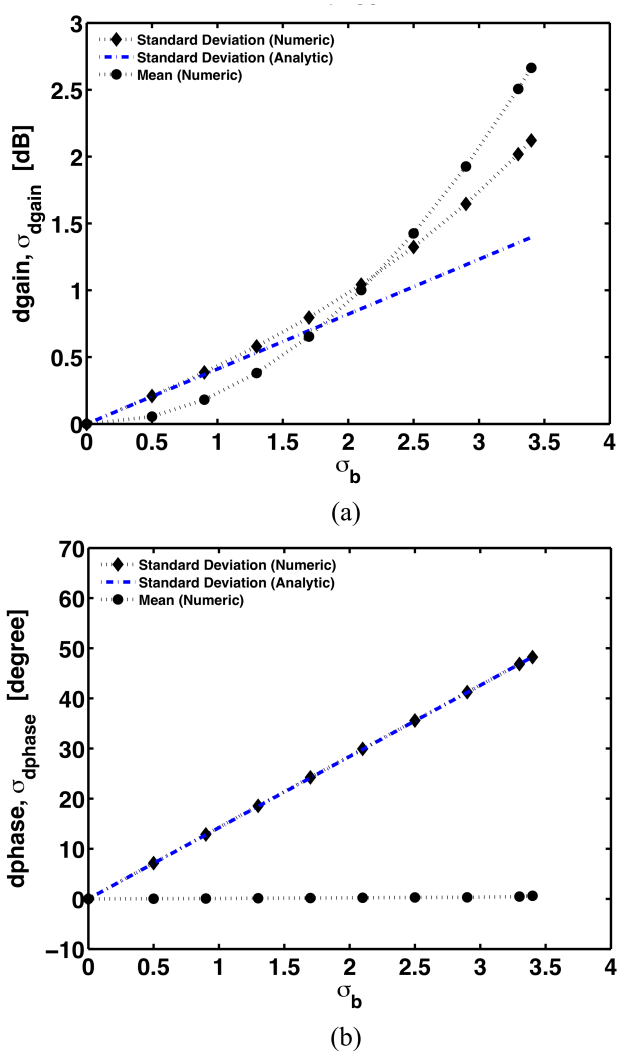

Figure 2.17: Mean values and standard deviation of the (a) gain and (b) phase at the output relative to the unperturbed values for $QC = 0$ for the non-synchronous velocity case, $b_0 = 0$. The circles are the results of numerically integrating Eq. (2.8). The diamonds are the standard deviation results from numerically integrating Eq. (2.8). The dashed line is the analytic standard deviation as calculated from Eqs. (2.11a) and (2.11b). Here, $x = 100, C = 0.05, \Delta = 1$, and $d = 0$.

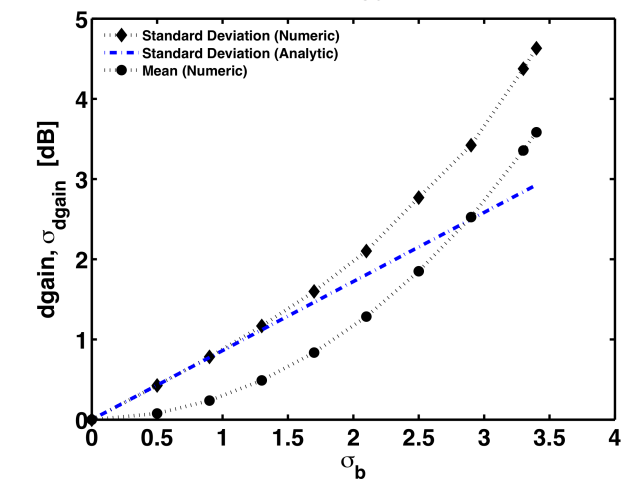

(a)

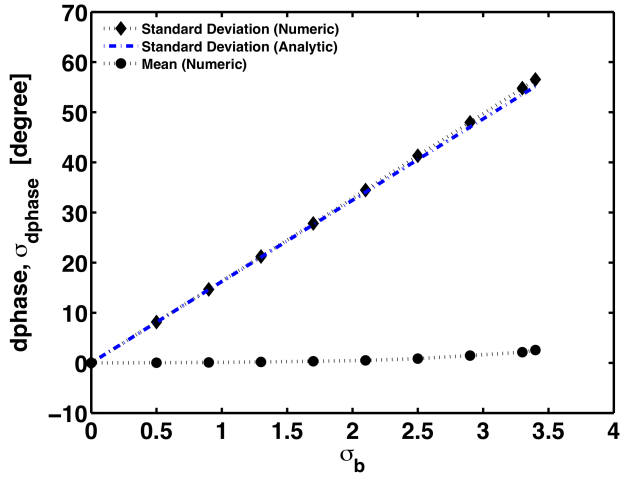

(b)

Figure 2.18: Mean values and standard deviation of the (a) gain and (b) phase at the output relative to the unperturbed values for $QC = 0$ for the non-synchronous velocity case, $b_0 = 1$. The circles are the results of numerically integrating Eq. (2.8). The diamonds are the standard deviation results from numerically integrating Eq. (2.8). The dashed line is the analytic standard deviation as calculated from Eqs. (2.11a) and (2.11b). Here, $x = 100, C = 0.05, \Delta = 1$, and $d = 0$.

2.5.3 Standard Deviations in the Presence of the Space Charge Term ($QC \neq 0$)

Figures 2.19 - 2.22 show the analytical standard deviation as calculated by Eqs. (2.11a) and (2.11b) with the space charge modified expression for g_b from Eq. (2.12), as well as the statistical standard deviation calculation from the numerical method. In Fig. 2.19 we show the gain and in Fig. 2.20 we show the phase for a synchronous case ($b_0 = 0$) in the presence of space charge effects. In Fig. 2.21 we show the gain and in Fig. 2.22 we show the phase for a nonsynchronous case ($b_0 = 1$) in the presence of space charge effects. With the inclusion of the space charge term, QC, Eqs. (2.11a) and (2.11b) are no longer in agreement with the statistical calculation. The difference between the two increases with increasing values of QC. As was the case for the mean variation (Section 2.5.1), the QC term reduces the gain in the TWT because it represents the space charge force that debunches the beam. In such a case, all three waves can have comparable amplitudes. The $b_0 = -1$ case could not be calculated reliably because the TWT would not amplify for any significant values of QC.

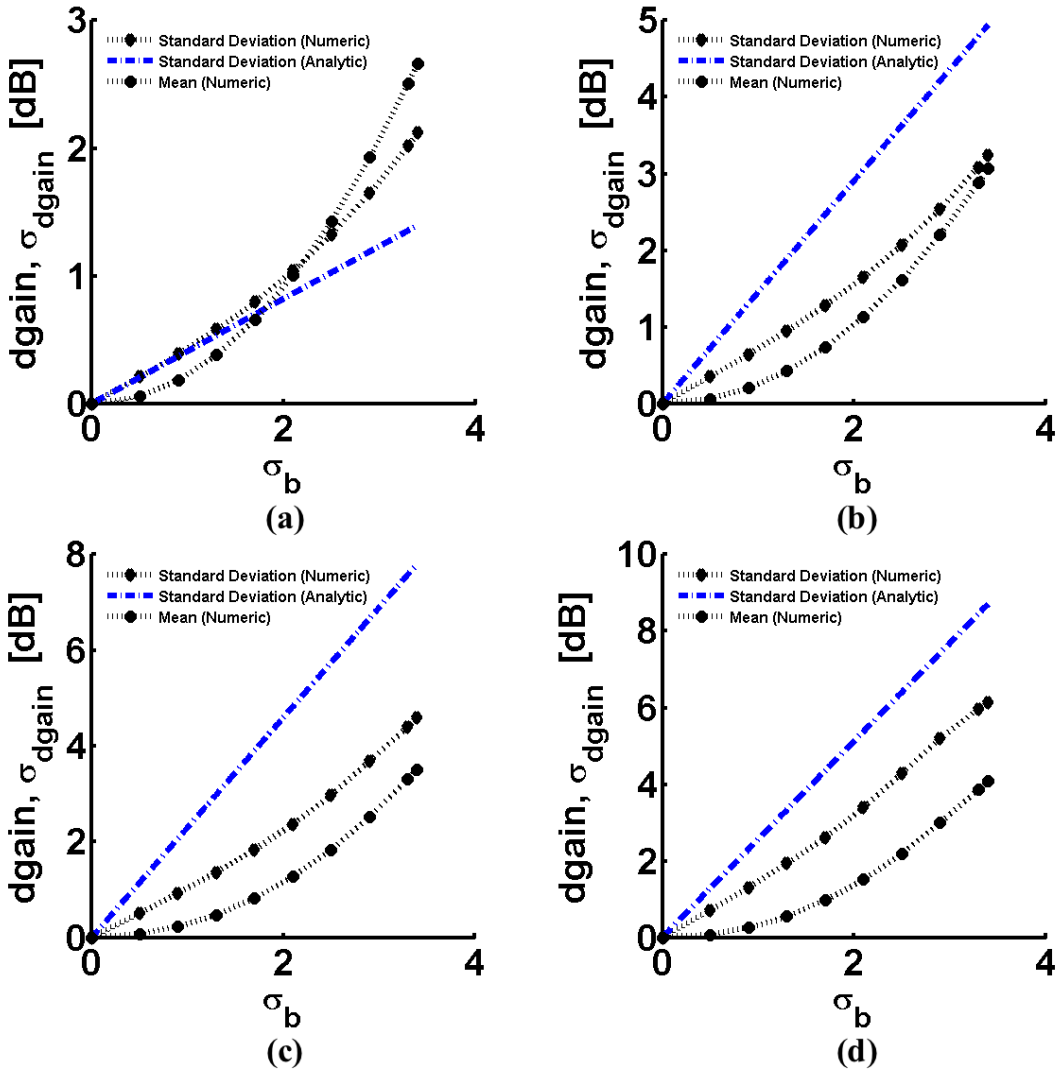

Figure 2.19: Mean values and standard deviation of the gain at the output relative to the unperturbed values for (a) $QC = 0$, (b) $QC = 0.15$, (c) $QC = 0.25$, and (d) $QC = 0.35$ for the synchronous velocity case, $b_0 = 0$. The circles are the results of numerically integrating Eq. (2.8). The diamonds are the standard deviation results from numerically integrating Eq. (2.8). The dashed line is the analytic standard deviation as calculated from Eqs. (2.11a) and (2.11b). Here, $x = 100, C = 0.05, \Delta = 1$, and $d = 0$.

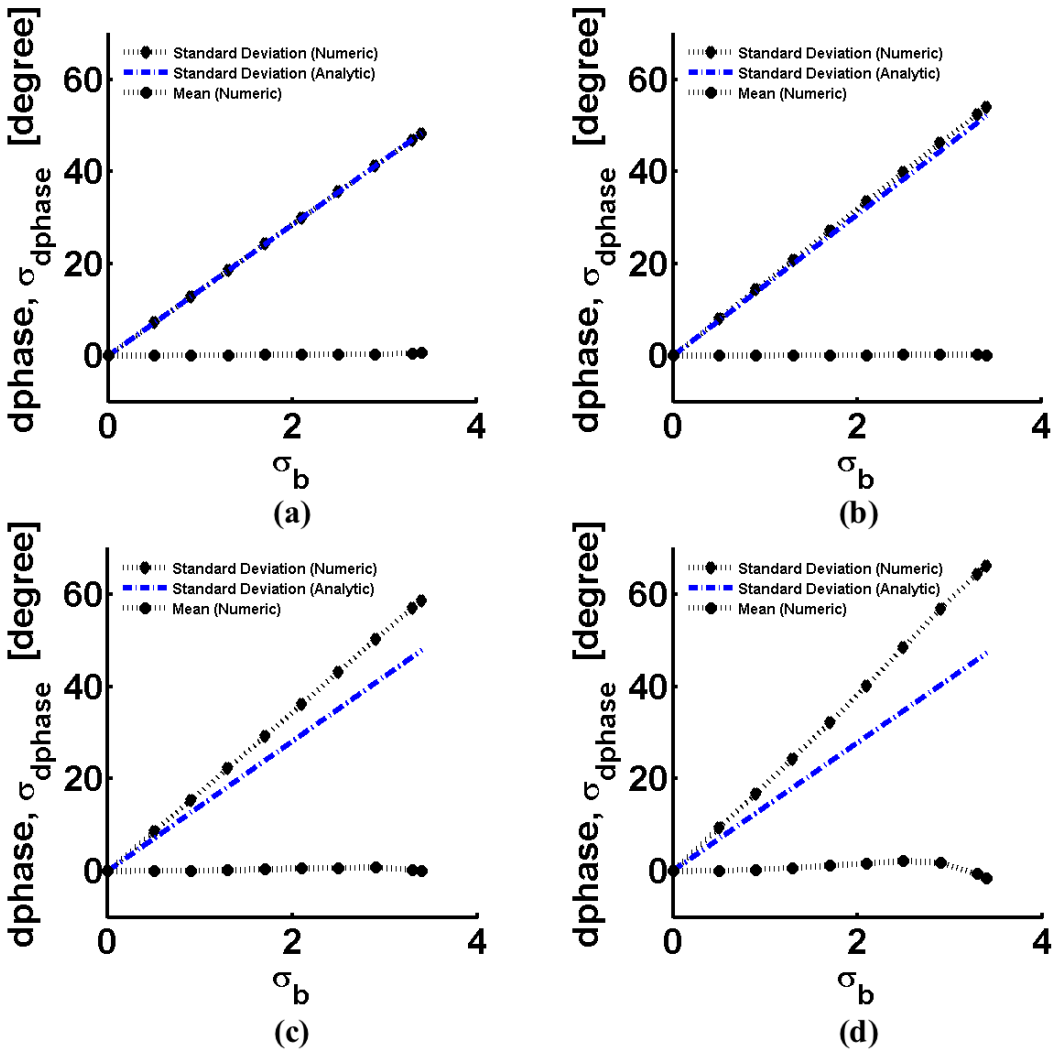

Figure 2.20: Mean values and standard deviation of the phase at the output relative to the unperturbed values for (a) $QC = 0$, (b) $QC = 0.15$, (c) $QC = 0.25$, and (d) $QC = 0.35$ for the synchronous velocity case, $b_0 = 0$. The circles are the results of numerically integrating Eq. (2.8). The diamonds are the standard deviation results from numerically integrating Eq. (2.8). The dashed line is the analytic standard deviation as calculated from Eqs. (2.11a) and (2.11b). Here, $x = 100, C = 0.05, \Delta = 1$, and $d = 0$.

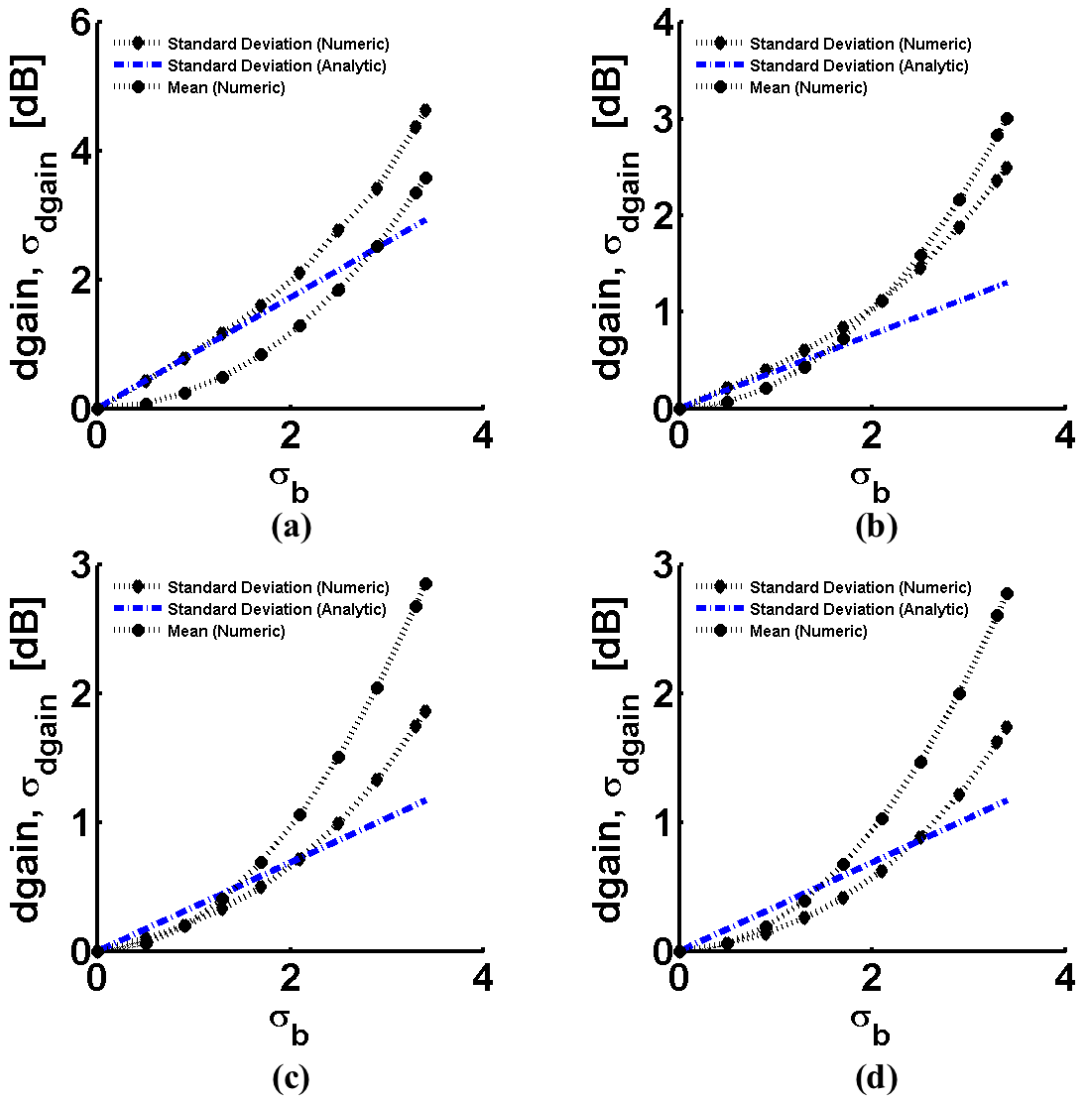

Figure 2.21: Mean values and standard deviation of the gain at the output relative to the unperturbed values for (a) $QC = 0$, (b) $QC = 0.15$, (c) $QC = 0.25$, and (d) $QC = 0.35$ for the non-synchronous velocity case, $b_0 = 1$. The circles are the results of numerically integrating Eq. (2.8). The diamonds are the standard deviation results from numerically integrating Eq. (2.8). The dashed line is the analytic standard deviation as calculated from Eqs. (2.11a) and (2.11b). Here, $x = 100, C = 0.05, \Delta = 1$, and $d = 0$.

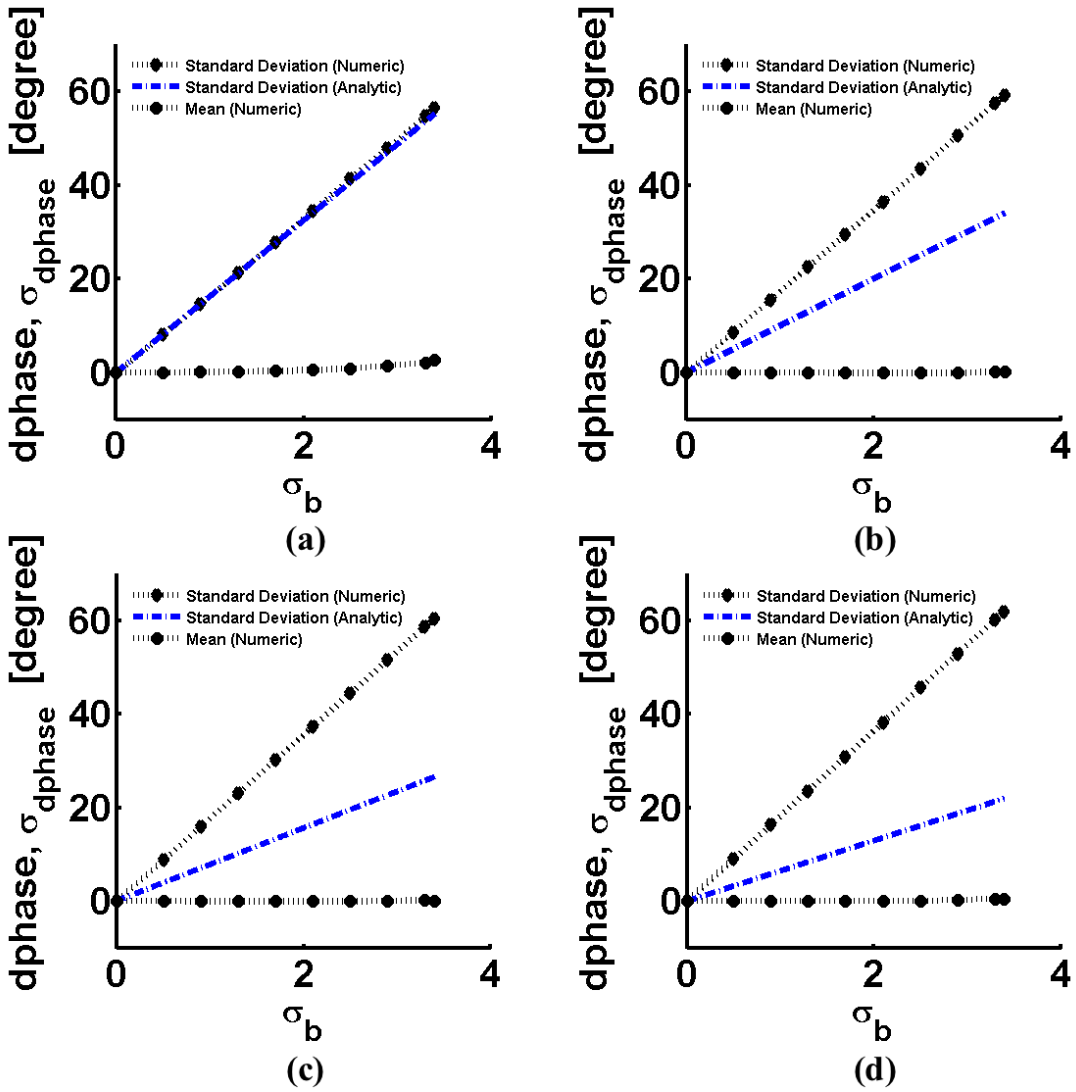

Figure 2.22: Mean values and standard deviation of the phase at the output relative to the unperturbed values for (a) $QC = 0$, (b) $QC = 0.15$, (c) $QC = 0.25$, and (d) $QC = 0.35$ for the non-synchronous velocity case, $b_0 = 1$. The circles are the results of numerically integrating Eq. (2.8). The diamonds are the standard deviation results from numerically integrating Eq. (2.8). The dashed line is the analytic standard deviation as calculated from Eqs. (2.11a) and (2.11b). Here, $x = 100, C = 0.05, \Delta = 1$, and $d = 0$.

2.5.4 Evaluation of a G-Band Folded Waveguide Traveling Wave Tube

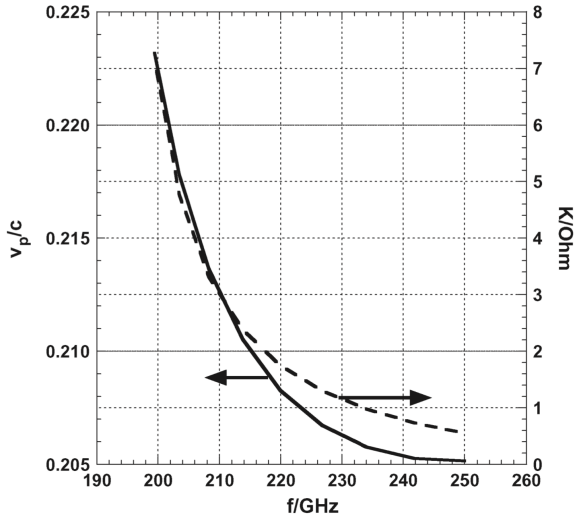

Figure 2.23: Phase velocity for the error-free pitch and interaction impedance as a function of frequency for a G-Band TWT. Figure from [37].

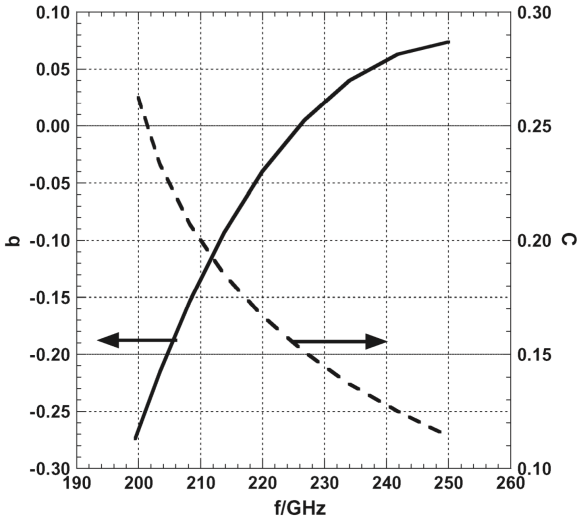

Figure 2.24: Pierce's velocity parameter and gain parameter as a function of frequency for a G-Band TWT. Figure from [37].

Finally, as a concrete example, we consider the G-band (210 GHz) folded waveguide TWT recently studied by Chernin et al. [37], with a beam voltage of $V_b = 11.7$ kV, a beam current of $I_b = 120$ mA, a length of 1.2 cm, and an average circuit pitch of 0.02 cm. The interaction impedance, K, and C^3 are related by $C^3 \equiv KI_b/(4V_b)$

(Eq. (2.3)). These parameters correspond to a normalized length of $x = 240$, and we take a correlation length of $\Delta = 4$. For this example we assume $QC = 0$ and consider the specific case using Figs. 2.23 and 2.24 to calculate $C = 0.0197$ and $b_0 = 0.36$ [37]. Figure 2.25 shows both the gain and phase variation of this G-Band-like TWT accurately predicted by both the perturbation and Riccati methods. The statistical standard deviations in gain and phase and their analytic formula are also presented in Fig. 2.25, showing good agreement also.

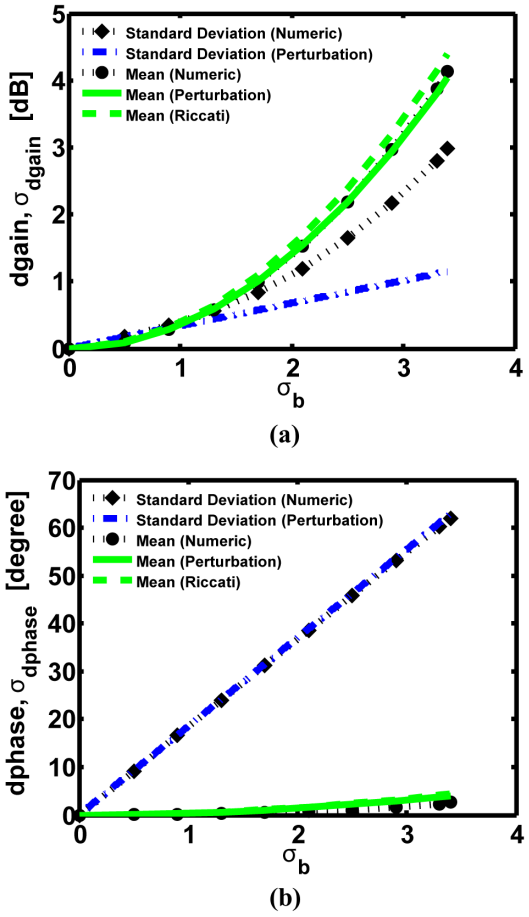

Figure 2.25: Mean values and standard deviation of the (a) gain and (b) phase at the output relative to the unperturbed values for a G-Band-like TWT. Results from the statistical, perturbation, and Riccati calculations for mean as well as analytic and statistical results for standard deviation are plotted. Here, $x = 240, \Delta = 4, C = 0.0197, b_0 = 0.36$, and $QC = d = 0$.

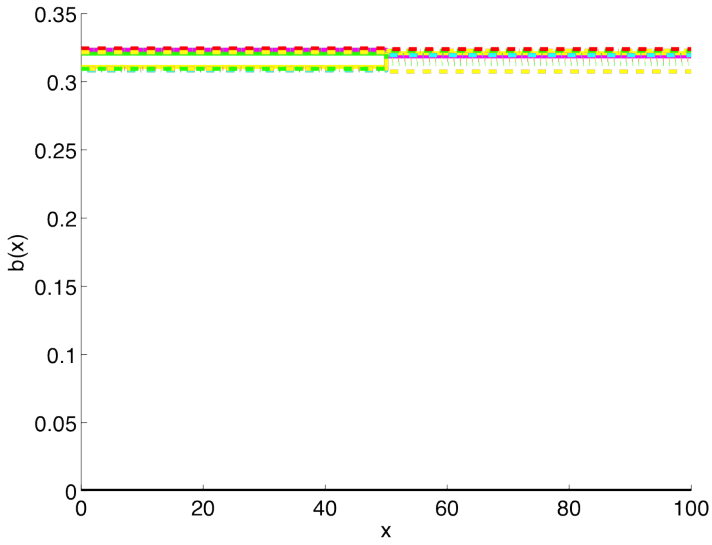

Figure 2.26: The twenty velocity parameter profiles for a TWT with 2 segments that produce the highest gain. Here, $x = 100, C = 0.05, b_0 = 0$, $\sigma_b = 1.7$ and $QC = d = 0$.

2.6 Optimization of Velocity Parameter Profile

The results in Section 2.5 have shown how it is possible to *statistically* achieve simulated TWTs that exhibit higher gain in the presence of random errors. This result would suggest that the profile of the velocity parameter might not be optimized for a given TWT. This leads us to consider the optimization of the velocity parameter, $b(x)$, profile. Here, we examine the types of b-profiles that yield the highest gain. To increase (decrease) b in a helix TWT, the pitch (period) of the helix is decreased (increased). The nature of this problem lends itself easily to parallel computing, so the forward integration code was parallelized and used to compute the optimal $b(x)$ profile by simulating 10^6 samples, where the value of b in each segment was sampled randomly, and observing the profiles that result in the highest gain. This approach was used to optimize TWTs for various evenly spaced segments, N. The number of segments from $N = 2$ to $N = 100$ were considered.

We find that in the case of two segments ($N = 2$) the twenty velocity profiles that yield the highest gain appear to be some constant value across the length of the

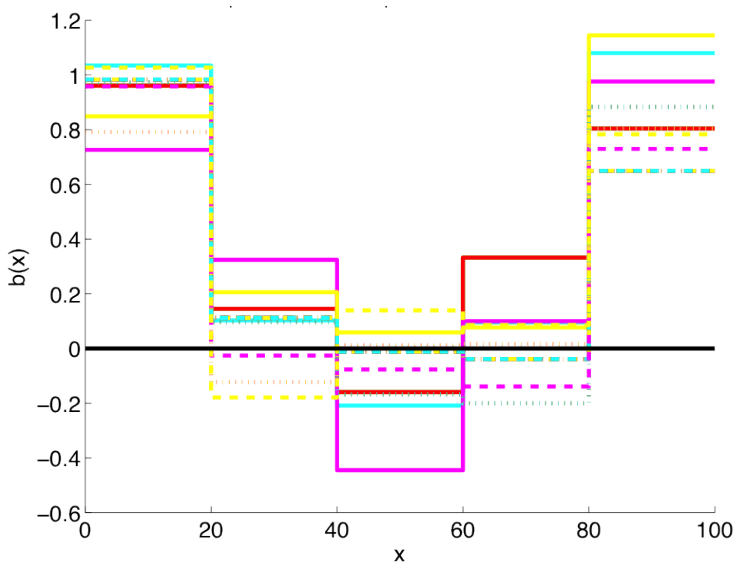

Figure 2.27: The twenty velocity parameter profiles for a TWT with 5 segments that produce the highest gain (811 units vs 647 units of power gain for an error-free tube as in Fig. 1.6). Here, $x = 100, C = 0.05, b_0 = 0$, $\sigma_b = 1.7$ and $QC = d = 0$.

TWT, as shown in Fig. 2.26. For this two segment case that value is around $b = 0.32$. This result is reasonable because this optimum value of b gives the peak gain of a pristine TWT, i.e., $b = 0.314$, as shown in Fig. 2.8. When the number of segments is increased from 2, however, a peculiar feature arises in the velocity parameter profile. It is seen that there is a parabolic shape to the velocity profile with a drop in value of b in the middle section of the TWT along the axis. This can be seen for a case with five segments ($N = 5$) in Fig. 2.27. This feature exists for three segments all the way up to 20 segments (see Fig. 2.28), although the features become obscure to the point of unrecognizable as the number of segments is increased beyond $N = 20$. The resulting optimized $b(x)$ profile for 100 segments can be seen in Fig. 2.29. It is possible that this obscuring is due to the fact that 10^6 samples is not enough as the number of segments increases.

The $b(x)$ profile in Fig. 2.27 means that $v_b > v_p$ near the input end ($x \simeq 0$) and output end ($x \simeq 100$), while $v_b < v_p$ in the central region of the circuit ($x \simeq 50$).

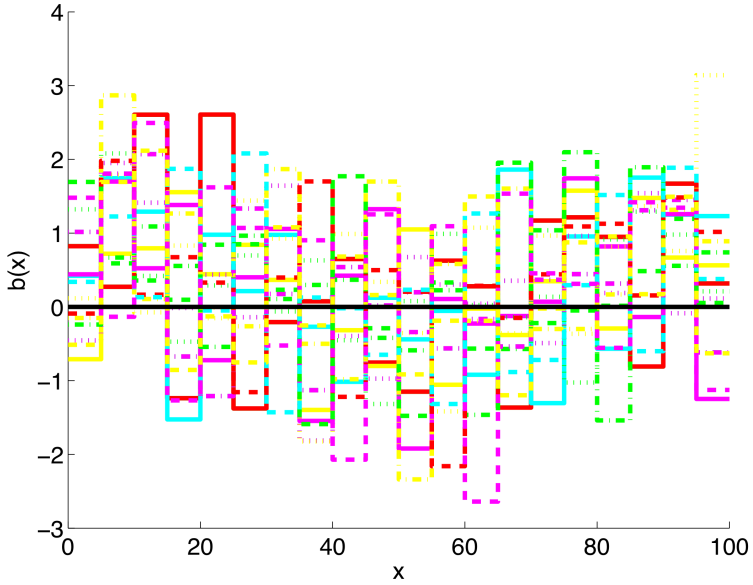

Figure 2.28: The twenty velocity parameter profiles for a TWT with 20 segments that produce the highest gain. Here, $x = 100, C = 0.05, b_0 = 0$, $\sigma_b = 1.7$ and $QC = d = 0$.

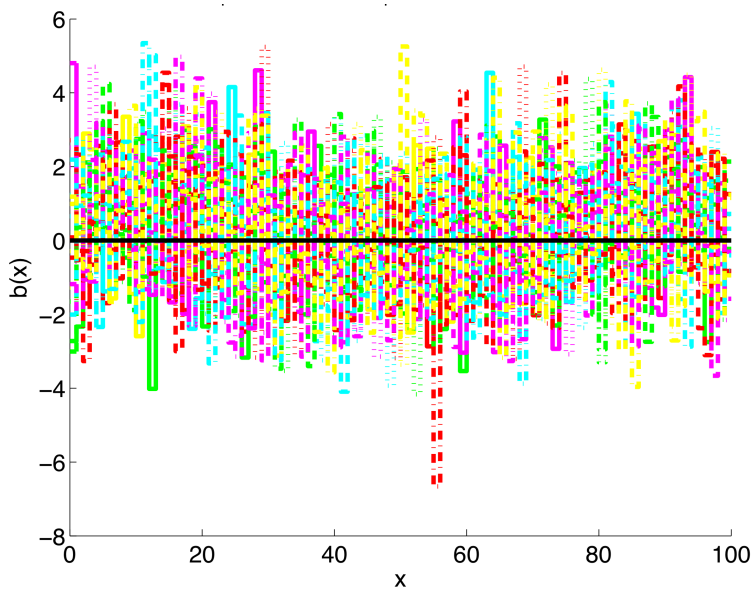

Figure 2.29: The twenty velocity parameter profiles for a TWT with 100 segments that produce the highest gain. Here, $x = 100, C = 0.05, b_0 = 0$, $\sigma_b = 1.7$ and $QC = d = 0$.

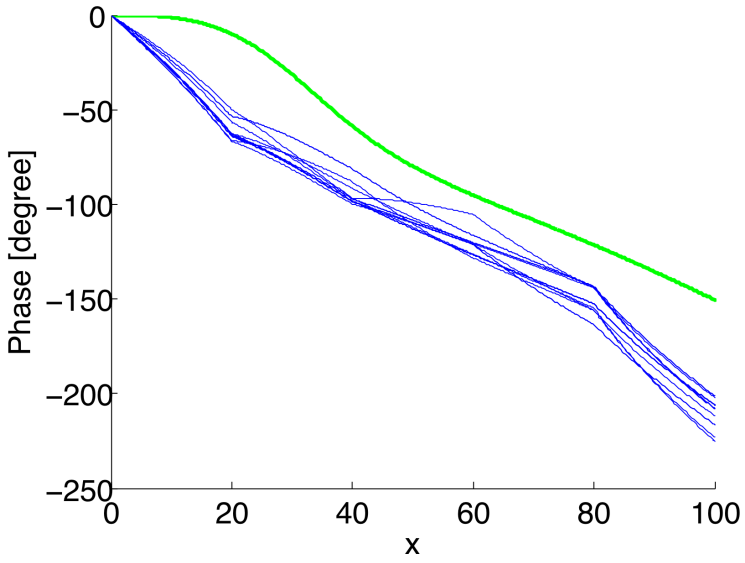

Figure 2.30: The phase as a function of TWT length, x. The smooth, green curve is the phase for the single segment calculation where the velocity profile $b = 0$ is constant. The blue curves are the results of the calculations made using the top 20 highest gain producing profiles for $N = 5$ segments, as shown in Fig. 2.27.

This can achieved physically by making the helix more tightly wound near the input and output ends, and loosely wound in the central region of the circuit. The phase for these 20 profiles are shown in Fig. 2.30. While the difference between these 20 circuits and the single segment case is 66° at the output, the standard deviation in the phase at the output among these 20 samples is only 6.6°. Furthermore, note that the phase velocity of the helix slow wave structure is insensitive to frequency. The optimal $b(x)$ profile for one frequency, therefore, would also be the optimal $b(x)$ profile for all frequencies on the helix, to the lowest order. The possible existence of an optimal $b(x)$ profile, together with its frequency dependence, remains to be studied in the future.

2.7 Summary and Conclusions

Two different formulas were derived to predict the deviations in gain and phase in a traveling wave tube in the presence of errors randomly distributed along the

axis: a second-order perturbation analysis that accounts for all three forward propagating waves and a Riccati analysis that includes only the amplifying wave. We have compared both of these models against a numerical integration of the governing, third-order linear differential equation for cases with nonzero b and the inclusion of AC space charge effects. We have found that the perturbation analytic model shows good agreement with the numerical analysis for non-synchronous beam velocities, i.e., nonzero b, in the absence of space charge effects ($QC = 0$). We have also found that the analytic models do not accurately predict the TWT behavior in the presence of AC space charge effects ($QC \neq 0$). A possible explanation is that a nonzero QC would enlarge the range of b in which the amplifying wave would have a reduced or even zero gain, in which case all three waves would have comparable amplitudes.

Since we have shown that the standard deviation is much larger than the deviation in the mean from an error-free tube, we have essentially solved the puzzle as to why random variations in $b(x)$, presumably caused by manufacturing errors, could lead to a higher gain in a significant fraction of the samples simulated, as shown in Fig. 1.6. Identification of the types of random errors that would lead to higher gain awaits further study, while some preliminary assessment has been made.

CHAPTER 3

Effects of the Reflected Wave in a Traveling Wave Tube and a Consideration of the Absolute Instability

3.1 Introduction

In the previous chapter, the effects of random errors in a traveling wave tube were considered in the absence of the backward wave. The backward wave, however, can play a significant role on the performance of the traveling wave tube [67–69]. In the presence of the backward wave, reflections due to a mismatch at the output can cause a gain ripple across the operation band which is characteristic of regenerative oscillation. The helix TWT is particularly susceptible to interaction with the backward wave due to the relatively linear dispersion characteristics of the circuit [67]. In the presence of random errors in the circuit of the TWT, there are many sources for the backward wave to arise [37]. In this chapter, we discuss the effects of the backward wave in the presence of internal reflections due to random circuit fabrication errors on the slow wave circuit of the TWT.

An instability is required for gain in any amplifier. In the case of stable gain in a TWT, this instability is known as convective instability, meaning that the signal amplifies as it co-propagates with the beam [70]. The absolute instability exists if the

gain (beam current) is so high that the reverse propagating mode of the circuit can be excited internally, so that oscillation occurs even in a perfectly matched TWT [71, 72]. The absolute instability leads to oscillations in a traveling wave tube that can spread to all locations in the system. Briggs [71] and Bers [72] devised a criterion, known as the Briggs-Bers criterion, that distinguishes absolute and convective instability from the dispersion relation. The latter part of this chapter investigates the threshold of the absolute instability in the traveling wave tube model using a dielectric waveguide for which the exact dispersion relation is analyzed by the Briggs-Bers criterion, as described in Section 3.6. The Briggs-Bers criterion distinguishes an amplifying wave from an absolute instability [71, 72].

3.2 Effects of Multiple Internal Reflections Due to Random Manufacturing Errors

In Chapter 2, we discuss the effects of small random variations in the circuit properties of a TWT in the absence of the backward wave. To analyze the effects of backward waves, the effects of loss and "AC space charge" effects are neglected here, e.g., $d = 0$ and $QC = 0$. With the inclusion of the backward wave, Eq. (2.1b) remains the same and reads, in the absence of space charge effects ($QC = 0, \beta_q = 0$),

$$\left(\frac{\partial}{\partial z} + j\beta_e\right)^2 s = a, \tag{3.1}$$

where s is the displacement of an electron fluid element from its unperturbed position, a represents the circuit field, and $\beta_e = \omega/v_0$ is the propagation constant which characterizes the beam's DC velocity v_0.

To include the reverse propagating mode on the circuit, operate Eq. (2.2) by $(\partial/\partial z - j\beta_p)$ and approximate this operation by multiplying $-2j\beta_p$ to the RHS to obtain

$$\left(\frac{\partial^2}{\partial z^2} + \beta_p^2\right) a = -2\beta_p \beta_e^3 C^3 s \tag{3.2}$$

where $\beta_p = \omega/v_p$ is the cold circuit wavenumber, v_p is the cold circuit phase velocity, that is the phase velocity of the wave on the circuit in the absence of the electron beam, and C is the Pierce gain parameter (Eq. (2.3)). Equation (3.2) is exactly Eq. (2) of Chernin et al. [37], although a different normalization of the axial electric field is used. The two can be related by the expression $a = \beta_e^2 E$. Note also that Eq. (3.2) is the same as Eq. (14) on p. 150 of Chodorow and Susskind [73]. In the absence of the beam ($C = 0$), Eq. (3.2) gives two cold tube solutions of a, $e^{-j\beta_p z}$ and $e^{+j\beta_p z}$, that travel with phase velocity v_p in the $\pm z$ directions. Following the notation in Section 2.4, we define $x = \beta_e z$ as the normalized axial distance and $f(x) = e^{jx} s(x)$ is the solution to the fourth-order ordinary differential equation

$$\frac{\partial^4 f(x)}{\partial x^4} - 2j\frac{\partial^3 f(x)}{\partial x^3} + bC(2 + bC)\frac{\partial^2 f(x)}{\partial x^2} + 2C^3(1 + bC)f = 0. \tag{3.3}$$

Equation (3.3) is derived from combining Eqs. (3.1) and (3.2) in the same manner as the formulation of Eq. (2.8). It is a fourth order ordinary differential equation because of the inclusion of the reverse propagating circuit wave. The Pierce parameters b and C in Eq. (3.3) may be functions of axial distance, x, as a result of manufacturing errors on the circuit.

Similar to the analysis of Chapter 2, we divide the interaction space of the TWT into N equal length sections. Within each section, we assume b and C to be constants. The general solution to Eq. (3.3), if x_i denotes the right-hand side of the ith section, may be written as [37]

$$f^{(i)}(x) = \sum_{k=1}^{4} f_k^{(i)} e^{\lambda_k^{(i)} x}, \tag{3.4}$$

where $\lambda_k^{(i)}$ are the four roots of the dispersion relation, which reads (cf. Eq. (3.3)),

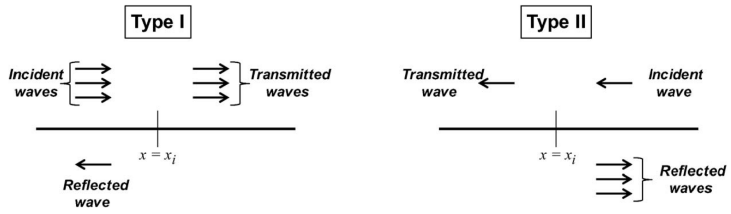

Figure 3.1: Depiction of the two types of reflections that can occur at the interface of two sections within the model of [37]. Image from [37].

$$D(\lambda) \equiv \lambda^4 - 2j\lambda^3 + b^{(i)}C^{(i)}\left(2 + b^{(i)}C^{(i)}\right)\lambda^2 + 2C^{(i)3}\left(1 + b^{(i)}C^{(i)}\right) = 0. \tag{3.5}$$

Here, $\lambda = C\delta = -j(\beta - \beta_e)/\beta_e$ is the root to the fourth degree polynomial (3.5) in each section (cf. Eq. (2.7) for the three-wave formulation), and $b^{(i)}$ and $C^{(i)}$ are the Pierce parameters in section i, which remain constant over the entirety of that section. In Eq. (3.4), $k = 1, 2, 3, 4$ represents the kth mode, where modes $k = 1, 2, 3$ are the three forward propagating modes and mode $k = 4$ is the reverse propagating mode. We can readily see by dropping the fourth order term from Eq. (3.5) that we can recover the three wave dispersion relation, Eq. (2.7), by writing $\lambda = C\delta$, $\delta = -j(\beta - \beta_e)/(C\beta_e)$, β being the propagation constant, and by assuming that $bC \ll 1$.

Chernin analyzed two types of reflections [37], shown in Fig. 3.1. The first type (referred to as 'Type I') results from three forward propagating waves in section i approaching a discontinuity in b due to random errors, causing a reflected wave in section i and three forward propagating waves in the next section, section $(i + 1)$. The second type (referred to as 'Type II') results from a reverse propagating wave in section $(i+1)$ encountering a discontinuity in b at the interface, causing three forward propagating waves in section $(i + 1)$ and a reverse propagating wave in section i. Chernin [37] provided a complete solution, which is outlined below.

We require initial four conditions to solve Eq. (3.3). However, only three are given

at the input, $x = 0$, and the fourth one is at the output, $x = x_N$. Similar to the three wave model in Section 2.4, we assume that the beam enters the interaction region with zero AC current, zero AC velocity, and unit input electric field. This results in three boundary conditions at $x = 0$ that read

$$f(0) = \sum_{k=1}^{4} f_k = 0, \tag{3.6a}$$

$$\frac{d}{dx} f(0) = \sum_{k=1}^{4} \lambda_k f_k = 0, \tag{3.6b}$$

and

$$\sum_{k=1}^{3} \lambda_k^2 f_k = 1. \tag{3.6c}$$

Equations (3.6) are exactly the same as the three boundary conditions (2.9) used in the analysis in Chapter 2. These boundary conditions make no mention of the backward wave. They do, however, imply that the backward wave does not originate at the input. The three forward propagating waves, however, do originate at the input (Eq. (3.6c)).

Finally, it is assumed that there is a perfect match at the output, i.e., no reflection at $x = x_N$. This is assumed to be true even in the presence of beam loading, the ability of the presence of a beam to alter the circuit characteristics. This allows the final boundary condition to be written as

$$f_4^{(N)} = 0. \tag{3.6d}$$

Due to the fact that the last boundary condition is at the output of the TWT, we can no longer integrate Eq. (3.3) forward from the input. Chernin solved the problem exactly using matrix algebra, however. See Chernin et al. [37] for the details of

Chernin's matrix algorithm. In Section 3.3 we report the validation of Chernin's solution from the data he obtained. In particular, his data yields $f(0), f'(0), f''(0)$, and $f'''(0)$ once the piecewise constant random function $b(x)$ is specified (Fig. 3.2). We then use these initial values to integrate Eq. (3.3) to compare with Chernin's solution for all x. This validation is reported next.

3.3 Validation of Backward Wave Matrix Calculation Algorithm

The numerical algorithm derived by Chernin yields the mode amplitudes in all sections, including the input section, of the TWT. The following cases show the validation of Chernin's matrix algorithm.

3.3.1 Validation Case 1

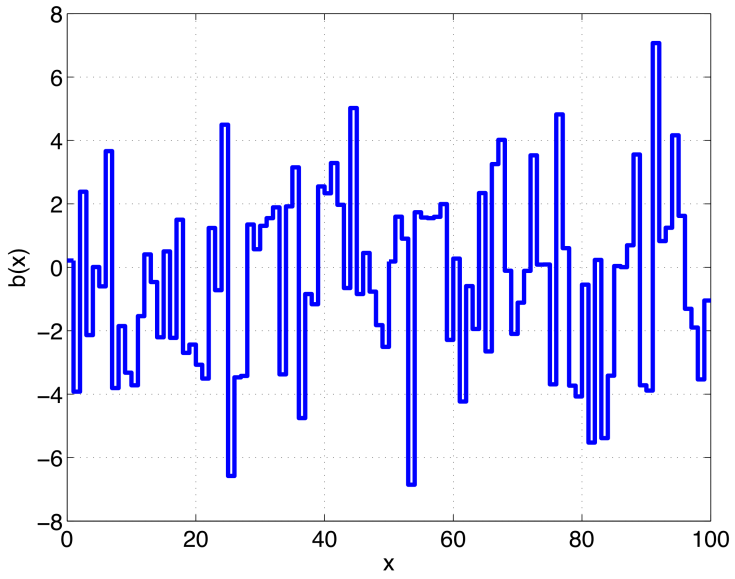

Figure 3.2: The profile for the Pierce velocity parameter, $b(x)$, for the first validation case.

For the first validation case, the standard parameters of $C = 0.05$, $d = 0$, $N = 100$, and TWT length of $x_N = 100$ were chosen. This is the base case of Pengvanich et al.

[32] and could correspond, for example, to a microwave power module TWT that has a 21.6 cm circuit length, a beam voltage of $V_b = 5$ kV, a beam current of $I_b = 260$ mA, and is operating at a frequency of 3 GHz [56]. The random profile for $b(x)$ for this simulated TWT example is shown in Fig. 3.2. Table 3.1 shows the results from the matrix calculation algorithm. Using the values for f and its derivatives at the input (Table 3.1), the forward integration code of Eq. (3.3) can be used to validate this method. The results of this calculation are found in Table 3.2. By comparing Tables 3.1 and 3.2, it is shown that the direct integration validates the matrix mode amplitude method out to at least 4 decimal places. Although a large amount of precision is shown, accuracy to so many places is not required. It was found, however, that round off error in the calculation of a single segment would be compounded when the number of error segments, N, was large. For example, with just 1% error in the calculation of the pristine TWT (a single segment), error in the calculation from the forward integration code for a TWT with $N = 100$ errors could be as large as 10%. Such errors are not present here.

Parameter	Value
$f(0)$	$-7.2724604117 \times 10^{-12} - j1.4447887331 \times 10^{-12}$
$f'(0)$	$1.9830784150 \times 10^{-13} - j8.2520226546 \times 10^{-14}$
$f''(0)$	$1.7838376836 - j1.5662689903$
$f'''(0)$	$3.1490879491 + j1.5653291201$
$f(x_N)$	$2.3822212200 \times 10^{3} - j9.6745552297 \times 10^{2}$
$f'(x_N)$	$1.0916583251 \times 10^{2} - j1.0351072389 \times 10^{2}$
$f''(x_N)$	$2.9764737113 - j4.9043443725$
$f'''(x_N)$	$1.3210160645 \times 10^{-1} - j1.2758698580 \times 10^{-1}$

Table 3.1: Mode amplitude values at the input and output of the TWT as calculated from Chernin's matrix algorithm [37].

Parameter	Value
$f(x_N)$	$2.3822210039 \times 10^{3} - j9.6745568468 \times 10^{2}$
$f'(x_N)$	$1.0916581938 \times 10^{2} - j1.0351072596 \times 10^{2}$
$f''(x_N)$	$2.9764727731 - j4.9043442418$
$f'''(x_N)$	$1.3210159568 \times 10^{-1} - j1.2758749225 \times 10^{-1}$

Table 3.2: Mode amplitude values at the output of the TWT as calculated from the direct integration of Eq. (3.3).

3.3.2 Validation Case 2

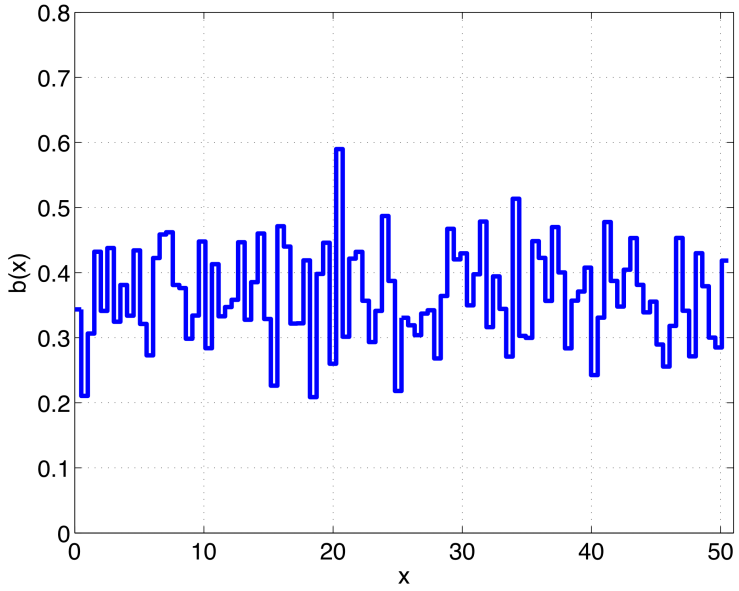

Figure 3.3: The profile for the pierce velocity parameter, $b(x)$, for the second validation case.

For the second validation case, the standard parameters of $d = 0$ and $N = 100$ are the same, but the values of the Pierce gain parameter and TWT length are different than those of the first validation case. Here, we take $C = 1.3744556891 \times 10^{-1}$ and $x_N = 5.0598638525 \times 10^{1}$. The random profile for $b(x)$ is shown in Fig. 3.3. Table 3.3 shows the results from the matrix calculation algorithm. Using the the values for f and its derivatives at the input (Table 3.3), the modified forward integration code can be used to validate this method. The results of this calculation are found in Table 3.4. By comparing Tables 3.3 and 3.4, it is shown that the direct integration validates the matrix mode amplitude method out to at least 7 decimal places. Again, the high level of precision shows that the effect of multiple error segments, N, is not increasing the error in the overall calculation.

Parameter	Value
$f(0)$	$2.2649937481 \times 10^{-12} + j3.2303049124 \times 10^{-12}$
$f'(0)$	$4.3891001673 \times 10^{-13} - j7.6364655159 \times 10^{-14}$
$f''(0)$	$6.4052562294 \times 10^{-1} + j3.2440680707 \times 10^{-1}$
$f'''(0)$	$-6.6351740029 \times 10^{-1} - j7.8183592825 \times 10^{-1}$
$f(x_N)$	$-5.6961867836 \times 10^{3} + j1.4978518619 \times 10^{3}$
$f'(x_N)$	$-5.2551795558 \times 10^{2} + j6.7168531938 \times 10^{2}$
$f''(x_N)$	$-1.7214451750 + j1.2283799270 \times 10^{2}$
$f'''(x_N)$	$1.1669721466 \times 10^{1} + j1.4434271185 \times 10^{1}$

Table 3.3: Mode amplitude values at the input and output of the TWT as calculated from Chernin's matrix algorithm [37].

Parameter	Value
$f(x_N)$	$-5.6961867846 \times 10^{3} + j1.4978518639 \times 10^{3}$
$f'(x_N)$	$-5.2551795553 \times 10^{2} + j6.7168531971 \times 10^{2}$
$f''(x_N)$	$-1.7214451419 + j1.2283799274 \times 10^{2}$
$f'''(x_N)$	$1.1669721471 \times 10^{1} + j1.4434271186 \times 10^{1}$

Table 3.4: Mode amplitude values at the output of the TWT as calculated from the direct integration of Eq. (3.3).

3.3.3 Validation Case 3

The final validation calculation compares the direct integration code of the three-wave theory against the analytic results of those of Pierce in the case of a TWT that contains a lossy sever region. The loss profile is shown in Fig. 3.4. The local increase in the loss, d, is to damp the electromagnetic waves (for stability) while preserving the AC current on the beam [1]. In this calculation, we take values of $b = 1.023$, $C = 0.078$, and $QC = 0.114$ (Eqs. (2.3) - (2.5)).

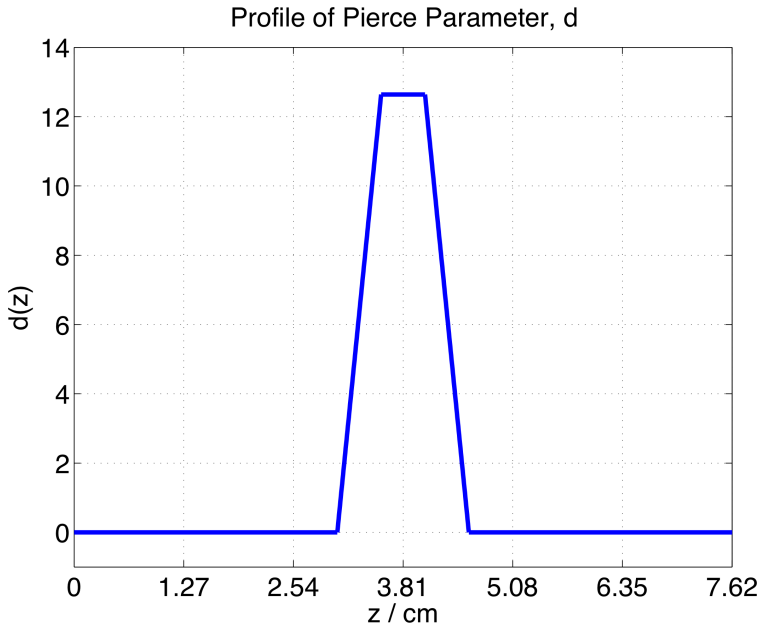

Figure 3.4: The profile for the Pierce loss parameter, $d(z)$, for the third validation case.

The results of the direct integration code compared to the analytic theory of Pierce can be seen in Fig. 3.5. The analytic theory of Pierce, called 'prc3' in Fig. 3.5, was performed by Chernin. As Fig. 3.5 shows, the gain as a function of distance between both methods is in excellent agreement.

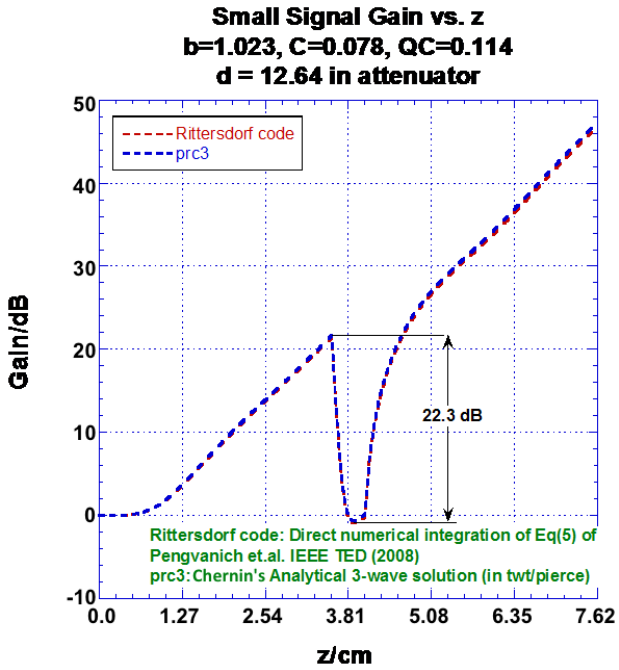

Figure 3.5: Gain as a function of distance, z, for both the direct integration calculation (Rittersdorf code) and the analytic theory of Pierce (prc3).

3.4 Key Results from the Backward Wave Study

Having validated the numerical scheme, this section presents some of the key findings on the effects of reflected waves as reported in Chernin et al. [37]. Let us first consider the standard case, a TWT of length $x = 100$, $b_0 = 0$, $C = 0.05$, and $d = QC = 0$. The TWT is broken up into $N = 100$ segments and the profile $b(x)$ is sampled from a Gaussian distribution with a mean of b_0 and a standard deviation of σ_b. Figure 3.6 shows both the mean variation from the error-free value and the corresponding standard deviations of those variations for both the three-wave model (from numerical integration of the governing equations) and the inclusion of the effects of internal reflections as a function of σ_b.

As Fig. 3.6 shows, the deviation from the error-free value increases with the inclusion of internal reflections within the model for increasing values of σ_b. Another

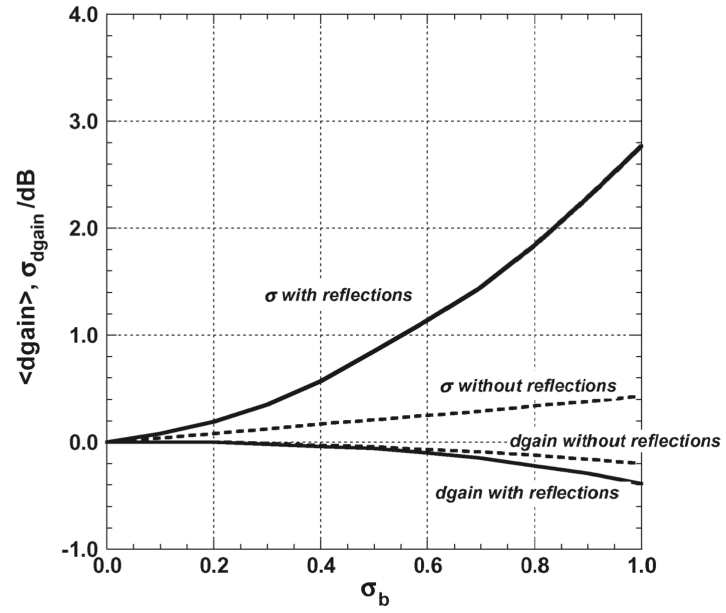

(a)

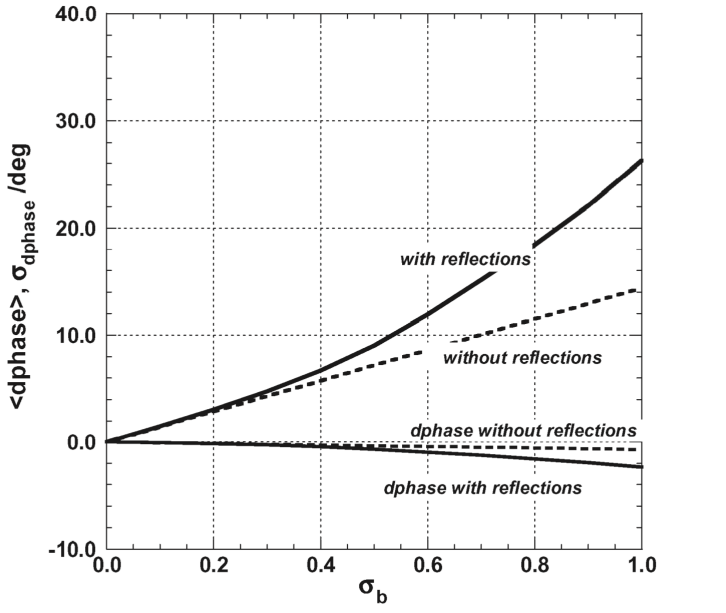

(b)

Figure 3.6: The mean variation and standard deviation from the error-free value for a TWT with random pitch errors as a function of σ_b. The dashed curves are the results of the calculation of the third-order model, i.e., in the absence of internal reflections. The solid curves are the results of the calculation of the fourth-order model, i.e., in the presence of internal reflections. Here, $x = 100$, $N = 100$, $C = 0.05$, and $b_0 = 0$ [37].

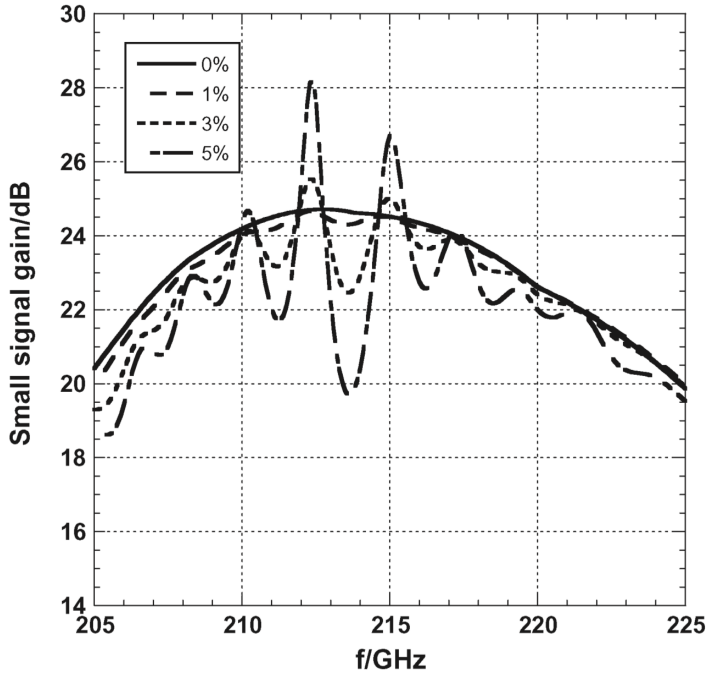

Figure 3.7: The small-signal gain as a function of frequency for different values of the standard deviation in the random pitch errors [37].

feature of Fig. 3.6 is that the increase in the mean variation due to internal reflections is much less than the corresponding increase in the standard deviations of those variations.

Figure 3.7 shows the small-signal gain as a function of frequency inside of the G-Band for different amplitudes of random error for a TWT with a beam voltage of $V_b = 11.7$ kV, a beam current of $I_b = 120$ mA, a circuit length of 1.2 cm, and an average circuit pitch of 0.02 cm. Typical Pierce parameter values in this tube are $C = 0.0197$ and $b = 0.36$ (see Fig. 2.24 and Chernin et al. [37]). Here, the amplitude of errors is measured in percentage and is defined by the standard deviation in the pitch divided by the average pitch. In the absence of random errors, the small-signal gain exhibits no gain ripple across the band. In the presence of pitch errors, a gain ripple forms and grows larger with increasing pitch error. At only a 5% pitch error the gain ripple is around 8 dB and regenerative oscillation, caused by internal feedback, becomes a distinct possibility [67].

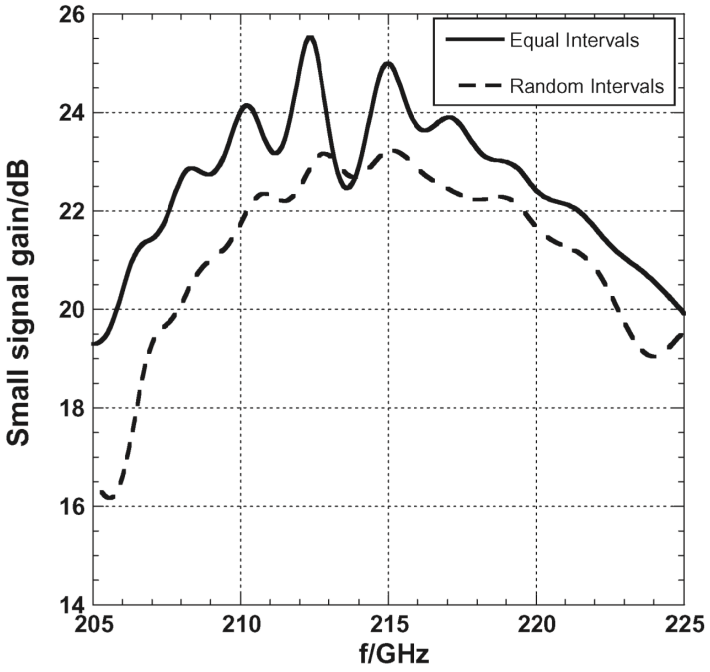

Figure 3.8: The small-signal gain as a function of frequency for a fixed standard deviation in the random pitch errors. The solid curve represents the calculation where the random pitch errors are evenly spaced. The dashed curve represents the calculation where the random pitch errors are distributed randomly along the axis of the TWT [37].

Figure 3.8 shows the same small-signal gain as a function of frequency, this time for a fixed pitch error of 3%, where the random errors are distributed evenly and then spaced at random intervals. When the pitch errors are randomly distributed along the axis of the TWT, the amplitude of the gain ripple is shown to be reduced.

3.5 Absolute Instability on an Electron Beam Inside a Dielectric Waveguide

In Section 3.4, we saw that a random distribution of b can cause internal wave reflections that lead to large gain ripples. An important question is whether such random internal reflections can lead to oscillations in a TWT. This generic question is very difficult to answer. Instead, we ask a more fundamental question: whether the dispersiveness in a slow wave structure can make a TWT undergo an absolute instability if the beam current is sufficiently high, even if such a TWT is pristine, i.e., an error-free tube. Absolute instability may occur even in a perfectly matched tube without reflection, as described more fully in the next paragraph. It turns out that this simpler question has not been adequately answered either[1] [74]. This section attempts to answer this simpler question by treating the *exact* dispersion relation of a sheet beam inside a dielectric waveguide. That is, the slow wave structure is provided by the dielectric medium. Despite its practical limitations, the dielectric waveguide does yield an exact dispersion relation that contains the reverse propagation mode. Such an exact formulation is *not* possible for the complicated helix structure, where the use of simplified governing equations for the helix structure, Eqs. (3.1) and (3.2), gave erroneous predictions on absolute instability[1] [74].

This is a general description of oscillation in a traveling wave tube amplifier [75].

[1]Lau showed that an absolute instability always exists according to the dispersion relation that is constructed from the simplified governing equations (3.1) and (3.2). The absolute instability, according to this simplified mode, cannot be stabilized even with the addition of cold-tube loss in these governing equations. This is contrary to intuition. It strongly suggests that a proper study of absolute instability requires accurate formulation of the dispersion relation.

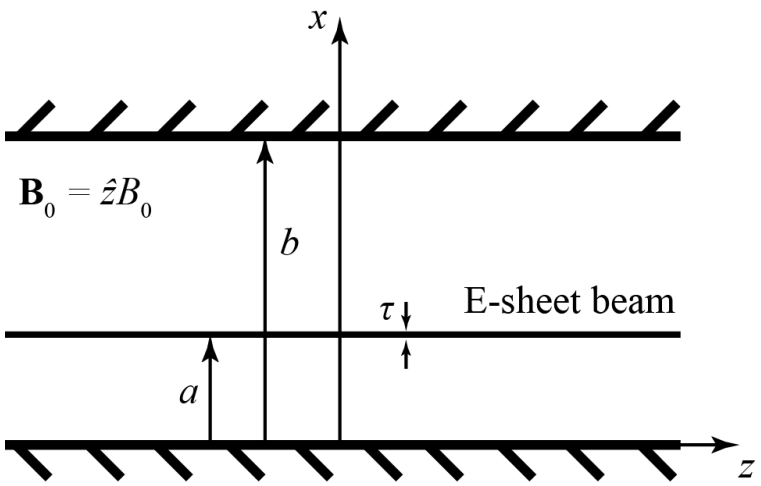

Figure 3.9: An electron sheet beam with thickness τ propagating through a dielectric waveguide in the $\hat{z}$-direction along an infinite magnetic field.

"Oscillations (in TWT amplifiers) are generally caused by either an external or an internal feedback process. The external feedback is provided by reflections at both ends of the interaction region. If the amplitude of the reflected signal reaches a certain level that the loop gain exceeds unity, the wave amplification processes become regenerative and oscillation consequently takes place. The internal feedback is a result of the dispersiveness of the unstable medium. Under certain conditions, the wave may grow locally without propagating axially out of the system. As a result, large amplitude waves can simply grow from noise level perturbations". Unlike those caused by end reflections, oscillations produced by internal feedback processes may occur in tubes that are perfectly matched at the input and output, and these oscillations are called absolute instability [71, 72]. The absolute instability was predicted and was later discovered in the gyrotron traveling wave amplifier [75].

We shall now consider the absolute instability of a sheet electron beam propagating in a smooth dielectric, planar waveguide, as shown in Fig. 3.9. The sheet beam has a small finite thickness τ, of density n_0, drifting at speed v_0, and guided by an infinite magnetic field in the z-direction. With $e^{j\omega t - jk_z z}$ dependence, the space charge wave inside this dielectric waveguide satisfies the dispersion relation [66],

$$D(\omega, k_z) = 0, \tag{3.7}$$

where

$$D(\omega, k_z) \equiv (\omega - k_z v_0)^2 + \omega_p^2 \left(\frac{\tau}{b}\right) pa \tan(pa), \tag{3.8}$$

$$p^2 = \omega^2 \epsilon \mu_0 - k_z^2, \tag{3.9}$$

where $\omega_p = (e^2 n_0 / m_e \epsilon)^{1/2}$. The derivation of Eq. (3.8) is shown in Appendix B, where we choose $b = 2a$ in Fig. 3.9 for simplicity.

Note that Eqs. (3.7) and (3.8) may also be written in the familiar form of the beam mode,

$$(\omega - k_z v_0)^2 = \omega_p^2 R(\omega, k_z), \tag{3.10}$$

where $R(\omega, k_z) = -(\tau/b) pa \tan(pa)$ is known as the "plasma reduction factor", that contains the beam and the waveguide geometries. R is singular when ω and k_z satisfy the cold tube dispersion relation of the dielectric waveguide, $\cos pa = 0$, yielding

$$k_z^2 = \omega^2 \epsilon \mu_0 - \left(\frac{\left(m - \frac{1}{2}\right)\pi}{a}\right)^2, \quad m = 1, 2, 3, \ldots \tag{3.11}$$

From Eq. (3.11), the cutoff frequency, ω_c, of the dielectric waveguide is given by

$$\omega_c a \sqrt{\epsilon \mu_0} = \left(m - \frac{1}{2}\right)\pi, \quad m = 1, 2, 3, \ldots \tag{3.12}$$

The beam mode, $\omega = k_z v_0$, and the circuit mode, Eq. (3.11), are shown in Fig. 3.10.

The TWT may operate at points A and B in this dispersion diagram, on which the beam velocity v_0 is equal to the circuit wave phase velocity ω/k_z. It is postulated

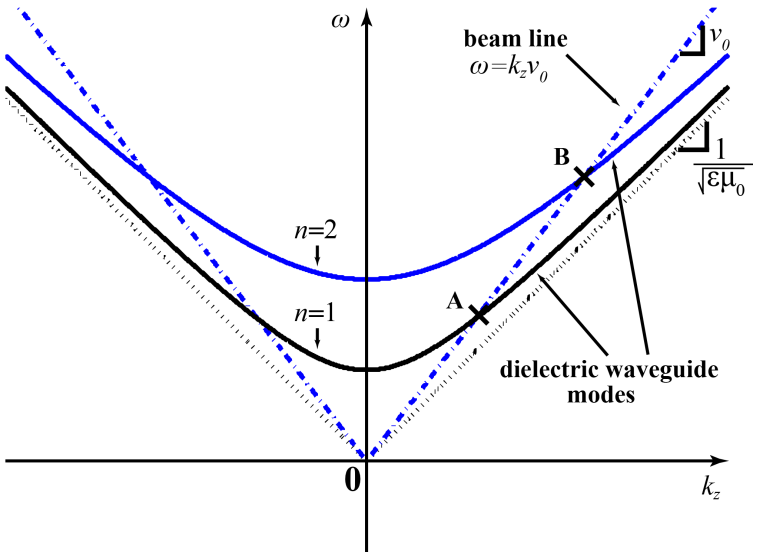

Figure 3.10: The dispersion diagram for the beam mode, $\omega = k_z v_0$, the dielectric waveguide circuit modes, Eq. (3.11), and the light line, $c = 1/\sqrt{\epsilon\mu_0}$.

that $v_0 > 1/\sqrt{\epsilon\mu_0}$ so that synchronism is possible (Fig. 3.10).

3.6 Briggs-Bers Criterion

Briggs and Bers [71, 72] derived a mathematical procedure that identifies absolute instability (assuming $e^{j\omega t - jk_z z}$ dependence) according to a general dispersion relation $D(\omega, k_z) = 0$ (Eq. (3.7)). An absolute instability occurs and oscillates at a natural frequency ω_s with $\mathrm{Im}(\omega_s) < 0$, if (ω_s, k_s) satisfies

$$D(\omega_s, k_s) = 0, \tag{3.13}$$

and

$$\left.\frac{\partial D}{\partial k}\right|_{\substack{\omega=\omega_s \\ k=k_s}} = 0. \tag{3.14}$$

Equations (3.13) and (3.14) are two equations which may be solved for the two unknowns, ω_s and k_s. Equation (3.13) is the dispersion relation $D(\omega, k_z) = 0$. Equa-

tion (3.14) is the condition for zero group velocity, $\partial\omega/\partial k = 0$, when ω cannot be expressed as a function of k_z explicitly from the dispersion relation. Note that if the dispersion relation $\omega = \omega(k_z)$ obtained from the general dispersion relation $D(\omega, k_z) = 0$ is analytic at $k_z = k_s$, then for $\omega \simeq \omega_s$, Eqs. (3.13) and (3.14) implies

$$\omega - \omega_s \simeq (\text{const}) \times (k_z - k_s)^2 , \tag{3.15}$$

i.e., two roots of k_s corresponding to one root of ω_s. Thus, $k = k_s$ is a saddle point at which $\partial\omega/\partial k = 0$, i.e., zero group velocity.

The Briggs-Bers test of whether (ω_s, k_s) corresponds to an absolute instability follows. Start with $\omega = \omega_s$. Allow ω to move downward to $-i\infty$ in the complex ω-plane (Fig. 3.11a) and solve for $k_z(\omega)$ from $D(\omega, k_z) = 0$ (Eq. (3.7)). If the double root k_s splits into the upper and lower half of the complex k-plane as $\omega \to -i\infty$, as in the case of $\overline{k}_{s1}$ in Fig. 3.11b, then an absolute instability exists. Otherwise, the convective instability exists, allowing spatial amplification of the amplifier, as in the roots $\overline{k}_{s2}$ and $\overline{k}_{s3}$ in Fig. 3.11b. Thus, at the onset of absolute instability, if there is one, it is obtained for real values of ω_s that satisfy Eq. (3.13) and (3.14). At the transition to absolute instability, $\text{Im}(\omega_s) = 0$. This substantially narrows the search for the threshold current for the onset of absolute instability.

In the normalization variables with $c \equiv 1/\sqrt{\epsilon\mu_0}$,

$$\overline{\omega} \equiv \frac{\omega a}{c}, \tag{3.16a}$$

$$\overline{k} \equiv ka, \tag{3.16b}$$

$$\overline{v}_0 \equiv \frac{v_0}{c} = v_0\sqrt{\epsilon\mu_0}, \tag{3.16c}$$

$$\overline{p} \equiv pa, \tag{3.16d}$$

$$n \equiv \omega_p^2 \left(\frac{\tau}{b}\right) \frac{a^2}{c^2}. \tag{3.16e}$$

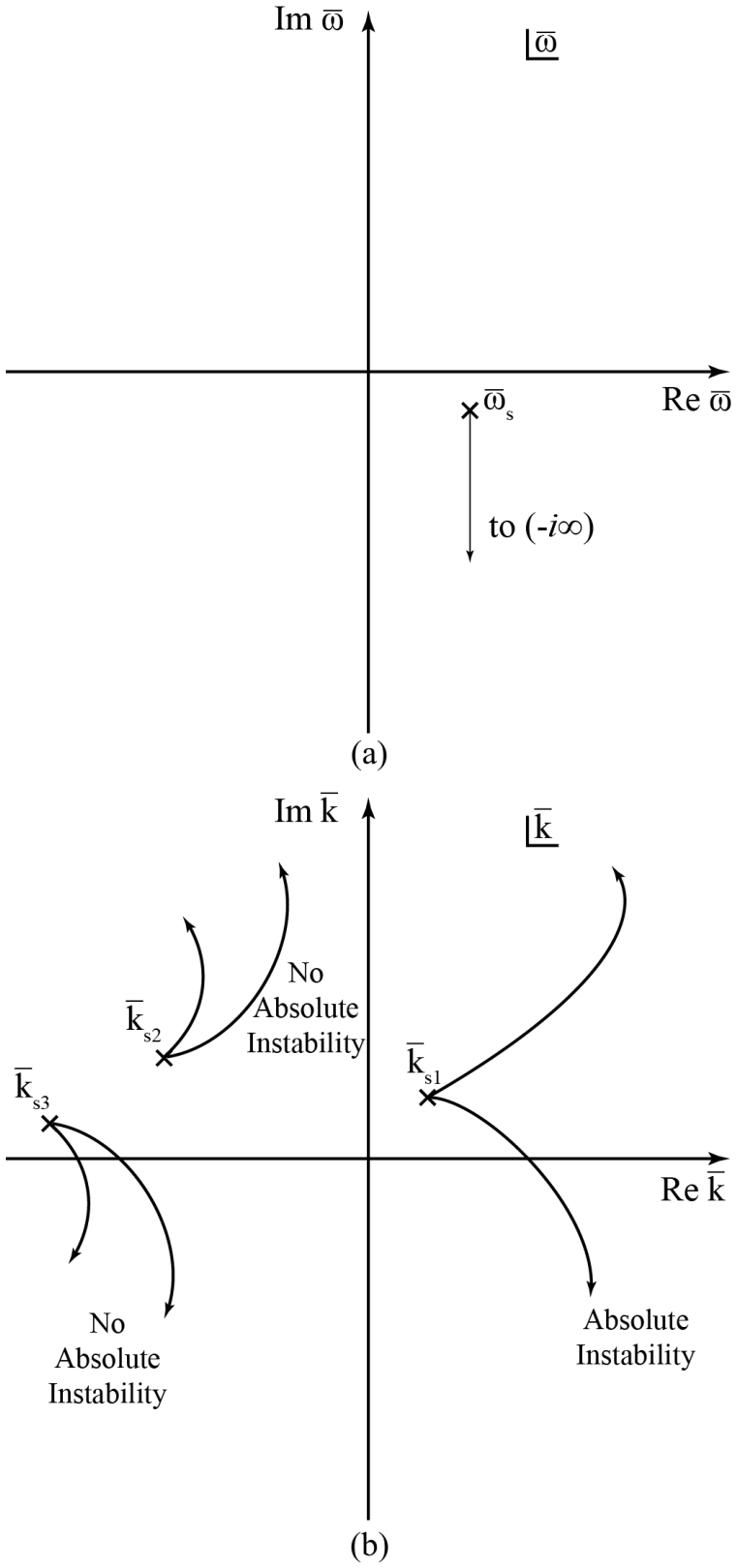

Figure 3.11: The Briggs-Bers stability criterion on the saddle points (ω_s, k_s). The root $(\overline{\omega}_s, \overline{k}_{s1})$ corresponds to an absolute instability. The roots $(\overline{\omega}_s, \overline{k}_{s2})$ and $(\overline{\omega}_s, \overline{k}_{s3})$ correspond to convective instabilities.

Here, n is a measure of the coupling which is proportional to C^3 because both n and C^3 are proportional to the beam current. The dispersion relation, Eq. (3.7), can then be written as $D(\overline{\omega}, \overline{k}) = 0$, where,

$$D(\overline{\omega}, \overline{k}) = \left(\overline{\omega} - \overline{k}\overline{v}_0\right)^2 + n\overline{p}\tan\overline{p}. \tag{3.17}$$

To determine the existence of (or nonexistence of) the absolute instability we find the points $(\overline{\omega}, \overline{k}) = (\overline{\omega}_s, \overline{k}_s)$ that satisfy the dispersion relation, $D(\overline{\omega}, \overline{k}) = 0$, and $\partial\omega/\partial k = 0$.

It is useful to define $f(\overline{\omega}, \overline{k}) \equiv \overline{p}\tan\overline{p}$, such that the dispersion relation reads

$$D(\overline{\omega}, \overline{k}) = \left(\overline{\omega} - \overline{k}\overline{v}_0\right)^2 + nf(\overline{\omega}, \overline{k}). \tag{3.18}$$

Taking the differential of Eq. (3.18) yields

$$2(\overline{\omega} - \overline{k}\overline{v}_0)(d\overline{\omega} - \overline{v}_0 d\overline{k}) = -n\left(\frac{\partial f}{\partial\overline{\omega}}d\overline{\omega} + \frac{\partial f}{\partial\overline{k}}d\overline{k}\right). \tag{3.19}$$

Equation (3.19) is of the form $Ad\overline{\omega} - Bd\overline{k} = 0$, where A and B are the coefficients that result from casting Eq. (3.19) in this form. The zero group velocity condition implies that the coefficient $B = 0$. This implies that

$$2\overline{v}_0(\overline{\omega} - \overline{k}\overline{v}_0) = n\frac{\partial f}{\partial\overline{k}}. \tag{3.20}$$

From Eq. (3.18) by (3.20), we eliminate n to yield

$$g(\overline{\omega}, \overline{k}) \equiv \frac{\partial f/\partial\overline{k}}{f} - \frac{2\overline{v}_0}{(\overline{\omega} - \overline{k}\overline{v}_0)} = 0. \tag{3.21}$$

By evaluating the derivative of f

$$\frac{\partial f}{\partial\overline{k}} = -\overline{k}\left(\sec^2\overline{p} + \frac{\tan\overline{p}}{\overline{p}}\right), \tag{3.22}$$

we can, after some trigonometry, express $g(\overline{\omega}, \overline{k})$ as

$$g(\overline{\omega}, \overline{k}) \equiv \overline{k}(\overline{\omega} - \overline{k}\overline{v}_0)(1 + \operatorname{sinc}\overline{p}\cos\overline{p}) - 2\overline{v}_0\overline{p}\sin\overline{p}\cos\overline{p}. \tag{3.23}$$

The procedure for solving this problem, assuming real $\overline{\omega}_s$ for the onset of absolute instability, is to solve Eq. (3.23) for the corresponding value of $\overline{k}_s$. Given this $(\overline{\omega}_s, \overline{k}_s)$ pair, the value of n can be obtained from Eq. (3.18),

$$n = -\frac{(\overline{\omega}_s - \overline{k}_s\overline{v}_0)^2}{f(\overline{\omega}_s, \overline{k}_s)}. \tag{3.24}$$

It is required that the corresponding value of n is purely real and positive for the answer to be physical. Thus, we scan over a large range of real values of $\overline{\omega}_s$ and determine the minimum value of n so obtained.

The final step is to then test to see if the n's so obtained correspond to the onset of absolute instability. Letting the imaginary part of the frequency go to negative infinity, $\overline{\omega}_i \to -\infty$, we look at the splitting of the roots of $\overline{k}$ and subject them to the Briggs-Bers criterion [71, 72] as shown in Fig 3.11. If the roots of $\overline{k}$ do not split in the complex $\overline{k}$-plane as $\overline{k}_{s2}$ and $\overline{k}_{s3}$ do in Fig. 3.11b, the solution $(\overline{\omega}, \overline{k})$ corresponds to a convective instability. If the roots of $\overline{k}$ split into the half $\overline{k}$-planes, as $\overline{k}_{s1}$ does in Fig. 3.11b, the solution $(\overline{\omega}, \overline{k})$ corresponds to an absolute instability. We identify the lowest value of n determined this way to give the threshold current beyond which the TWT amplifier is unstable with respect to absolute instability.

One set of threshold values of n as a function $\overline{v}_0$ using the above algorithm is shown in Fig. 3.12. This curve was obtained with the help of Derek Hung. For this set, the oscillation frequencies are close to the cutoff frequency given by Eq. (3.12) with $m = 1$. Other sets of values of n as a function of $\overline{v}_0$ have also been obtained; the corresponding values of oscillation frequency are always at the cutoff frequencies, i.e., given by $m = 1, 2, 3, \ldots$ in Eq. (3.12). Even for $m = 1$, additional calculations

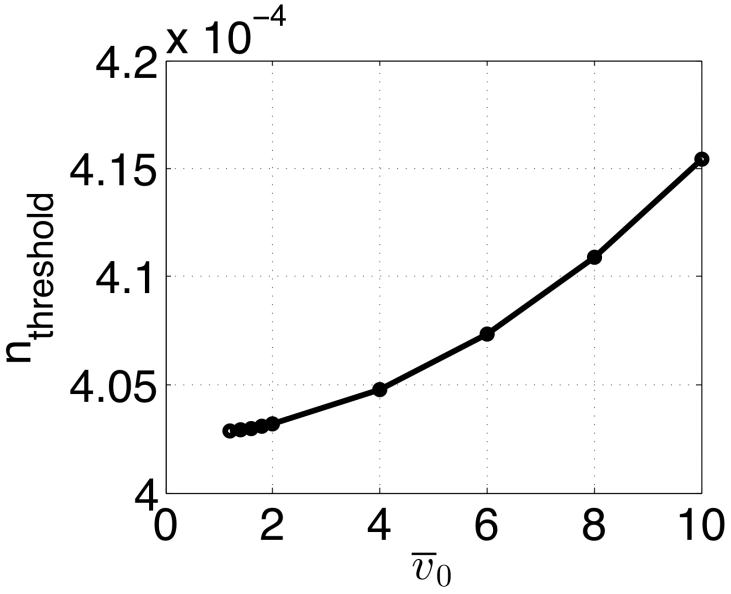

Figure 3.12: Threshold value of n as a function of $\overline{v}_0$ for the onset of absolute instability.

have shown that it is possible for smaller values of n compared to those in Fig. 3.12 to exist, but we are not certain whether they are artifacts due to numerical tolerances or meaningful values at this time.

3.7 Summary and Conclusions

The effects of the backward wave due to internal reflections that result from random manufacturing errors in the slow wave circuit of a TWT have been investigated. The circuit equation was modified such that the governing equation becomes a fourth order equation, giving rise to the backward wave in the model. An algorithm to calculate the mode amplitude in all segments of the TWT was developed [37] and validated by the numerical integration code. The effects of the internal reflections were shown to increase the mean variation and the standard deviation of the gain and phase from the error-free value from the results of the traditional Pierce model that contained only three forward waves. The increase in the standard deviation is much larger than the corresponding increase in the mean variation due to the internal

reflections. Finally, the effects of the random pitch errors were investigated on the effects of a G-Band TWT and they are shown to cause a gain ripple across the band.

The absolute instability of a TWT in a dielectric waveguide is investigated. A derivation of the exact dispersion relation for an electron beam in a dielectric waveguide is given. From the exact dispersion relation, an algorithm detailing how to determine the presence of the absolute instability is outlined. For a fixed, real frequency $\overline{\omega}_s$, the dispersion relation is solved to determine the complex wavenumber, $\overline{k}_s = \overline{k}_r - i\overline{k}_i$, representing growth or decay in the spatial coordinate. The root $(\overline{\omega}_s, \overline{k}_s)$ is then subject to the Briggs-Bers stability criterion, which determines the presence of either the convective or absolute instability. The threshold condition for the onset of absolute instability is determined for this idealized model.

CHAPTER 4

Temporal and Spatial Locking of Nonlinear Systems

4.1 Introduction

Phase-locking is utilized today in many important applications, ranging from small scale devices such as cardiac pacemakers [76] to large scale devices such as radar [10]. The well-known configuration is the "master-slave," where the driver, known as the "master," is unaffected by the driven oscillator, known as the "slave" [45, 77]. In this configuration, the condition for locking of the "slave" oscillator to the frequency of the "master" is given by the Adler locking condition [45],

$$\frac{|\omega_d - \omega_0|}{\omega_0} < \frac{\rho}{2Q_{ext}}, \tag{4.1}$$

where ω_d is the frequency of the driver (master), ω_0 is the frequency of the free-running oscillator (slave), ρ is the ratio of injected (driver) signal voltage to driven oscillator's output voltage, and Q_{ext} is the external quality factor of the output oscillator. This expression describes the condition for the phase locking of high power microwave oscillators in general, including the magnetron, although it has recently been shown that the injection power in certain high power microwave oscillators need not be limited by Adler's locking condition [78].

An alternate is the peer-to-peer configuration, where each oscillator acts as a driver of, and a slave to, the other oscillator [53, 54]. The latter is attractive when locking a larger number of oscillators is desired, because far fewer expensive components, such as isolators or circulators, are required. The condition for peer-to-peer locking of two nonlinear oscillators was recently derived [53], and experimentally verified using two kilowatt oven magnetrons [54]. In this chapter, we shall advance the theory a step further. We examine the viability of peer-to-peer locking when both oscillators suffer a frequency upchirp, or contain a low frequency noise component [26].

Phase locking of two oscillators in the (ω, t) domain (ω = frequency, t = time) was recently found to have an analogue in the phase locking of two spatial modes in the (k, z) domain (k = wavenumber, z = axial direction). In z-pinch experiments performed at the Sandia National Laboratories [18, 20, 22, 79], Cornell University [80–83], and the University of Michigan [25, 84, 85], current on the order of $10 - 100$s of kiloamperes is made to pass through each metallic wire in a wire array. The diameter of the wires is typically tens of microns and the axial length is of order 1 cm. The intense current ablates the wire and the current-carrying plasma column always exhibits a sausage-like instability along the wire with a certain characteristic wavelength. When the separation of the wires is large, the axial perturbation on each wire is independent of its neighbor. However, when the wires are placed sufficiently close to each other, it is experimentally observed that the "sausage" modes on the wire become axially correlated (See Fig. 4.10 below). The spatial correlation of the axial modes that appeared on two (and more) ablated wires has been systematically studied [25]; it is of substantial interest to the Sandia National Laboratories' "Z" machine [86–90]. This chapter will treat this spatial locking as the spatial analog of peer-to-peer locking of nonlinear oscillators. The (ω, t) space is replaced by (k, z) space, even though the coupling mechanisms for the two cases are entirely different. Here, k is the characteristic wave number of the instability mode on a single, isolated

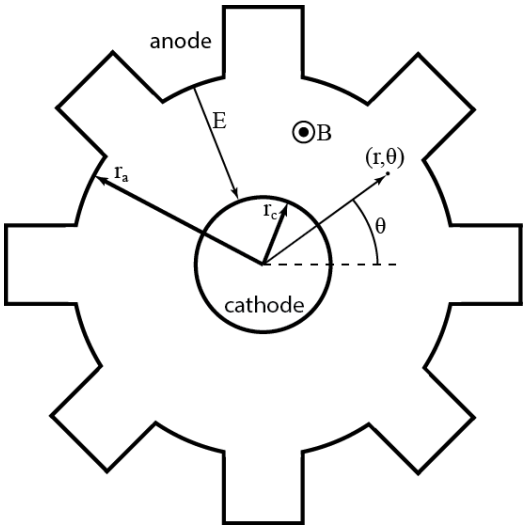

Figure 4.1: Geometry of a cylindrical magnetron with the cathode in the center. A vane slow wave structure is depicted on the anode.

wire [85, 87, 91, 92].

Section 4.2 outlines the model for peer-to-peer locking of two magnetrons and presents the condition of locking [53]. This paved the way for Section 4.3, where we consider the effects of a frequency chirp on the locking of two oscillators. The frequency chirp extends beyond the local locking range. Section 4.4 considers the effect of a background noise on peer-to-peer locking. Bounds on the output phase variations are derived analytically and compared favorably with numerical computations. Section 4.5 considers locking of axial modes on two closely ablated wires. Section 4.6 summarizes this chapter.

4.2 Peer-to-Peer Locking of Two Magnetrons

A conventional oven magnetron is employed in the cylindrical geometry, although the planar magnetron works on similar physical principles. Commercial magnetrons typically operate at few kV all the way up to 100 kV. Current is emitted thermionically from the cylindrical cathode at the center. An axial magnetic field is imposed. The emitted electrons experience an electric field in the radial direction that causes them

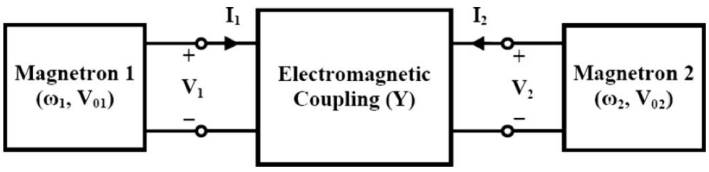

Figure 4.2: A schematic showing two magnetrons connected to a two-port network for the peer-to-peer locking configuration. Figure from [53].

to $E \times B$ drift in the azimuthal direction (Fig. 4.1).

As the electrons flow in the azimuthal direction around the cathode, they experience electric field perturbations from the slow wave structure, an example is shown in Fig. 4.1 with a vane structure. When the $E \times B$ drift velocity is approximately equal to the azimuthal phase velocity of the slow wave on the structure, the electrons will continuously interact with the wave as they travel around the interaction space of the magnetron. Electron spokes are formed, in which the electron drifts toward the anode, converting their potential energy into RF energy [1]. The RF wave is typically coupled out of the structure at the end of one or several vanes.

We now consider the locking of two such magnetrons, 1 and 2, schematically shown in Fig. 4.2. To study the effects of a frequency chirp and of noise on peer-to-peer locking, we need to describe the model for noise free magnetrons, following [53]. Each operating magnetron is a free-running oscillator. The theory of peer-to-peer locking of nonlinear oscillators is modeled by considering the two magnetrons being connected through a two-port admittance matrix, $\mathbf{Y}$, as shown in Fig. 4.2. Each magnetron is modeled by a parallel RLC circuit as shown in Fig. 4.3. From the conservation of current, it can be shown that

$$\frac{V_2}{R_2} + \frac{V_2}{j\omega L_2} + j\omega C_2 V_2 + Y_{B2} V_2 = -I_2. \tag{4.2}$$

When $I_2 = 0$, the magnetron is in its free-running state. That is, I_2 represents an external current that is used to drive magnetron 2. In the "master-slave" injection

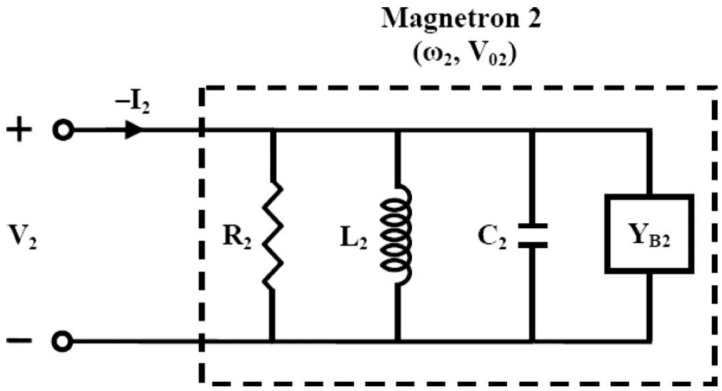

Figure 4.3: Magnetron 2 modeled as an RLC circuit. I_2 and V_2 are output current and voltage, respectively. The resistance, inductance, and capacitance are R_2, L_2, and C_2, respectively. Y_{B2} is the admittance due to beam loading, e.g., $Y_{B2} = 0$ in the absence of the beam. Figure from [53].

locking configuration, the current I_2 is a constant quantity. In the case of peer-to-peer coupling, the current I_2 is no longer constant; the combination of magnetron 1 and the coupling between magnetrons 1 and 2 gives rise to the value of I_2, which may be time varying.

Since we are interested in temporal effects, we write Eq. (4.2) in the time domain form [53],

$$\frac{d^2V_2}{dt^2} + \frac{\omega_2}{Q_2}\left[1 - \frac{|V_2|}{V_{02}}\right]\frac{dV_2}{dt} + \omega_2^2 V_2 = -\frac{1}{C_2}\frac{dI_2}{dt}, \tag{4.3}$$

where ω_2 is the free-running frequency of magnetron 2, V_{02} is the free-running voltage amplitude of magnetron 2, and C_2 is the capacitance of magnetron 2. The solution of magnetron 2 in the free-running state, e.g., $I_2 = 0$ is simply $V_2(t) = V_{02}e^{j\omega_2 t - j\phi}$, where ϕ is an arbitrary phase. When connected to magnetron 1, e.g., $I_2 \neq 0$, the voltage is modified to read (if locking occurs),

$$V_2(t) = V_2 e^{j\omega t + j\theta_2}, \tag{4.4}$$

where θ_2 is the phase of magnetron 2 relative to magnetron 1, ω is the locked frequency,

and V_2 is the amplitude of magnetron 2. The analysis for magnetron 1 is exactly the same with subscripts 1 and 2 reversed. Since we assume that the two magnetrons are coupled together through a two-port admittance matrix, as in Fig. 4.2, we write [53]

$$\begin{bmatrix} I_1 \\ I_2 \end{bmatrix} = \begin{bmatrix} Y_{11} & Y_{12} \\ Y_{21} & Y_{22} \end{bmatrix} \begin{bmatrix} V_1 \\ V_2 \end{bmatrix}. \tag{4.5}$$

The admittances in Eq. (4.5) are, in general, allowed to be complex and are defined as

$$Y_{mn} = |Y_{mn}|e^{jp_{mn}} = \mathrm{Re}(Y_{mn}) + j\mathrm{Im}(Y_{mn}), \tag{4.6}$$

where p_{mn} is the phase of element mn. Substituting Eqs. (4.4) and (4.5) into Eq. (4.3) yields

$$-\omega^2 V_2 + \frac{\omega_2}{Q_2}\left[1 - \frac{|V_2|}{V_{02}}\right] j\omega V_2 + \omega_2^2 V_2 = -\frac{1}{C_2}\frac{d}{dt}\left(Y_{21}V_1 + Y_{22}V_2\right). \tag{4.7}$$

Assuming that the admittances Y_{21}, Y_{22} slowly vary in time such that $V dY/dt \ll Y dV/dt$, we write

$$\left(\omega_2^2 - \omega^2\right) V_2 + \frac{\omega_2}{Q_2}\left[1 - \frac{|V_2|}{V_{02}}\right] j\omega V_2 = -\frac{1}{C_2}\left(Y_{21}\frac{dV_1}{dt} + Y_{22}\frac{dV_2}{dt}\right). \tag{4.8}$$

Factoring ω^2 from Eq. (4.8) allows the first term to be written as $\omega^2(\omega_2^2/\omega^2 - 1)$. Since the ratio of ω_2/ω is close to unity for locking, let us define $\epsilon = \omega_2/\omega - 1$, where $\epsilon \ll 1$. This allows us to make the approximation

$$\left(\frac{\omega_2}{\omega}\right)^2 = (1+\epsilon)^2 \approx 1 + 2\epsilon. \tag{4.9}$$

After substituting Eq. (4.9), evaluating the derivatives, and some algebra we express Eq. (4.8) as

$$2jC_2(\omega_2 - \omega) - \frac{\omega_2}{Q_2}\left[1 - \frac{|V_2|}{V_{02}}\right] = Y_{21}\frac{V_{10}}{V_{20}}e^{j(\theta_1-\theta_2)} + Y_{22}. \tag{4.10}$$

It is convenient to express the three circuit parameters R_2, L_2, and C_2 as three measurable cold-tube quantities. These quantities are the natural frequency ω_{02}, the quality factor Q_{02}, and the shunt impedance Z_2. In the absence of the beam loading term, Y_{B2}, shown in Fig. 4.3, they are defined as

$$\omega_{02} = \sqrt{\frac{1}{L_2C_2}}, \tag{4.11a}$$

$$Q_{02} = \omega_{02}R_2C_2, \tag{4.11b}$$

$$Z_2 = R_2/Q_{02}. \tag{4.11c}$$

The presence of beam loading gives rise to the hot natural frequency, ω_2, and the hot quality factor, Q_2. The shunt impedance remains approximately unchanged in the presence of beam loading [55]. Substituting Eqs. (4.11) into Eq. (4.10) yields

$$2jC_2(\omega_2 - \omega) - \frac{1}{Z_2Q_2}\left[1 - \frac{|V_2|}{V_{02}}\right] = Y_{21}\frac{V_{10}}{V_{20}}e^{j(\theta_1-\theta_2)} + Y_{22}. \tag{4.12a}$$

Similarly for magnetron 1

$$2jC_1(\omega_1 - \omega) - \frac{1}{Z_1Q_1}\left[1 - \frac{|V_1|}{V_{01}}\right] = Y_{12}\frac{V_{20}}{V_{10}}e^{j(\theta_2-\theta_1)} + Y_{11}. \tag{4.12b}$$

Taking the real part of Eqs. (4.12) yields

$$\frac{|V_2|}{V_{02}} = 1 + Q_2Z_2\left[\mathrm{Re}(Y_{22}) + \mathrm{Re}(Y_{21})\frac{V_{10}}{V_{20}}\cos(p_{21} + \theta_1 - \theta_2)\right]. \tag{4.13a}$$

Similarly for magnetron 1

$$\frac{|V_1|}{V_{01}} = 1 + Q_1Z_1\left[\mathrm{Re}(Y_{11}) + \mathrm{Re}(Y_{12})\frac{V_{20}}{V_{10}}\cos(p_{12} + \theta_2 - \theta_1)\right]. \tag{4.13b}$$

Taking the imaginary part of Eqs. (4.12) yields

$$\omega - \left(\omega_2 - \frac{1}{2}\omega_2 Z_2 \mathrm{Im}(Y_{22})\right) = -\frac{1}{2}\omega_2 Z_2 |Y_{22}| \frac{V_{10}}{V_{20}} \sin(p_{21} + \theta_1 - \theta_2), \tag{4.14a}$$

$$\omega - \left(\omega_1 - \frac{1}{2}\omega_1 Z_1 \mathrm{Im}(Y_{11})\right) = -\frac{1}{2}\omega_1 Z_1 |Y_{11}| \frac{V_{20}}{V_{10}} \sin(p_{12} + \theta_2 - \theta_1). \tag{4.14b}$$

Let

$$\Omega_1 = \omega_2 - \frac{\omega_1}{2} Z_1 \mathrm{Im}(Y_{11}), \tag{4.15a}$$

$$\Omega_2 = \omega_2 - \frac{\omega_2}{2} Z_2 \mathrm{Im}(Y_{22}), \tag{4.15b}$$

and

$$\alpha_1 = \frac{\omega_1}{2} Z_1 |Y_{12}| \frac{V_{20}}{V_{10}}, \tag{4.16a}$$

$$\alpha_2 = \frac{\omega_2}{2} Z_2 |Y_{21}| \frac{V_{10}}{V_{20}}. \tag{4.16b}$$

Equation (4.14) then becomes, for both magnetron 1 and 2

$$\omega - \Omega_1 = -\alpha_1 \sin(p_{12} + \theta_2 - \theta_1), \tag{4.17a}$$

$$\omega - \Omega_2 = -\alpha_2 \sin(p_{21} + \theta_1 - \theta_2). \tag{4.17b}$$

Subtracting Eq. (4.17b) from Eq. (4.17a) yields

$$\Omega_2 - \Omega_1 = \alpha_2 \sin(p_{21} + \theta_1 - \theta_2) - \alpha_1 \sin(p_{12} + \theta_2 - \theta_1). \tag{4.18}$$

Since only the relative phase between magnetron 1 and magnetron 2 is important, we can, without loss of generality, set $\theta_1 = 0$. By doing so, Eq. (4.18) can be expressed

as

$$\Omega_2 - \Omega_1 = \alpha_2 \sin(p_{21} - \theta_2) - \alpha_1 \sin(p_{12} + \theta_2) \tag{4.19}$$

We require that the solution to θ_2 be purely real. We can show the condition for purely real solutions of θ_2 if we define

$$\bar{p} \equiv \frac{1}{2}(p_{12} + p_{21}), \tag{4.20a}$$

$$\phi \equiv \delta p + \theta_2 - \theta_1, \tag{4.20b}$$

$$\delta p \equiv \bar{p} - p_{21} = p_{12} - \bar{p}. \tag{4.20c}$$

We can then see that Eq. (4.19) is of the form

$$c = a \sin\phi + b \cos\phi, \tag{4.21}$$

where $a = -(\alpha_1 + \alpha_2)\cos\bar{p}$, $b = -(\alpha_2 - \alpha_1)\sin\bar{p}$, and $c = \Omega_2 - \Omega_1$. For real values of a, b, and c, Eq. (4.21) then only admits real solutions for ϕ, that is to say θ_2, if and only if $c^2 < a^2 + b^2$. Substituting Eqs. (4.20) into Eq. (4.21) yields

$$\alpha_1^2 + \alpha_2^2 + 2\alpha_1\alpha_2 \cos(p_{12} + p_{21}) > (\Omega_2 - \Omega_1)^2, \tag{4.22}$$

which is the peer-to-peer locking condition [53]. Equation (4.22) states that if the free-running frequencies Ω_1 and Ω_2 of the two oscillators are far apart, it is impossible to lock at a fixed coupling strength, α_1 and α_2.

The locking condition Eq. (4.22) was verified in experiments [54].

4.3 Effects of Frequency Chirping on Peer-to-Peer Locked Magnetrons

Consider first the peer-to-peer locking of two nonlinear oscillators in the presence of a frequency chirp. In complex notation, we represent the signal on the ith oscillator ($i = 1, 2$) as $V_i(t)e^{j\omega t - j\theta_i(t)}$, where ω is the frequency; V_i and θ_i are, respectively, the amplitude and phase of signal i, both assumed to be slowly time-varying compared with ω. The governing equation for the phases may be written as (cf. Eqs. (4.17a) and (4.17b))

$$\frac{d\theta_1}{dt} + \Omega_1 - \omega = \alpha_1 \sin(p_{12} + \theta_2 - \theta_1), \tag{4.23a}$$

$$\frac{d\theta_2}{dt} + \Omega_2 - \omega = \alpha_2 \sin(p_{21} + \theta_1 - \theta_2), \tag{4.23b}$$

where Ω_1 (Ω_2) is the free-running frequency of oscillator 1 (oscillator 2) when the other is turned off, α_1 (α_2) is the effect on oscillator 1 (oscillator 2) by oscillator 2 (oscillator 1) because of the coupling, and p_{12} and p_{21} represent the phase advances on the coupling paths. When oscillator 2 is turned off, $\alpha_1 = 0$ and $\omega = \Omega_1$ on oscillator 1 according to Eq. (4.23a); the phase θ_1 on oscillator 1 is an arbitrary constant, as expected of any free-running oscillator. The free-running oscillator 1 is assumed to have a fixed amplitude V_1. Similarly, oscillator 2 has a free-running frequency Ω_2, a fixed amplitude V_2, and an arbitrary phase θ_2.

When Ω_1 and Ω_2 are constants, the two oscillators are locked to a common frequency (ω) if the locking condition, Eq. (4.22), is satisfied [53]. This condition was validated in experiments performed by Cruz et al. using two kilowatt-magnetrons [54], for which the parameters α_1, α_2, p_{12}, and p_{21} were obtained from the admittance matrix that described the electromagnetic coupling between the two magnetrons. For the following calculations, we chose values for these parameters from a deeply locked

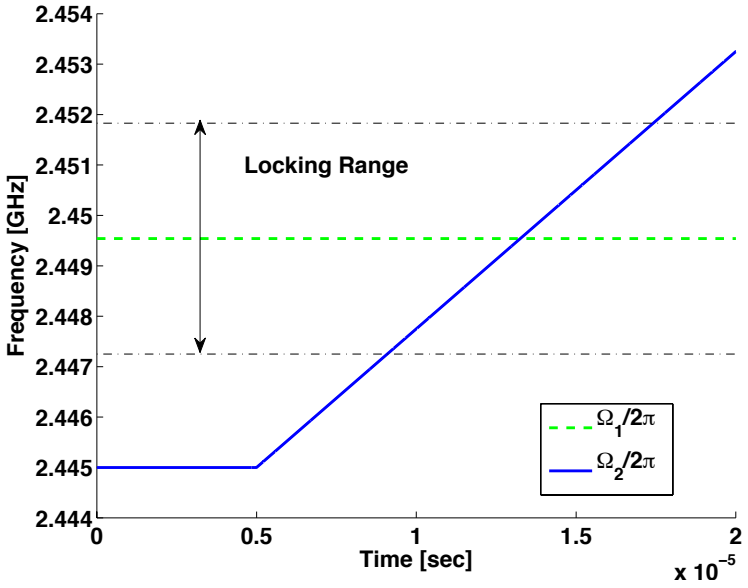

Figure 4.4: Frequency profiles for magnetron 1 (dashed green) and magnetron 2 (solid blue). The frequency of magnetron 1 is held constant while a linear frequency chirp begins in magnetron 2 at $t = 5$ μs. The two black dashed horizontal lines show the boundaries of the locking range as predicted by Eq. (4.22).

case from the Cruz experiments [54]. These values are listed in Table 4.1.

Parameter	Experimental Value
$\Omega_1/2\pi$	2.44953 GHz
$\Omega_2/2\pi$	2.44807 GHz
α_1	1.442 $\times 10^{-3}$ GHz
α_2	9.347 $\times 10^{-4}$ GHz
p_{12}	-0.202979 rad
p_{21}	0.745879 rad

Table 4.1: List of values used in the calculations in this chapter as determined experimentally by Cruz et al. [54].

How the locking is altered if there are frequency chirps in the free-running frequencies Ω_1 and Ω_2 can readily be answered by subtracting Eq. (4.23a) from Eq. (4.23b),

$$\frac{d(\theta_2 - \theta_1)}{dt} + (\Omega_2 - \Omega_1) = \alpha_2 \sin(p_{21} + \theta_1 - \theta_2) - \alpha_1 \sin(p_{12} + \theta_2 - \theta_1), \qquad (4.24)$$

which is a single equation for the phase difference $(\theta_2 - \theta_1)$. It is clear from Eq. (4.24) that this phase difference $(\theta_2 - \theta_1)$ cannot be a constant if $(\Omega_2 - \Omega_1)$ is time-varying. Therefore, strictly speaking, there is no locking in the phase if there is a frequency drift between the free-running frequencies Ω_1 and Ω_2. Furthermore, since only the frequency difference $(\Omega_2 - \Omega_1)$ enters in Eq. (4.24), we may pretend that Ω_1 is a constant but let Ω_2 vary with time. For simplicity, we shall write this linear frequency chirp in the free-running frequency of magnetron 2 as

$$\Omega_2(t) = \Omega_{20} + (t - t_s)\frac{d\Omega_2}{dt}, \tag{4.25}$$

where Ω_{20} is the constant frequency, t_s is the time at which the frequency chirp begins, and $d\Omega_2/dt$ is the chirping rate, which is zero when $t < t_s$ and is assumed to be constant when $t \geq t_s$. Additionally, the chirping rate is assumed to be slow in comparison to Ω_{20}. Figure 4.4 shows an example of a linear chirp in Ω_2, which allows us to pinpoint the drift in the relative phase $(\theta_2 - \theta_1)$ as the frequency difference $(\Omega_2 - \Omega_1)$ moves across the locking range, Eq. (4.22) [52]. Here, we chose a moderate value for the frequency chirp of $\Omega_2/dt = 2\pi \times 5.5 \times 10^{11}$ GHz/s which begins at time $t_s = 5$ μs.

Figure 4.5 shows the instantaneous drift rate of the relative phase, $d\phi/dt$, where $\phi = \theta_2 - \theta_1$. It is obtained by solving Eq. (4.24) using the linear chirp in Fig. 4.4. From Fig. 4.5, we see that this instantaneous drift rate is close to zero but not exactly equal to zero, when the frequency difference $(\Omega_2 - \Omega_1)$ lies within the locking range. Thus, while perfect phase locking cannot be achieved if there is a frequency drift between the two nonlinear oscillators, approximate phase locking can be attained if the locking condition (4.22) is satisfied locally in time. In Fig. 4.5, during the flat portion of the locking range, $|d\phi/dt| < 4 \times 10^5$ rad/s.

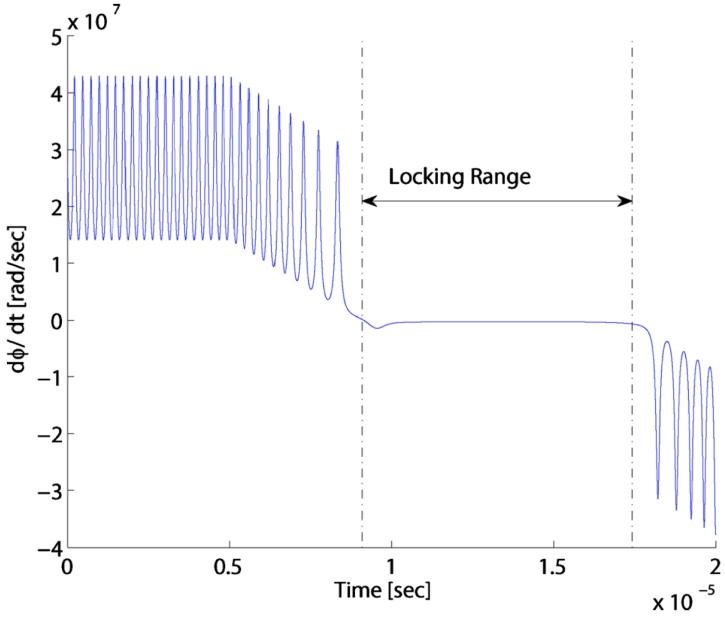

Figure 4.5: $d\phi/dt$ during the linear frequency chirp. Here, $\Omega_1/2\pi = 2.4496$ GHz and the linear chirp in Ω_2 starts at $t = 5$ μs. The dashed lines show the boundaries of when the locking condition is satisfied. The magnitude of $|d\phi/dt|$ is less than 4×10^5 rad/s inside of the locking range.

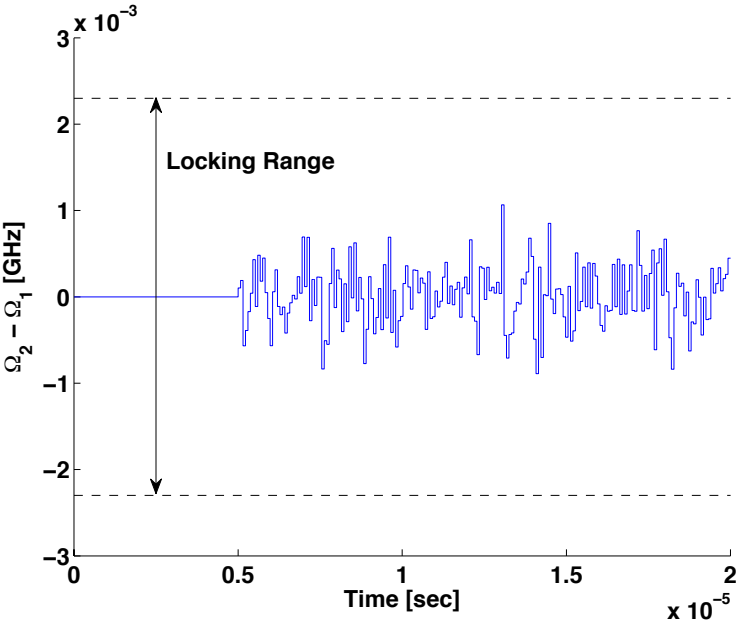

Figure 4.6: Profile of random frequency fluctuations between magnetron 1 and 2 with 200 nodes over the range shown. The two black dashed horizontal lines show the boundaries of the locking range as predicted by Eq. (4.22).

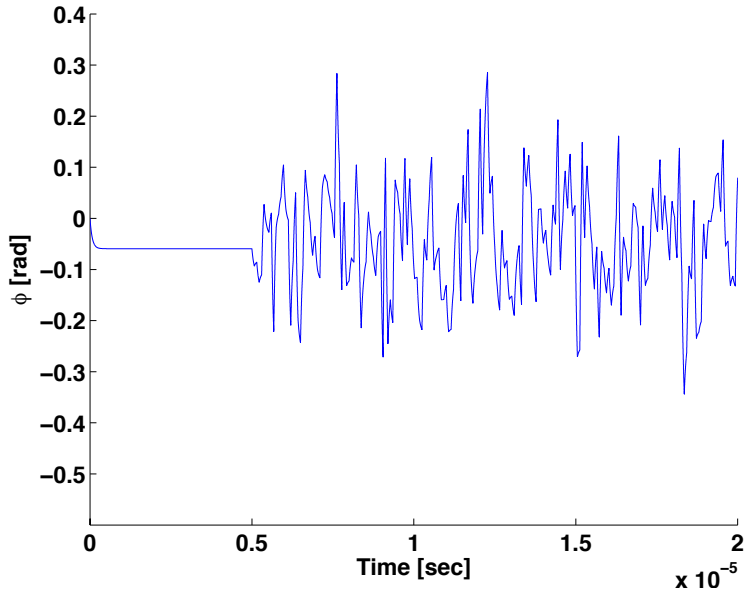

Figure 4.7: Phase with random frequency fluctuations shown in Fig. 4.6. The phase reaches a steady-state value of -0.0593 rad before the frequency fluctuations begin at $t = 5$ μs.

4.4 Effects of Random Noise on Peer-to-Peer Locked Magnetrons

Also of interest is the phase variation when the free-running frequencies contain a low frequency noise component. Figure. 4.6 shows a random sample of $(\Omega_2 - \Omega_1)$ which lies within the locking range. The numerical solution to Eq. (4.24) using this random sample is shown in Fig. 4.7. From this example, we see that the phase fluctuations do not exceed 0.3 rad.

The spectrum of the phase fluctuations in the presence of small random frequency fluctuation can be calculated analytically. Substituting Eqs. (4.20) into Eq. (4.24), we obtain

$$\frac{d\phi}{dt} + (\Omega_2 - \Omega_1) = \alpha_1 \sin(\bar{p} + \phi) - \alpha_2 \sin(\bar{p} - \phi). \tag{4.26}$$

Next, let us add a perturbation to the frequency such that $\Delta\Omega \equiv \Omega_2 - \Omega_1 = \Delta\Omega_m + \delta\Omega$

and $\phi = \phi_0 + \delta\phi$, where $\Delta\Omega_m$ is the mean difference in frequencies, $\delta\Omega$ is the random fluctuation, ϕ_0 is the unperturbed phase, and $\delta\phi$ is the perturbed phase caused by the perturbation in the frequency. Substituting this into Eq. (4.26) yields

$$\frac{d}{dt}\left(\phi_0 + \delta\phi\right) + \Delta\Omega_m + \delta\Omega = \alpha_1 \sin(\bar{p} + \phi_0 + \delta\phi) - \alpha_2 \sin(\bar{p} - \phi_0 - \delta\phi). \tag{4.27}$$

For small $\delta\Omega$ and $\delta\phi$, Eq. (4.27) is linearized to give

$$\frac{d\delta\phi}{dt} + \delta\Omega = \alpha_1 \delta\phi \cos(\bar{p} + \phi_0) + \alpha_2 \delta\phi \cos(\bar{p} - \phi_0). \tag{4.28}$$

Taking the Fourier transform of Eq. (4.28) yields

$$\widetilde{\delta\phi}(\omega) = \frac{\widetilde{\delta\Omega}(\omega)}{[\alpha_1 \cos(\bar{p} + \phi_0) + \alpha_2 \cos(\bar{p} - \phi_0)] - i\omega}, \tag{4.29}$$

where $\widetilde{\delta\phi}(\omega)$ and $\widetilde{\delta\Omega}(\omega)$ are, respectively, the Fourier transforms of $\delta\phi$ and $\delta\Omega$. The spectral density of the phase noise can then be related to the spectral density of the frequency fluctuations,

$$\left|\widetilde{\delta\phi}(\omega)\right|^2 = \frac{\left|\widetilde{\delta\Omega}(\omega)\right|^2}{\left[\alpha_1 \cos(\bar{p} + \phi_0) + \alpha_2 \cos(\bar{p} - \phi_0)\right]^2 + \omega^2}. \tag{4.30}$$

When locking is nearly satisfied, the term $\left[\alpha_1 \cos(\bar{p} + \phi_0) + \alpha_2 \cos(\bar{p} - \phi_0)\right]^2$ becomes much less than ω^2. Eq (4.30) can then be approximated as

$$\left|\widetilde{\delta\phi}(\omega)\right| \approx \frac{\left|\widetilde{\delta\Omega}(\omega)\right|}{\omega}. \tag{4.31}$$

Figure 4.8 shows the LHS and the RHS of Eq. (4.31) as a function of frequency, ω. The LHS is calculated by numerically taking the fast Fourier transform of $\phi(t)$; the RHS is calculated by numerically taking the fast Fourier transform of $\Delta\Omega(t)$ and

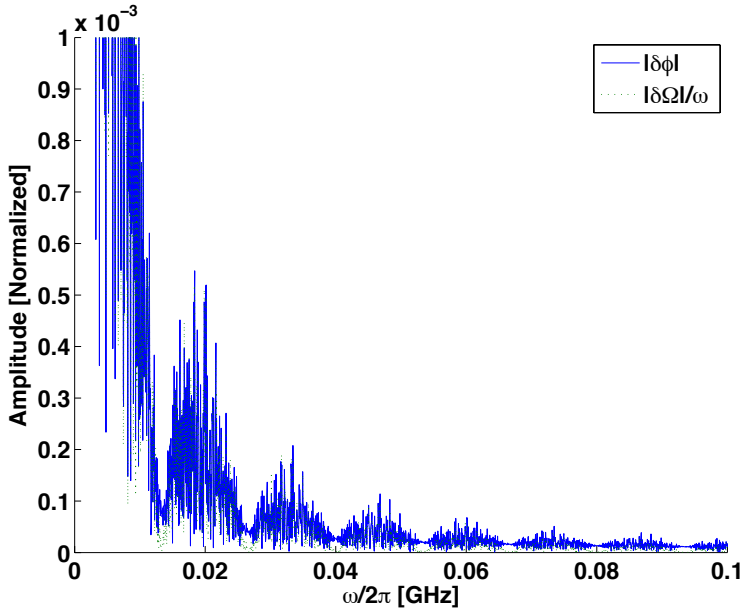

Figure 4.8: Numerical evaluation and comparison of the LHS and RHS of Eq. (4.31).

dividing by ω. The signals are noisy when they are close to $\omega = 0$. Both sides of Eq. (4.31) seem to show agreement. Figure 4.9 shows a zoomed view of the same plot around 35 MHz. The two curves can be seen to have similar shape to them and show reasonable agreement.

4.5 Extension of Temporal Locking to Spatial Locking of Nonlinear Modes

This section considers phase locking of spatial modes on wire z-pinches. As an intense current passes through the metallic wire, it heats it up such that the wire evolves into a hot liquid and vapor metal core with a surrounding, coronal plasma. Sausage-like modes are prevalent on each of the ablated wires (Fig. 1.3). When the wires are sufficiently close to each other, correlation between the ablation structures of neighboring wires can be observed [25, 86–88], as shown in Figs. 4.10 and 4.11. Figure 4.10 shows that when two wires are close by, the sausage-like modes are phase locked spatially. When the wires are far apart, no correlation of the phase is observed

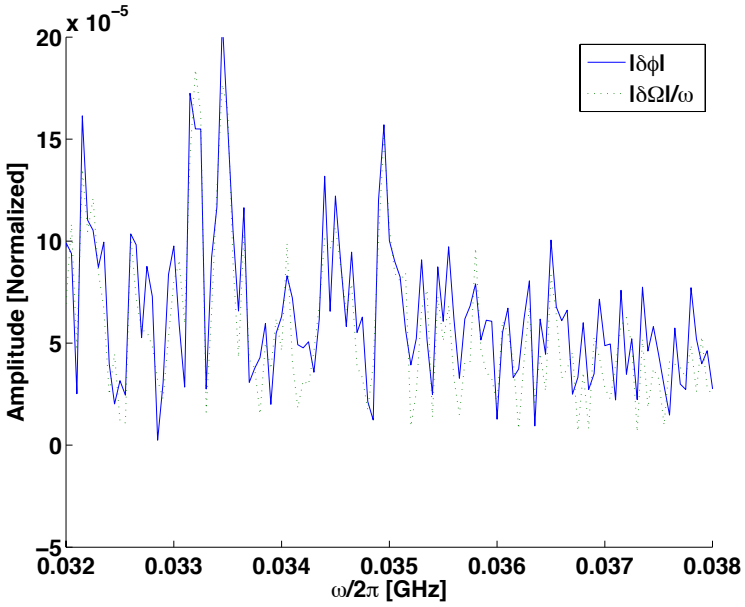

Figure 4.9: A zoomed view of Fig. 4.8 around 35 MHz.

in the sausage-like modes (Fig. 4.11).

We now apply the technique of temporal locking in (ω, t) domain to spatial locking in (k, z) domain. An isolated wire is known to develop a sausage like instability which manifests as axial variations in the form Se^{ikz-jp} where S is the amplitude, k is the axial (z) wave number, and p is the phase of the perturbation of the ablated plasma boundary [91, 92]. S is analogous to the amplitude (V) and k is analogous to the frequency (ω) of the free-running magnetron oscillation mode. Referring to Eqs. (4.23a) and (4.23b), we postulate that the governing equations for the phases p_1 and p_2 may be written as

$$\frac{dp_1}{dz} + k_1 - k = \beta_1 \sin(q_{12} + p_2 - p_1), \tag{4.32}$$

$$\frac{dp_2}{dz} + k_2 - k = \beta_2 \sin(q_{21} + p_1 - p_2), \tag{4.33}$$

where k_1 (k_2) is the axial wave number on wire 1 (wire 2) when the other is infinitely far away, β_1 (β_2) is the effect on wire 1 (wire 2) by wire 2 (wire 1); *both* β_1 *and* β_2

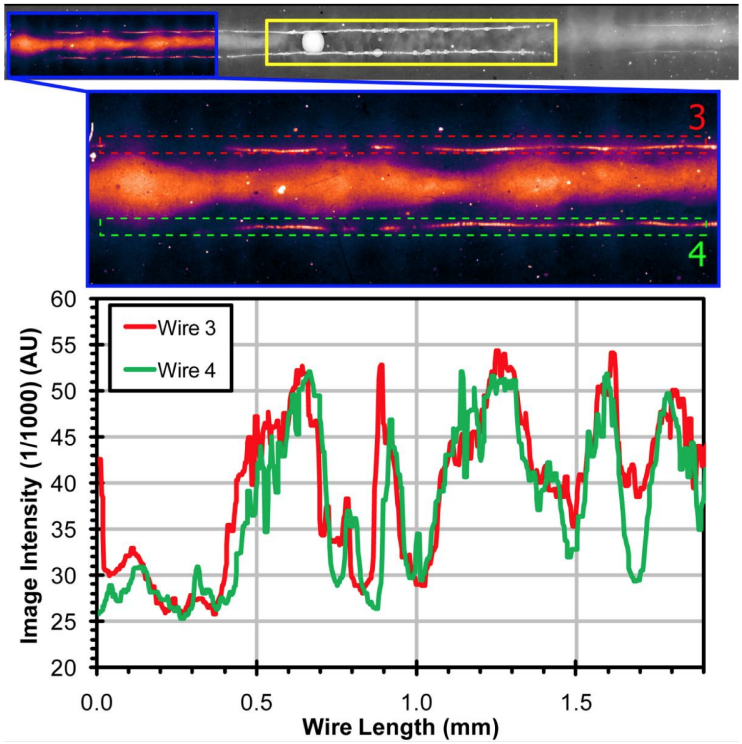

Figure 4.10: A false color radiograph with enhanced contrast (top) from a small interwire spacing shot. The tungsten wires are 7.4 μm in diameter and spaced 240 μm apart. This particular shot occurred at 93 ns and there was 1.13 MA of driver current. The corresponding lineouts (bottom) of the two wires shows the ablation correlation between them. Figure from [25].

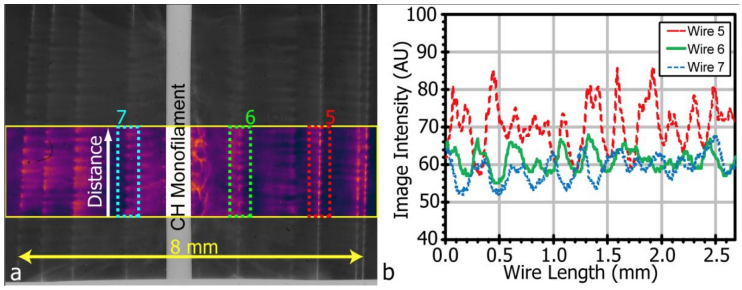

Figure 4.11: (a) An enhanced contrast radiograph taken by the COBRA-STAR imaging system of ten tungsten wires with large interwire gap spacing with 7.4 μm diameters at 100 ns in time with 1.0 MA of drive current. (b) The corresponding lineouts from wires highlighted in the radiograph. Figure from [25].

become small when the wire separation becomes large, and q_{12} and q_{21} is another pair of constants associated with the coupling between the two wires. Thus, analogous to Eq. (4.22), we arrive at the locking condition for the phase p_1 and p_2 on the two wires,

$$\beta_1^2 + \beta_2^2 + 2\beta_1\beta_2 \cos(q_{12} + q_{21}) > (k_2 - k_1)^2. \tag{4.34}$$

Equation (4.34) implies that phase locking can be achieved only if the wires are sufficiently close to each other. In the case of the experiments of Zier et al. [25], locking was observed when the wires were 240 μm apart. This is quite analogous to Huygen's original observation that synchronization of two clocks occurred only if the two clocks were placed sufficiently close to each other [76]. While the physical processes that lead to spatial locking for the two ablating wires can be quite complicated (just as the locking of Huygen's clocks), what we have given here is a framework in which spatial correlation may be interpreted in the same manner as temporal locking. The transform pair (ω, t) in the time domain is totally analogous to the transform pair (k, z) in the spatial domain. The study presented in this chapter of lockability when ω has a finite width in the spectrum, e.g., frequency chirp or noise, such as those studied in Sections 4.3 and 4.4, can similarly be adapted to the wave number k in the spatial domain for nonmonochromatic k_1 and k_2.

4.6 Summary and Conclusions

In this chapter, the analytic condition for the peer-to-peer locking of two magnetrons was presented [53]. Using values from the experiments that validated the locking condition [54], the effects on the peer-to-peer locking condition in the presence of both a frequency chirp and low frequency random noise were investigated [26]. It is found that complete phase locking cannot be achieved in either case. It is found,

however, that as long as the locking condition is well satisfied instantaneously, a high degree of locking occurs.

Experiments performed by Zier et al., separate to these studies, investigated the spatial correlation of two current carrying wires that are placed sufficiently close together [24, 25]. When the two wires are sufficiently far apart and pulsed with $10\text{s} - 100\text{s}$ of kiloamperes of current the plasma density from the ablated wires is uncorrelated between the two. In the case where the two wires are ablated in sufficiently close proximity, the density perturbations are correlated spatially. An argument is made that the analysis performed in the time domain can be adapted to this locking in the spatial domain, providing a framework for the interpretation of these experiments by Zier et al.

CHAPTER 5

Conclusions and Future Work

This thesis contains analysis of the effects of random perturbations, due to manufacturing processes or noise, on two microwave sources: the traveling wave tube and the magnetron. The investigation of these effects was motivated, respectively, by the desire to push microwave sources in the millimeter and sub-millimeter wavelength regime, and by the appeal of generating high power microwaves from the peer-to-peer locking of highly efficient, lower power magnetrons.

5.1 Investigation of Random Errors in TWTs

In Chapter 2, the effects on the gain and the phase of TWTs in the presence of random manufacturing methods were investigated using the traditional three wave model. This work was motivated by a peculiar feature in previous numerical studies that reported a significant number of simulated TWTs that showed higher gain in the presence of random errors compared to the error free case [32]. In this study we presented two analytic formulations, the perturbation and Riccati analysis [34]. These analytic formulas showed that the mean variation in the gain and phase is a small, second order effect in the standard deviation of the errors, σ_b. It was found that the analytic formulations showed reasonable agreement with the numeric methods over a wide range of parameter space when the space charge effect (QC) is neglected.

The analysis was then extended to account for the inclusion of a nonzero QC term. It was found that in the presence of the QC term the perturbation analysis and the Riccati analysis no longer accurately predicted the results of the numeric analysis. One possible explanation of this is that the space charge term reduces the range of b (the sensitive detune parameter in TWTs) over which gain occurs, if at all. This violates the single-wave assumption behind the Riccati approach but doesn't fully explain the difference with the perturbation method. This unanswered question about why the space charge term modifies the analytic results so much that they do not agree with direct numerical integration of the governing equation is worthy of future study.

The standard deviation is shown to be first order in σ_b while the mean variation is shown to be second order in σ_b in both analytic approaches (perturbation and Riccati). This causes the standard deviation to be larger than the mean variation, which statistically explains why a significant number of simulated TWTs can exhibit larger gain in the presence of errors. It also suggests that the $b(x)$ profile is not optimized. Preliminary results of the optimal $b(x)$, determined by the highest gain cases in one million samples, revealed an interesting feature. The profile in $b(x)$ exhibited a parabolic dip in the middle section of the profile, implying that the phase velocity of the circuit wave in the mid-section of the tube needs to be faster than the beam velocity for higher gain. This was particularly evident in cases with 3 to 8 error node segments. The feature is still evident in samples with up to 20 nodes but becomes much less prominent as the number of nodes increases to 100. The case with the $N = 5$ segment helix shows a 25% increase in gain. In the case of the microwave power module operating at 3-18 GHz, the 21.6 cm long circuit produces around 200 W of power. These results suggest that this MPM could produce an extra 50 W of power simply by varying the helix periodicity. The study of this optimization and of these optimized $b(x)$ profiles and their underlying physical nature is an interesting

area of future study.

In Chapter 3, the TWT analysis was extended by including the effects of the backward circuit wave. Due to the boundary conditions, this problem could no longer be solved using the forward integration method that was utilized in the three-wave model. A general method of solving this problem by solving for the mode amplitude in all segments in the presence of random errors was presented in [37]. This algorithm was numerically validated via the forward integration code originally developed for solving the three-wave problem (and modified to four-wave) and those validation results were presented. It confirmed that the effects of the internal reflections increased the mean variation and the standard deviation in the gain and phase in the presence of random errors compared to that of the model with only three-waves. The effects of random errors on a G-Band TWT were studied and shown to cause a ripple in the gain across the band.

During this four wave investigation, the question of internal reflections being the source of TWT oscillations arose. As this is a difficult question to analyze, we posed the simpler problem of investigating the absolute instability in a dielectric waveguide. Using the exact dispersion relation, the critical roots (ω_s, k_s) of the dispersion relation can be numerically solved for. The splitting of the double root k_s is then tested according to the Briggs-Bers criterion, which identifies the presence of absolute instability. Preliminary runs show that there is a threshold value of beam current beyond which the absolute instability occurs. How to apply absolute instability analysis to a practical TWT is an open question, because the dispersion relation cannot be obtained exactly. Our study of the dielectric waveguide suggests that cutoff oscillations (at $k_z = 0$) are worthy of particular attention.

5.2 Investigation of Locking of Nonlinear Oscillators

In Chapter 4, the phase locking of nonlinear oscillators is considered. First, the locking of two magnetrons is considered in the peer-to-peer configuration. This configuration differs from the standard "master-slave" configuration in that each oscillator acts as both master to and slave to the other. An analytic condition that describes the conditions under which peer-to-peer locking occurs was previously derived [53], and this condition was proved to be true experimentally [54]. In this thesis, we explore the question as to how the peer-to-peer locking of two magnetrons behaves in the presence of both a frequency chirp and low frequency noise [26]. In the presence of a low frequency chirp, it was found that the rate of change of the difference in phase between the two oscillators was greatly reduced but was not equal to zero when the peer-to-peer locking condition was satisfied. A high degree of locking can occur when the locking condition is satisfied in the presence of a frequency chirp, but complete phase locking cannot be achieved. Next, the presence of low frequency noise was investigated. Again, it was found that in the presence of low frequency noise complete locking cannot be achieved. It was found, however, that as long as the locking condition is well satisfied instantaneously, approximate locking occurs. In the case presented, the difference between the phases of both oscillators never exceeded 0.3 radians in the presence of noise.

Only the peer-to-peer locking of two oscillators has been considered. The peer-to-peer locking condition for three or more oscillators is a remaining problem that is open for future work. In the experiments that validated the peer-to-peer locking condition, it was found that the frequency of two peer-to-peer locked magnetrons did not necessarily lie between the two free running frequencies of the oscillators [54]. Due to the nature of the governing equations, there are two locking frequencies that can result from the peer-to-peer locking. The investigation of why one of these frequencies is more prevalent or stable than the other is still an open question for

future investigation.

Separate to the research performed on the peer-to-peer locking, experiments were performed that investigated the spatial correlation of the ablation structure of two current carrying wires [25]. It is well known that a current carrying wire will exhibit the sausage-like plasma instability. It was found that when two such wires were placed sufficiently close together that the ablation structure between the two becomes correlated spatially. As the wires are spaced further apart, the ablation plasma is no longer correlated spatially. We interpret this phenomenon as locking in the spatial domain. An argument is made that since the spatial locking is analogous to the temporal locking problem that the phase equations that govern the two ablating wires will be of the same form. From the phase equations for the wires, we formulate a locking condition for the spatial locking of two current carrying wires. We have provided a framework for the interpretation of spatial locking. We did not compare directly to experimental data or attempt to resolve what the coupling coefficients in our framework are. This will require an in-depth physical modeling of the complex physics of an ablated plasma from wires.

APPENDICES

APPENDIX A

Second-Order Small-Signal Solution in the Presence of Random Errors [34]

We derive the second-order perturbative solution to Eq. (2.13) when the Pierce parameters C and d are constant and the parameter b contains small random perturbations denoted as $b_1(x)$. We re-write Eq. (2.10) as,

$$a = a_0 e^{G_1 + j\theta_1}, \tag{A.1}$$

where a is the normalized electric field and $a_0(x)$ is the solution in the error-free tube given by Eq. (A4) of [32]. To second order, we write $a(x) = a_0(x) + a_{10}(x) + a_{11}(x)$. The first and second order perturbations are $a_{10}(x)$ and a_{11}, respectively. Expanding $a(x)$ in Eq. (A.1) yields an expression for the modification of amplitude and phase of

$$G_1 + j\theta_1 = \frac{a_{10} + a_{11}}{a_0} - \frac{1}{2}\frac{a_{10}^2}{a_0^2}. \tag{A.2}$$

This equation can be solved for the gain and phase change when the expressions for a_{10} and a_{11} are substituted into Eq. (A.2). These quantities are to be derived in this appendix.

Equation (2.8) can be written as three coupled first-order differential equations expressed in matrix notation as

$$\frac{d\mathbf{Y}}{dx} = (\mathbf{M} + \mathbf{M}_1)\,\mathbf{Y}, \tag{A.3}$$

in the presence of random variation $b_1(x)$, where $\mathbf{M}$ represents the error-free tube and $\mathbf{M}_1$ is the modification due to b_1,

$$\mathbf{M} = \begin{bmatrix} 0 & 1 & 0 \\ 0 & 0 & 1 \\ -jC\left(4QC^3\left(b - jd\right) + C^2\right) & 4QC^3 & -jC\left(b - jd\right) \end{bmatrix}, \tag{A.4}$$

$$\mathbf{M}_1 = \begin{bmatrix} 0 & 0 & 0 \\ 0 & 0 & 0 \\ m_{31}(x) & 0 & m_{33}(x) \end{bmatrix}, \tag{A.5}$$

where $m_{31} = -jC\left(4QC^3\right)b_1(x)$ and $m_{33} = -jCb_1(x)$. Equation (A.4) is a constant matrix containing error-free tube parameters. We assume that there are no losses, i.e., $d = 0$. We write

$$\mathbf{Y} = \mathbf{Y}_0(x) + \mathbf{Y}_1(x) \equiv \begin{bmatrix} f_0(x) + f_1(x) \\ v_0(x) + v_1(x) \\ a_0(x) + a_1(x) \end{bmatrix}, \tag{A.6}$$

where quantities with subscript 1 are due only to random $b_1(x)$. The error-free solutions are f_0, v_0, and a_0 and are given by Eq. (A4) of [32].

Combining Eq. (A.6) with (A.3) yields, to second order

$$\frac{d\mathbf{Y}_1}{dx} - \mathbf{M}\mathbf{Y}_1 = \mathbf{M}_1\mathbf{Y}_0 + \mathbf{M}_1\mathbf{Y}_1. \tag{A.7}$$

Ignoring the second order term $\mathbf{M}_1\mathbf{Y}_1$, the solution to Eq. (A.7) is $\mathbf{Y}_1(x) = \mathbf{Y}_{10}(x)$,

whose solution is given by Eq. (A10) of [32]. Next, let us approximate $\mathbf{M}_1\mathbf{Y}_1$ in Eq. (A.7) as $\mathbf{M}_1\mathbf{Y}_{10}(x)$, and write

$$\mathbf{Y}_1 = \mathbf{Y}_{10}(x) + \mathbf{Y}_{11} \equiv \begin{bmatrix} f_{10}(x) + f_{11}(x) \\ v_{10}(x) + v_{11}(x) \\ a_{10}(x) + a_{11}(x) \end{bmatrix}. \tag{A.8}$$

Equation (A.8) then becomes

$$\frac{d\mathbf{Y}_{11}(x)}{dx} - \mathbf{M}\mathbf{Y}_{11}(x) \cong \mathbf{M}_1(x)\mathbf{Y}_{10}(x), \tag{A.9}$$

which is of the same form as Eq. (A7) of [32].

We may then express $\mathbf{Y}_{11}$ as Eq. (A10) from [32] to obtain

$$a_{11}(x) = \int_0^x ds\ \left(m_{31}(s)f_{10}(s) + m_{33}(s)a_{10}(s)\right) P_3(x,s), \tag{A.10}$$

where

$$P_3(x,s) = \Psi_{31}(x)\Psi_{13}^{-1}(s) + \Psi_{32}(x)\Psi_{23}^{-1}(s) + \Psi_{33}(x)\Psi_{33}^{-1}(s), \tag{A.11}$$

and $\Psi_{ij}(x)$ $(i,j = 1,2,3)$ is defined by Eq. (A3) of Pengvanich et al. [32]. The first order perturbations $f_{10}(x)$ and $a_{10}(x)$ are given by Eq. (A11) of Pengvanich et al. [32], where the expression for $V_k(s)$ now contains the AC space charge term in $m_{31}(x)$. Substituting these into Eq. (A.10) yields

$$a_{11}(x) = \int_0^x ds\, P_3(x,s) \Bigg\{ \sum_{l=1}^{3} \frac{\tau_l}{C\delta_l} e^{C\delta_l s} \int_0^s ds'\, e^{-C\delta_l s'} \big[f_0(s') m_{31}(s') m_{31}(s) + a_0(s') m_{33}(s') m_{31}(s) \big] + \sum_{k=1}^{3} \tau_k C\delta_k e^{C\delta_k s} \int_0^s ds'\, e^{-C\delta_k s'} \times \big[f_0(s') m_{31}(s') m_{33}(s) + a_0(s') m_{33}(s') m_{33}(s) \big] \Bigg\} \tag{A.12}$$

where $\delta_k (k = 1, 2, 3)$ are the three roots to the Pierce dispersion relation (2.7), and $\tau_k (k = 1, 2, 3)$ which depends only on δ_k, is defined by Eq. (A5) of Ref. [32].

We next take the ensemble average of Eq. (A.12), assuming that $\langle b_1(s) b_1(s') \rangle = \langle b_1^2 \rangle \, \Delta \delta(s - s')$, where Δ is the correlation length and δ is the Dirac delta function. With $\langle b_1^2 \rangle = \sigma_b^2$, we obtain

$$\langle a_{11}(x) \rangle = \int_0^x ds\, P_3(x,s) \Bigg\{ - C^2 \sigma_b^2 \Delta \left(4QC^3 \right) \sum_{l=1}^{3} \frac{\tau_l}{C\delta_l} \left[4QC^3 \frac{f_0(s)}{2} + \frac{a_0(s)}{2} \right] - C^2 \sigma_b^2 \Delta \sum_{k=1}^{3} \tau_k C\delta_k \left[4QC^3 \frac{f_0(s)}{2} + \frac{a_0(s)}{2} \right] \Bigg\}. \tag{A.13}$$

Similarly, squaring $a_{10}(x)$ and taking the ensemble average yields

$$\left\langle a_{10}^2(x) \right\rangle = -C^2 \sigma_b^2 \Delta \sum_{k=1}^{3} \sum_{l=1}^{3} \left(\tau_k C\delta_k \right) \left(\tau_l C\delta_l \right) e^{C(\delta_k + \delta_l)x} \int_0^x ds\, e^{-C(\delta_k + \delta_l)s} \times \left[\left(4QC^3 \right)^2 f_0^2(s) + 2 \left(4QC^3 \right) f_0(s) a_0(s) + a_0^2(s) \right]. \tag{A.14}$$

Note that $\langle a_{10}(x) \rangle = 0$ since $\mathbf{M}_1$ is linear in $b_1(x)$ and therefore $\langle \mathbf{Y}_{10}(x) \rangle = 0$ (cf. Eq. (A10) of [32]).

With this result, we obtain from Eq. (A.2),

$$\langle G_1(x) + j\theta_1(x)\rangle = \frac{\langle a_{11}(s)\rangle}{a_0(x)} - \frac{1}{2}\frac{\langle a_{10}^2\rangle}{a_0^2(x)}, \tag{A.15}$$

where $\langle a_{11}(x)\rangle$ is given by Eq. (A.13), $a_0(x)$ by Eq. (A4) of [32], and $\langle a_{10}^2(x)\rangle$ by Eq. (A.14). This can be written in the form

$$\langle G_1(x) + j\theta_1(x)\rangle = -\frac{1}{2}C^2\sigma_b^2\Delta\Bigg\{\left[4QC^3\sum_{l=1}^{3}\frac{\tau_l}{C\delta_l} + \sum_{k=1}^{3}\tau_k C\delta_k\right]\int_0^x \frac{Q_1(x,s)ds}{a_0(x)} + \sum_{l=1}^{3}\sum_{k=1}^{3}\left(\tau_l C\delta_l\right)\left(\tau_k C\delta_k\right)e^{C(\delta_l+\delta_k)x}\int_0^x \frac{Q_2(x,s)ds}{a_0^2(x)}\Bigg\}, \tag{A.16}$$

which is Eq. (2.13) in chapter 2. In Eq. (A.16), $Q_1(x,s)$, $Q_2(x,s)$ are given by, with the substitution $\lambda_i = C\delta_i$,

$$Q_1(x,s) = \Bigg\{\left[\lambda_1^2\left(\lambda_2-\lambda_3\right)e^{\lambda_1(x-s)} + \lambda_2^2\left(\lambda_1-\lambda_3\right)e^{\lambda_2(x-s)} + \lambda_3^2\left(\lambda_1-\lambda_2\right)e^{\lambda_3(x-s)}\right]\times \left[\sum_{i=1}^{3}\lambda_i\tau_i e^{\lambda_i s} + 4QC^3\sum_{j=1}^{3}\frac{\tau_j}{\lambda_j}e^{\lambda_j s}\right]\Bigg\}\Bigg/\left[\left(\lambda_1-\lambda_2\right)\left(\lambda_1-\lambda_3\right)\left(\lambda_2-\lambda_3\right)\right], \tag{A.17}$$

$$Q_2(x,s) = \left(\frac{1}{\lambda_1\lambda_2\lambda_3}\right)^2 e^{-(\lambda_k+\lambda_l)}\big[\tau_1\lambda_2\lambda_3\left(4QC^3+\lambda_1^2\right)e^{\lambda_1 s} + \tau_2\lambda_1\lambda_3\left(4QC^3+\lambda_2^2\right)e^{\lambda_2 s} + \tau_3\lambda_1\lambda_2\left(4QC^3+\lambda_3^2\right)e^{\lambda_3 s}\big]. \tag{A.18}$$

In the limit of zero space charge effects, Eq. (A.16) reduces to

$$\langle G_1(x) + j\theta_1(x)\rangle = \frac{1}{2}C^2\sigma_b^2\Delta\int_0^x ds\, A(x,s), \tag{A.19}$$

where

$$A(x,s) = \sum_{j=1}^{3} \tau_j C\delta_j P_3(x,s)\frac{a_0(s)}{a_0(x)} + \sum_{k=1}^{3}\sum_{l=1}^{3} \left(\tau_k C\delta_k\right)\left(\tau_l C\delta_l\right) e^{C(\delta_k+\delta_l)x} e^{-C(\delta_k+\delta_l)s} \frac{a_0^2(x)}{a_0^2(x)}. \tag{A.20}$$

APPENDIX B

Derivation of the Exact Smooth, Dielectric Waveguide Dispersion Relation

The exact dispersion relation of an electron sheet-beam propagating through a dielectric waveguide can be determined [66]. We begin by considering an electron sheet-beam propagating through a smooth wave guide, as shown in Fig. B.1. Assume an infinite magnetic field in the direction of propagation, $\hat{z}$. In general, we assume that the electron sheet-beam has some small finite thickness, τ. The equilibrium conditions are

$$\vec{v} = \hat{z}v_0, \tag{B.1a}$$

$$\rho_0 = \sigma_0\delta(x-a), \tag{B.1b}$$

and

$$J_0 = K_0 v_0 \delta(x-a), \tag{B.1c}$$

where v_0 is the constant beam velocity, ρ_0 is the charge density, $\sigma_0 = \tau\rho_0$ is the surface charge density, $K_0 = J_0\tau$ is the surface current, and δ is the Dirac delta function. Let us consider an infinitesimally thin beam, such that $\tau \to 0$. We require that $\rho_0 \to \infty$,

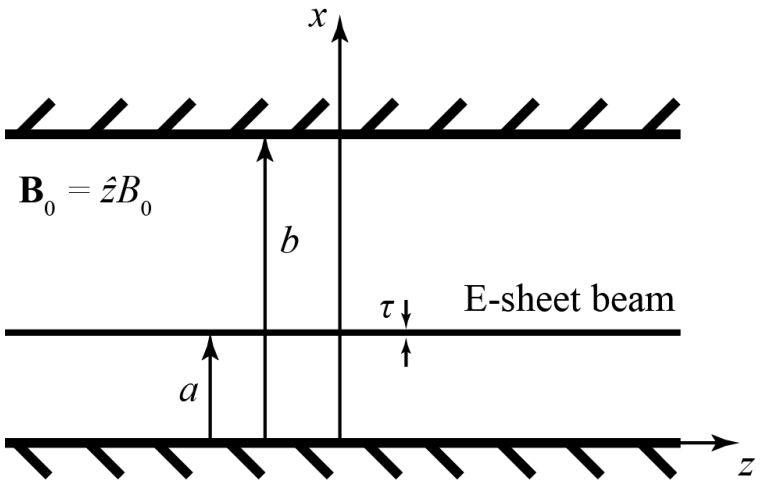

Figure B.1: An electron sheet beam with thickness τ propagating through a dielectric waveguide in the $\hat{z}$-direction along an infinite magnetic field.

such that σ_0 and K_0 remain finite. Introducing a perturbation to this system of the form $e^{j\omega t - jk_z z}$ where the subscript 0 denotes the unperturbed quantities while the subscript 1 denotes the perturbation quantities, the velocity and density are now of the form

$$v = v_0 + v_1 e^{j\omega t - jk_z z}, \tag{B.2}$$

$$n = n_0 + n_1(x) e^{j\omega t - jk_z z}. \tag{B.3}$$

This results in bunching of the electron beam. The perturbation electric field is of the form

$$E = \left[\hat{x}E_{1x}(x) + \hat{z}E_{1z}(x)\right] e^{j\omega t - jk_z z}. \tag{B.4}$$

Using Faraday's law we can compute the perturbation magnetic field

$$\nabla \times \vec{E} = -\mu_0 \frac{\partial \vec{H}}{\partial t} = -j\omega\mu_0 \vec{H}, \tag{B.5}$$

and show that it is of the form

$$\vec{H}_1 = \hat{y} H_{1y}(x) e^{j\omega t - jk_z z}. \tag{B.6}$$

First, the response of the beam to these perturbation fields must be calculated. The force law reads

$$\frac{\partial \vec{v}}{\partial t} + \vec{v} \cdot \nabla \vec{v} = \frac{e}{m_e} \left[\vec{E} + \vec{v} \times \vec{B} \right], \tag{B.7}$$

where e is the electronic charge and m_e is the electron rest mass. Only the force law in the $\hat{z}$-direction needs to be considered since infinite magnetic field has been assumed to be infinite in that direction, restricting motion in the $\hat{z}$-direction. Equation (B.7) will be linearized; that is only terms that are first order in perturbation quantities are kept. Substituting Eq. (B.2) into (B.7) and evaluating the derivatives yields

$$j\omega v_1 - jk_z z v_0 v_1 = \frac{e}{m_e} E_{1z}, \tag{B.8}$$

which can be solved for v_1,

$$v_1 = -\frac{je}{(\omega - k_z v_0) m_e} E_{1z}. \tag{B.9}$$

The continuity equation reads

$$\frac{\partial n}{\partial t} + \nabla \cdot (nv) = 0. \tag{B.10}$$

Substituting the perturbation velocity and density (Eqs. (B.2) and (B.3)) into Eq. (B.10) and linearizing yields

$$n_1 = \frac{k_z n_0}{(\omega - k_z v_0)} v_1. \tag{B.11}$$

Substituting the expression for v_1, Eq. (B.9), into Eq. (B.11) yields

$$n_1 = \frac{-jk_z n_0 e}{m_e(\omega - k_z v_0)^2} E_{1z}. \tag{B.12}$$

This expression for n_1 can be used to calculate the perturbation surface charge density, $\sigma_1 = e n_1 \tau$, at the location of the beam, $x = a$. It reads

$$\sigma_1 = \frac{-je^2 k_z (n_0 \tau)}{m_e(\omega - k_z v_0)^2} E_{1z}(x = a). \tag{B.13}$$

Using the normalized continuity equation, Eq. (B.13) can be used to express the perturbation current as

$$J_1 = \frac{\omega}{\tau k_z} \sigma_1. \tag{B.14}$$

The next step is to calculate the perturbation fields that are excited by the perturbations in the beam. Specifically, by solving for $E_{1z}(x = a)$ the dispersion relation can be solved for by way of Eq. (B.14).

There are two distinct regions to consider when calculating the fields: Region I ($0 < x < a^-$) and Region II ($a^+ < x < b$). In the vacuum region, Faraday's and Ampère's Laws read

$$\nabla \times \vec{E_1} = -j\omega\mu_0 \vec{H_1} \tag{B.15}$$

$$\nabla \times \vec{H_1} = j\omega\epsilon_0 \vec{E_1}. \tag{B.16}$$

Taking the curl of Eq. (B.16) and substituting $\nabla \cdot \vec{H_1} = 0$ yields

$$\left(\frac{\omega^2}{c^2} + \nabla^2\right) \vec{H_1} = 0. \tag{B.17}$$

It is the TM mode that is set up in this geometry. By substituting Eq. (B.6) into

Eq. (B.17), it can be shown that

$$\frac{\partial^2 H_{1y}}{\partial x^2} + \left(\frac{\omega^2}{c^2} - k_z^2\right) H_{1y} = 0. \tag{B.18}$$

Let

$$p^2 \equiv \frac{\omega^2}{c^2} - k_z^2 \tag{B.19}$$

be a constant such that Eq. (B.18) reads as

$$\frac{\partial^2 H_{1y}}{\partial x^2} + p^2 H_{1y} = 0. \tag{B.20}$$

The solution to Eq. (B.20) is known [93]. In regions I and II,

$$H_{1y} = \begin{cases} A_I \cos\left[p(x - C_I)\right], & 0 < x < a^- \\ A_{II} \cos\left[p(x - C_{II})\right], & a^+ < x < b \end{cases}. \tag{B.21}$$

The vacuum electric field can then be solved for by substituting Eq. (B.21) into Eq. (B.16) to show that

$$\vec{E_1} = \frac{1}{j\omega\epsilon_0} \begin{cases} \left[\hat{x}\left(jk_z A_I \cos\left[p(x - C_I)\right]\right) - \hat{z}\left(A_I p \sin\left[p(x - C_I)\right]\right)\right], & 0 < x < a^- \\ \left[\hat{x}\left(jk_z A_{II} \cos\left[p(x - C_{II})\right]\right) - \hat{z}\left(A_{II} p \sin\left[p(x - C_{II})\right]\right)\right], & a^+ < x < b \end{cases} \tag{B.22}$$

There are four unknowns in Eqs. (B.21) and (B.22); A_I, A_{II}, C_I, and C_{II}. We require four boundary conditions, i.e., four equations, to solve for these coefficients. The boundary conditions for this system are that $\vec{E_1}$ must be normal at the bottom ($x = 0$) and at the top ($x = b$) of the waveguide (Fig. B.1), the tangential electric field is continuous at the beam ($x = a$), and the normal electric field is discontinuous

across the beam because of its sheet charge perturbation. These boundary conditions give us the following four equations:

$$E_{1z}(x=0)=0, \tag{B.23a}$$

$$E_{1z}(x=b)=0, \tag{B.23b}$$

$$E_{1z}(x=a^{+})=E_{1z}(x=a^{-}), \tag{B.23c}$$

$$E_{1x}(x=a^{+})-E_{1x}(x=a^{-})=\frac{\sigma_1}{\epsilon}. \tag{B.23d}$$

Equations (B.23) can be used to solve for the coefficients A_I, A_{II}, C_I, and C_{II} in terms of $E_{1z}(x=a)$. Equations (B.23a) and (B.23b) can be used to show that $C_I=0$ and $C_{II}=b$. Solving Eqs. (B.23c) and (B.23d) gives solution to A_I and A_{II}. After some algebra, it can be shown that axial electric field at the location of the beam is given by

$$E_{1z}(x=a)=\frac{J_1}{j\omega\epsilon_0}\left(\frac{\tau}{b}\right)Z(\omega,k_z), \tag{B.24}$$

where $Z(\omega,k_z)$ is known as the interaction impedance and is defined as

$$Z(\omega,k_z)=\frac{-pb\sin(pa)\sin[p(b-a)]}{\sin(pb)}. \tag{B.25}$$

Substituting Eq. (B.25) into the expression for the perturbation current, J_1, Eq. (B.14), yields the dispersion relation for a beam in a dielectric waveguide. The dispersion relation reads

$$(\omega-k_z v_0)^2=\omega_p^2\left(\frac{\tau}{b}\right)Z(\omega,k_z) \tag{B.26}$$

where $\omega_p=\sqrt{e^2n_0/m_e\epsilon}$ is the plasma frequency. We express Eq. (B.26) as

$$D(\omega, k_z) \equiv (\omega - k_z v_0)^2 - \omega_p^2 \left(\frac{\tau}{b}\right) Z(\omega, k_z) = 0. \tag{B.27}$$

Assuming $b = 2a$, Eqs. (B.25) and (B.27) yields Eq. (3.8) of the main text.

BIBLIOGRAPHY

BIBLIOGRAPHY

[1] A. S. Gilmour, *Microwave Tubes*. Norwood, MA: Artech House, 1986.

[2] R. J. Barker, J. H. Booske, N. C. Luhmann Jr., and G. S. Nusinovich, *Modern Microwave and Millimeter-Wave Power Electronics*. Piscataway, NJ: IEEE Press, 2005.

[3] V. Granatstein, R. Parker, and C. Armstrong, "Vacuum electronics at the dawn of the twenty-first century," *Proceedings of the IEEE*, vol. 87, no. 5, pp. 702–716, May 1999.

[4] J. H. Booske, "Plasma physics and related challenges of millimeter-wave-to-terahertz and high power microwave generation," *Physics of Plasmas*, vol. 15, no. 5, pp. 055 502–1–055 502–16, May 2008.

[5] C. Smith, C. Armstrong, and J. Duthie, "The microwave power module: A versatile RF building block for high-power transmitters," *Proceedings of the IEEE*, vol. 87, no. 5, pp. 717–737, May 1999.

[6] D. Whaley, C. Armstrong, B. Gannon, G. Groshart, E. Hurt, J. Hutchins, M. Roscoe, T. Antonsen, and B. Levush, "Sixty-percent-efficient miniature C-Band vacuum power booster for the microwave power module," *IEEE Transactions on Plasma Science*, vol. 26, no. 3, pp. 912–921, Jun 1998.

[7] A. A. Faust, C. J. J. de Ruiter, A. Ehlerding, J. E. McFee, E. Svinsas, and A. D. van Rheenen, "Observations on Military Exploitation of Explosives Detection Technologies," in *Detection and Sensing of Mines, Explosive Objects, and Obscured Targets XVI*, ser. Proceedings of SPIE, Harmon, RS and Holloway, JH and Broach, JT, Ed., vol. 8017, 2011, pp. 801 716–1–801 716–12.

[8] J. Tucek, D. A. Basten, D. A. Gallagher, and K. E. Kreischer, "Testing of a 0.850 THz vacuum electronic power amplifier," in *2013 IEEE International Vacuum Electronics Conference*, ser. IEEE International Vacuum Electronics Conference IVEC. IEEE Electron Devices Soc, 2013, pp. 1–2, 14th IEEE International Vacuum Electronics Conference, Paris, France, May 21-23, 2013.

[9] R. M. Gilgenbach, Y. Y. Lau, H. McDowell, K. L. Cartwright, and T. A. Spencer, "Crossed-field devices," in *Modern Microwave and Millimeter Wave Power Electronics*, R. J. Barker, J. H. Booske, N. C. Luhmann Jr., and G. S. Nusinovich, Eds. Piscataway, NJ: IEEE Press, 2005, pp. 289 – 342.

[10] J. Benford, J. A. Swegle, and E. Schamiloglu, *High Power Microwave Sources*. London: Taylor & Francis, 2007.

[11] V. Neculaes, R. Gilgenbach, and Y. Lau, "Low-noise microwave magnetrons by azimuthally varying axial magnetic field," *Applied Physics Letters*, vol. 83, no. 10, pp. 1938–1940, Sep 8 2003.

[12] D. G. Youmans, "Phase Locking of Adjacent Channel Leaky Waveguide CO2-Lasers," *Applied Physics Letters*, vol. 44, no. 4, pp. 365–367, 1984.

[13] R. Kompfner, "The Traveling-Wave Tube as Amplifier at Microwaves," *Proceedings of the Institute of Radio Engineers*, vol. 35, no. 2, pp. 124–127, 1947.

[14] J. R. Pierce, *Traveling Wave Tubes*. New York: Van Nostrand, 1950.

[15] S. Riyopoulos, "Magnetron theory," *Physics of Plasmas*, vol. 3, no. 3, pp. 1137–1161, Mar 1996.

[16] Y. Y. Lau, J. W. Luginsland, K. L. Cartwright, D. H. Simon, W. Tang, B. W. Hoff, and R. M. Gilgenbach, "A re-examination of the Buneman-Hartree condition in a cylindrical smooth-bore relativistic magnetron," *Physics of Plasmas*, vol. 17, no. 3, pp. 033 102–1–033 102–9, Mar 2010.

[17] J. Benford, "Relativistic magnetrons," in *High Power Microwave Sources*, V. L. Granatstein and I. Alexeff, Eds. Boston: Artech House, 1987, p. 351.

[18] G. Chandler, C. Deeney, M. Cuneo, D. Fehl, J. McGurn, R. Spielman, J. Torres, J. McKenney, J. Mills, and K. Struve, "Filtered x-ray diode diagnostics fielded on the Z accelerator for source power measurements," *Review of Scientific Instruments*, vol. 70, no. 1, 2, pp. 561–565, Jan 1999.

[19] C. A. Coverdale, B. Jones, D. J. Ampleford, J. Chittenden, C. Jennings, J. W. Thornhill, J. P. Apruzese, R. W. Clark, K. G. Whitney, A. Dasgupta, J. Davis, J. Guiliani, P. D. LePell, C. Deeney, D. B. Sinars, and M. E. Cuneo, "K-shell X-ray sources at the Z Accelerator," *High Energy Density Physics*, vol. 6, no. 2, SI, pp. 143–152, Jun 2010, 2nd International Conference on High Energy Density Physics, Austin, TX, May 19-22, 2009.

[20] M. G. Mazarakis, C. E. Deeney, W. A. Stygar, M. R. Douglas, J. Chittenden, D. B. Sinars, M. E. Cuneo, T. J. Nash, G. A. Chandler, M. K. Matzen, J. L. Porter, K. W. Struve, and D. H. McDaniel, "Wire number dependence of the implosion dynamics, stagnation, and radiation output of tungsten wire arrays at Z driver," *Physics of Plasmas*, vol. 18, no. 11, pp. 112 706–1–112 706–15, Nov 2011.

[21] P. M. Bellen, "Stability of static mhd equilibria," in *Fundamentals of Plasma Physics*. New York: Cambridge University Press, 2006, pp. 370 – 383.

[22] M. G. Mazarakis, M. E. Cuneo, W. A. Stygar, H. C. Harjes, D. B. Sinars, B. M. Jones, C. Deeney, E. M. Waisman, T. J. Nash, K. W. Struve, and D. H. McDaniel, "X-ray emission current scaling experiments for compact single-tungsten-wire arrays at 80-nanosecond implosion times," *Physical Review E*, vol. 79, no. 1, pp. 016 412–1–016 412–15, Jan 2009.

[23] D. Ryutov, M. Derzon, and M. Matzen, "The physics of fast Z pinches," *Reviews of Modern Physics*, vol. 72, no. 1, pp. 167–223, Jan 2000.

[24] J. C. Zier, "Ablation dynamics and instabilities of metallic plasmas generated using mega-ampere-scale current drivers," Ph.D. dissertation, University of Michigan, 2011.

[25] J. C. Zier, J. D. Douglass, I. C. Blesener, K. S. Blesener, D. A. Chalenski, R. M. Gilgenbach, J. B. Greenly, D. A. Hammer, P. F. Knapp, B. R. Kusse, Y. Y. Lau, R. D. McBride, W. Syed, and E. P. Yu, "Azimuthally correlated ablation between z-pinch wire cores," *Physics of Plasmas*, vol. 16, no. 10, pp. 102 702–1–102 702–6, Oct 2009.

[26] I. M. Rittersdorf, Y. Y. Lau, J. C. Zier, R. M. Gilgenbach, E. J. Cruz, and J. W. Luginsland, "Temporal and spatial locking of nonlinear systems," *Applied Physics Letters*, vol. 97, no. 17, pp. 171 502–1–171 502–3, Oct 25 2010.

[27] S. D'Agostino and C. Paoloni, "Effect of mechanical tolerance of T-shaped rods in a TWT based on a helix slow-wave structure," *Microwave and Optical Technology Letters*, vol. 25, no. 6, pp. 393–395, Jun 20 2000.

[28] S. D'Agostino, F. Emma, and C. Paoloni, "Sensitivity analysis of TWT's small signal gain based on the effect of rod shape and dimensions," *IEEE Transactions on Electron Devices*, vol. 47, no. 7, pp. 1457–1462, Jul 2000.

[29] S. D'Agostino and C. Paoloni, "Helix wire tolerances in TWT small-signal gain prediction," *Microwave and Optical Technology Letters*, vol. 29, no. 3, pp. 208–209, May 5 2001.

[30] S. D'Agostino and C. Paoloni, "A study on helix pitch tolerance impact on TWT small-signal gain," *IEEE Electron Device Letters*, vol. 23, no. 12, pp. 746–748, Dec 2002.

[31] J. D. Wilson and C. T. Chevalier, "Robust optimization of high-frequency traveling-wave tube slow-wave circuits," *IEEE Transactions on Electron Devices*, vol. 54, no. 5, pp. 1232–1237, May 2007.

[32] P. Pengvanich, D. Chernin, Y. Y. Lau, J. W. Luginsland, and R. M. Gilgenbach, "Effect of random circuit fabrication errors on small-signal gain and phase in traveling-wave tubes," *IEEE Transactions on Electron Devices*, vol. 55, no. 3, pp. 916–924, Mar 2008.

[33] P. Pengvanich, "Theory of injection locking and rapid start-up of magnetrons, and effects of manufacturing errors in terahertz traveling wave tubes," Ph.D. dissertation, University of Michigan, 2007.

[34] I. Rittersdorf, T. Antonsen, Jr., D. Chernin, and Y. Lau, "Effects of random circuit fabrication errors on the mean and standard deviation of small signal gain and phase of a traveling wave tube," *IEEE Journal of the Electron Devices Society*, vol. 1, no. 5, pp. 117–128, 2013.

[35] S. Sengele, M. L. Barsanti, T. A. Hargreaves, C. M. Armstrong, J. H. Booske, and Y. Y. Lau, "Impact of Random Fabrication Errors on Fundamental Forward-Wave Small-Signal Gain and Bandwidth in Traveling-Wave Tubes With Finite-Space-Charge Electron Beams," *IEEE Transactions on Electron Devices*, vol. 60, no. 3, pp. 1221–1227, Mar 2013.

[36] S. Sengele, M. L. Barsanti, T. A. Hargreaves, C. M. Armstrong, J. H. Booske, and Y. Y. Lau, "Impact of random fabrication errors on backward-wave small-signal gain in traveling wave tubes with finite space charge electron beams," *Journal of Applied Physics*, vol. 113, no. 7, pp. 074 905–1–074 905–9, Feb 21 2013.

[37] D. Chernin, I. Rittersdorf, Y. Y. Lau, T. M. Antonsen, Jr., and B. Levush, "Effects of multiple internal reflections on the small-signal gain and phase of a twt," *IEEE Transactions on Electron Devices*, vol. 59, no. 5, pp. 1542–1550, May 2012.

[38] D. Price, H. Sze, and D. Fittinghoff, "Phase and Frequency Locking of a Cavity Vircator Driven by a Relativistic Magnetron," *Journal of Applied Physics*, vol. 65, no. 12, pp. 5185–5189, Jun 15 1989.

[39] D. Price and H. M. Sze, "Phase-Stability Analysis of the Magnetron-Driven Vircator Experiment," *IEEE Transactions on Plasma Science*, vol. 18, no. 3, pp. 580–585, Jun 1990.

[40] W. Woo, J. Benford, D. Fittinghoff, B. Harteneck, D. Price, R. Smith, and H. Sze, "Phase Locking of High-Power Microwave-Oscillators," *Journal of Applied Physics*, vol. 65, no. 2, pp. 861–866, Jan 15 1989.

[41] J. Benford, H. Sze, W. Woo, R. Smith, and B. Harteneck, "Phase Locking of Relativistic Magnetrons," *Physical Review Letters*, vol. 62, no. 8, pp. 969–971, Feb 20 1989.

[42] H. Sze, R. Smith, J. N. Benford, and B. D. Harteneck, "Phase-Locking of Strongly Coupled Relativistic Magnetrons," *IEEE Transactions on Electromagnetic Compatibility*, vol. 34, no. 3, 1, pp. 235–241, Aug 1992.

[43] H. Sze, D. Price, and B. Harteneck, "Phase Locking of 2 Strongly Couple Vircators," *Journal of Applied Physics*, vol. 67, no. 5, pp. 2278–2282, Mar 1 1990.

[44] W. White, R. Gilgenbach, M. Jones, V. Neculaes, Y. Lau, P. Pengvanich, N. Jordan, B. Hoff, R. Edgar, T. Spencer, and D. Price, "Radio frequency priming of a long-pulse relativistic magnetron," *IEEE Transactions on Plasma Science*, vol. 34, no. 3, 1, pp. 627–634, Jun 2006.

[45] R. Adler, "Study of Locking Phenomena in Oscillators," *Proceedings of the IEEE*, vol. 61, no. 10, pp. 1380–1385, 1973.

[46] M. Jones, V. Neculaes, Y. Lau, R. Gilgenbach, and W. White, "Cathode priming of a relativistic magnetron," *Applied Physics Letters*, vol. 85, no. 26, pp. 6332–6334, Dec 27 2004.

[47] M. Jones, V. Neculaes, Y. Lau, R. Gilgenbach, W. White, B. Hoff, and N. Jordan, "Magnetron priming by multiple cathodes," *Applied Physics Letters*, vol. 87, no. 8, Aug 22 2005.

[48] V. Neculaes, M. Jones, R. Gilgenbach, Y. Lau, J. Luginsland, B. Hoff, W. White, N. Jordan, P. Pengvanich, Y. Hidaka, and H. Bosman, "Magnetic priming effects on noise, startup, and mode competition in magnetrons," *IEEE Transactions on Plasma Science*, vol. 33, no. 1, 1, pp. 94–102, Feb 2005.

[49] J. Luginsland, Y. Lau, V. Neculaes, R. Gilgenbach, M. Jones, M. Frese, and J. Watrous, "Three-dimensional particle-in-cell simulations of rapid start-up in strapped oven magnetrons due to variation in the insulating magnetic field," *Applied Physics Letters*, vol. 84, no. 26, pp. 5425–5427, Jun 28 2004.

[50] M. Fuks and E. Schamiloglu, "Rapid start of oscillations in a magnetron with a "transparent" cathode," *Physical Review Letters*, vol. 95, no. 20, pp. 205 101–1–205 101–4, Nov 11 2005.

[51] P. Pengvanich, V. Neculaes, Y. Lau, R. Gilgenbach, M. Jones, W. White, and R. Kowalczyk, "Modeling and experimental studies of magnetron injection locking," *Journal of Applied Physics*, vol. 98, no. 11, pp. 114 903–1–114 903–6, Dec 1 2005.

[52] P. Pengvanich, Y. Y. Lau, J. W. Luginsland, R. M. Gilgenbach, E. Cruz, and E. Schamiloglu, "Effects of frequency chirp on magnetron injection locking," *Physics of Plasmas*, vol. 15, no. 7, pp. 073 110–1–073 110–6, Jul 2008.

[53] P. Pengvanich, Y. Y. Lau, E. Cruz, R. M. Gilgenbach, B. Hoff, and J. W. Luginsland, "Analysis of peer-to-peer locking of magnetrons," *Physics of Plasmas*, vol. 15, no. 10, pp. 103 104–1–103 104–4, Oct 2008.

[54] E. J. Cruz, B. W. Hoff, P. Pengvanich, Y. Y. Lau, R. M. Gilgenbach, and J. W. Luginsland, "Experiments on peer-to-peer locking of magnetrons," *Applied Physics Letters*, vol. 95, no. 19, pp. 191 503–1–191 503–3, Nov 9 2009.

[55] J. W. Gewartowski and H. A. Watson, *Principles of Electron Tubes.* Pinceton: Van Nostrand, 1965.

[56] J. H. Booske, D. R. Whaley, W. L. Menninger, R. S. Hollister, and C. M. Armstrong, "Traveling-wave tubes," in *Modern Microwave and Millimeter Wave Power Electronics*, R. J. Barker, J. H. Booske, N. C. Luhmann Jr., and G. S. Nusinovich, Eds. Piscataway, NJ: IEEE Press, 2005, pp. 171 – 246.

[57] C. Kory and J. Dayton, "Effect of helical slow-wave circuit variations on twt cold-test characteristics," *IEEE Transactions on Electron Devices*, vol. 45, no. 4, pp. 972–976, Apr 1998.

[58] N. Luhmann Jr., G. Caryotakis, G.-S. Park, R. M. Phillips, and G. P. Scheitrum, "Affordable manufacturing," in *Modern Microwave and Millimeter Wave Power Electronics*, R. J. Barker, J. H. Booske, N. C. Luhmann Jr., and G. S. Nusinovich, Eds. Piscataway, NJ: IEEE Press, 2005, pp. 731 – 763.

[59] H. R. Johnson, "Backward-wave oscillators," *Proceedings of the Institute of Radio Engineers*, vol. 43, no. 6, pp. 684–697, 1955.

[60] D. Komm, R. Benton, H. Limburg, W. Menninger, and X. Zhai, "Advances in space TWT efficiencies," *IEEE Transactions on Electron Devices*, vol. 48, no. 1, pp. 174–176, Jan 2001.

[61] J. Booske, M. Converse, C. Kory, C. Chevalier, D. Gallagher, K. Kreischer, V. Heinen, and S. Bhattacharjee, "Accurate parametric modeling of folded waveguide circuits for millimeter-wave traveling wave tubes," *IEEE Transactions on Electron Devices*, vol. 52, no. 5, pp. 685–694, May 2005.

[62] J. Wilson, "Design of high-efficiency wide-bandwidth coupled-cavity traveling-wave tube phase velocity tapers with simulated annealing algorithms," *IEEE Transactions on Electron Devices*, vol. 48, no. 1, pp. 95–100, Jan 2001.

[63] C. L. Kory and J. D. Wilson, "Novel High-Gain, Improved-Bandwidth, Finned-Ladder V-Band Traveling-Wave Tube Slow-Wave Circuit-Design," *IEEE Transactions on Electron Devices*, vol. 42, no. 9, pp. 1686–1692, Sep 1995.

[64] D. Goebel, J. Keller, W. Menninger, and S. Blunk, "Gain stability of traveling wave tubes," *IEEE Transactions on Electron Devices*, vol. 46, no. 11, pp. 2235–2244, Nov 1999.

[65] M. Santra, L. Kumar, and J. Balakrishnan, "Analysis of Long-Periodic Permanent Magnet Structures for Electron Beam Focusing," *IEEE Transactions on Electron Devices*, vol. 60, no. 5, pp. 1776–1781, May 2013.

[66] Y. Y. Lau and D. Chernin, "A review of the ac space-charge effect in electron circuit interactions," *Physics Of Fluids B-Plasma Physics*, vol. 4, no. 11, pp. 3473–3497, Nov 1992.

[67] T. Antonsen, P. Safier, D. Chernin, and B. Levush, "Stability of traveling-wave amplifiers with reflections," *IEEE Transactions on Plasma Science*, vol. 30, no. 3, 1, pp. 1089–1107, Jun 2002.

[68] Z. Duan, Y. Gong, W. Wang, Y. Wei, and M. Huang, "Effect of attenuation on backward-wave oscillation start oscillation condition," *IEEE Transactions on Plasma Science*, vol. 32, no. 6, pp. 2184–2188, Dec 2004.

[69] E. Belyavskiy, I. Shevelenok, and S. Khotiaintsev, "Linear two-dimensional analysis of parasitic backward-wave oscillation in a monofilar-helix traveling wave tube," *IEEE Transactions on Electron Devices*, vol. 52, no. 4, pp. 603–610, Apr 2005.

[70] P. A. Sturrock, "Kinematics of Growing Waves," *Physical Review*, vol. 112, no. 5, pp. 1488–1503, 1958.

[71] R. J. Briggs, *Electron-Stream Interaction With Plasmas*. Cambridge: The M.I.T. Press, 1964.

[72] A. Bers, *Handbook of Plasma Physics*, M. N. Rosenbluth and R. Z. Sagdeev, Eds. New York: North-Holland, 1983.

[73] M. Chodorow and C. Susskind, *Fundamentals of Microwave Electronics*. New York: McGraw-Hill, 1964.

[74] Y. Y. Lau, private communication, 2012.

[75] Y. Y. Lau, K. Chu, L. Barnett, and V. Granatstein, "Gyrotron Traveling Wave Amplifier .1. Analysis of Oscillations," *International Journal of Infrared and Millimeter Waves*, vol. 2, no. 3, pp. 373–393, 1981.

[76] A. Pikovsky, M. Rosenblum, and J. Kurths, *Synchronization*. Cambridge: Cambridge University Press, 2001.

[77] J. C. Slater, *Microwave Electronics*. New York: Van Nostrand, 1950.

[78] W. Song, J. Sun, H. Shao, R.-z. Xiao, C.-h. Chen, and G.-z. Liu, "Inducing phase locking of multiple oscillators beyond the Adler's condition," *Journal of Applied Physics*, vol. 111, no. 2, pp. 023 302–1–023 302–5, Jan 15 2012.

[79] M. Cuneo, E. Waisman, S. Lebedev, J. Chittenden, W. Stygar, G. Chandler, R. Vesey, E. Yu, T. Nash, D. Bliss, G. Sarkisov, T. Wagoner, G. Bennett, D. Sinars, J. Porter, W. Simpson, L. Ruggles, D. Wenger, C. Garasi, B. Oliver, R. Aragon, W. Fowler, M. Hettrick, G. Idzorek, D. Johnson, K. Keller, S. Lazier, J. McGurn, T. Mehlhorn, T. Moore, D. Nielsen, J. Pyle, S. Speas, K. Struve, and J. Torres, "Characteristics and scaling of tungsten-wire-array z-pinch implosion dynamics at 20 MA," *Physical Review E*, vol. 71, no. 4, pp. 046 406–1–046 406–43, Apr 2005.

[80] J. D. Douglass and D. A. Hammer, "COBRA-STAR, a five frame point-projection x-ray imaging system for 1 MA scale wire-array Z pinches," *Review of Scientific Instruments*, vol. 79, no. 3, pp. 033 503–1–033 503–4, Mar 2008.

[81] S. C. Bott, D. M. Haas, Y. Eshaq, U. Ueda, F. N. Beg, D. A. Hammer, B. Kusse, J. Greenly, T. A. Shelkovenko, S. A. Pikuz, I. C. Blesener, R. D. McBride, J. D. Douglass, K. Bell, P. Knapp, J. P. Chittenden, S. V. Lebedev, S. N. Bland, G. N. Hall, F. A. S. Vidal, A. Marocchino, A. Harvey-Thomson, M. G. Haines, J. B. A. Palmer, A. Esaulov, and D. J. Ampleford, "Study of the effect of current rise time on the formation of the precursor column in cylindrical wire array Z pinches at 1 MA," *Physics of Plasmas*, vol. 16, no. 7, pp. 072 701–1–072 701–14, Jul 2009.

[82] D. A. Chalenski, B. R. Kusse, and J. B. Greenly, "Soldered contact and current risetime effects on negative polarity wire array Z pinches," *Physics of Plasmas*, vol. 16, no. 8, pp. 082 707–1–082 707–9, Aug 2009.

[83] C. L. Hoyt, P. F. Knapp, S. A. Pikuz, T. A. Shelkovenko, A. D. Cahill, P. A. Gourdain, J. B. Greenly, B. R. Kusse, and D. A. Hammer, "Cable Array Z-Pinch Experiments at 1 MA," *IEEE Transactions on Plasma Science*, vol. 40, no. 12, 2, SI, pp. 3367–3371, Dec 2012.

[84] M. R. Gomez, J. C. Zier, R. M. Gilgenbach, D. M. French, W. Tang, and Y. Y. Lau, "Effect of soft metal gasket contacts on contact resistance, energy deposition, and plasma expansion profile in a wire array Z pinch," *Review of Scientific Instruments*, vol. 79, no. 9, Sep 2008.

[85] J. Zier, M. R. Gomez, D. M. French, R. M. Gilgenbach, Y. Y. Lau, W. W. Tang, M. E. Ctlneo, T. A. Mehlhorn, M. D. Johnston, and M. G. Mazarakis, "Wire-tension effects on plasma dynamics in a two-wire Z-pinch," *IEEE Transactions on Plasma Science*, vol. 36, no. 4, 1, pp. 1284–1285, Aug 2008.

[86] M. Mazarakis, C. Deeney, M. Douglas, W. Stygar, D. Sinars, M. Cuneo, J. Chittenden, G. Chandler, T. Nash, K. Struve, and D. McDaniel, "Tungsten wire number dependence of the implosion dynamics at the Z-accelerator," *Plasma Devices and Operations*, vol. 13, no. 2, pp. 157–161, Jun 2005.

[87] D. Sinars, M. Cuneo, E. Yu, D. Bliss, T. Nash, J. Porter, C. Deeney, M. Mazarakis, G. Sarkisov, and D. Wenger, "Mass-profile and instability-growth measurements for 300-wire Z-pinch implosions driven by 14-18 MA," *Physical Review Letters*, vol. 93, no. 14, pp. 145 002–1–145 002–4, Oct 1 2004.

[88] T. Sanford, G. Allshouse, B. Marder, T. Nash, R. Mock, R. Spielman, J. Seamen, J. McGurn, D. Jobe, T. Gilliland, M. Vargas, K. Struve, W. Stygar, M. Douglas, M. Matzen, J. Hammer, J. DeGroot, J. Eddleman, D. Peterson, D. Mosher, K. Whitney, J. Thornhill, P. Pulsifer, J. Apruzese, and Y. Maron, "Improved symmetry greatly increases X-ray power from wire-array Z-pinches," *Physical Review Letters*, vol. 77, no. 25, pp. 5063–5066, Dec 16 1996.

[89] J. P. Apruzese, R. W. Clark, J. Davis, T. W. L. Sanford, T. J. Nash, R. C. Mock, and D. L. Peterson, "Comparative properties of the interior and blowoff plasmas in a Dynamic Hohlraum," *Physics of Plasmas*, vol. 14, no. 4, pp. 042 702–1–042 702–5, Apr 2007.

[90] R. A. Vesey, M. C. Herrmann, R. W. Lemke, M. P. Desjarlais, M. E. Cuneo, W. A. Stygar, G. R. Bennett, R. B. Campbell, P. J. Christenson, T. A. Mehlhorn, J. L. Porter, and S. A. Slutz, "Target design for high fusion yield with the double Z-pinch-driven hohlraum," *Physics of Plasmas*, vol. 14, no. 5, pp. 056 302–1–056 302–13, May 2007.

[91] S. Lebedev, F. Beg, S. Bland, J. Chittenden, A. Dangor, M. Haines, S. Pikuz, and T. Shelkovenko, "Effect of core-corona plasma structure on seeding of instabilities in wire array Z pinches," *Physical Review Letters*, vol. 85, no. 1, pp. 98–101, Jul 3 2000.

[92] J. P. Chittenden and C. A. Jennings, "Development of instabilities in wire-array Z pinches," *Physical Review Letters*, vol. 101, no. 5, pp. 055 005–1–055 005–4, Aug 1 2008.

[93] M. D. Greenburg, *Advanced Engineering Mathematics*. London: Pearson, 1998.